STUDY OF NANOCLUSTERS CONTAINING HIGH CONCENTRATIONS OF STABILIZED ATOMS BY OPTICAL AND ELECTRON SPIN RESONANCE METHODS

A Dissertation

by

ADIL MERAKI

Submitted to the Office of Graduate and Professional Studies of
Texas A&M University
in partial fulfillment of the requirements for the degree of

DOCTOR OF PHILOSOPHY

Chair of Committee,	David M. Lee
Co-Chair of Committee,	M. Suhail Zubairy
Committee Members,	Aleksei Zheltikov
	Andrew Comech
Head of Department,	Peter McIntyre

December 2016

Major Subject: Physics

ABSTRACT

Impurity-helium condensates (IHCs) are a new class of non-crystalline materials formed by injecting a gas mixture consisting of helium gas and an impurity gas into superfluid helium. We studied dynamics of thermoluminescence during destruction of porous structures formed by nanoclusters of nitrogen molecules containing high concentrations of stabilized nitrogen atoms. Porous structures were formed in bulk superfluid helium by injection of the products of discharges in nitrogen-helium gas mixtures through the liquid helium surface. Fast recombination of nitrogen atoms during warming-up led to explosive destruction of the porous structures accompanied by bright flashes.

We also investigated thermoluminescence of ensembles of molecular nitrogen nanoclusters, containing stabilized nitrogen atoms, immersed in liquid helium. We obtained experimental evidence for quantum vortex induced chemical reactions for nitrogen atoms in HeII leading to the appearance of luminescence. Thermoluminescence was also observed in HeI due to the process of nanocluster association resulting in thermal explosions of a small fraction of nanoclusters. Impurity-helium condensates created by injection of nitrogen atoms and molecules as well as rare gas (RG) atoms (Ne, Ar and Kr) into superfluid ^{4}He also have been studied via electron spin resonance (ESR) techniques and optical spectroscopy. Measurements of the ground-state spectroscopic parameters of nitrogen atoms show that the nanoclusters have a shell structure. N and O atoms reside in solid molecular layers of N_2. These layers form on the surfaces of RG (Ar or Kr) nanoclusters. We studied the dynamics of thermoluminescence spectra emitted during the warming of porous N-N_2-RG-He samples inside the superfluid helium. Using this experimental approach, it is possible

to study chemical reactions of heavy atoms and molecules at very low temperatures where normally diffusion and quantum tunneling in solid matrices not possible.

To my parents.

to my wife.

ACKNOWLEDGEMENTS

Professor Peter M. Rentzepis and his Postdoc Runze Li were essential in supplying equipment and providing assistance for performing determining the number of photons. Thank you Peter and Runze for sharing your experience and getting us off on the right track. Working on the determination of the number of photons with Runze Li, who I enjoyed collaborating with led to our becoming close friends. In addition, I'd like to thank my friend Yakup Boran detailed advise about writing new Matlab program for analyzing data was essential in the speeding of the project.

I am deeply grateful to my sponsor, the Republic of Turkey Ministry of National Education, for the funding me during these six years. I also gratefully acknowledge funding from NSF Grant No. DMR 1209255.

I would like to express the deepest gratitude to my parents, brothers, Yalcin and Enes, and my dear sister, Ilknur, for their love and support which I have always received.

And finally, I want to thank my beloved wife Cigdem Meraki for her love, encouragement and prayers during these years. It is a blessing that she is also a physicist, so she always understands me, correcting me and sacrificing her time mostly, staying alone while I spent long hours in the lab every day. Thanks for listening to my problems and providing perspective. She has been continually supportive of my graduate education. Thank you for the little things you have done like preparing lunch everyday and bringing dinner when I worked late nights. Last but not least, special thanks to my boys, Yusuf and Omer. Without you, my life would not have been so happy and colorful.

TABLE OF CONTENTS

LIST OF FIGURES

x

LIST OF TABLES

1.   INTRODUCTION

Although the technique of Impurity-Helium condensates (IHCs) has been known for more than forty years, the properties of IHCs are still the subject of continuous interest. IHCs are a new class of non-crystalline materials formed by injecting a gas mixture consisting of helium gas and an impurity gas into superfluid helium.[1] When the gas jet meets the surface of the superfluid helium, the formation of impurity nanoclusters each surrounded by one or two layers of solid helium due to Van der Waal forces occurs inside superfluid helium (see figure 1.1). These nanoclusters aggregate to form our samples. The characteristic sizes of impurity nanoclusters are of order 5 nm and the overall density of the impurity atoms and molecules is of order 10^{20} cm^{-3}.[2, 3, 4] Pores in the condensates have a broad distribution of sizes ranging from 8 to 860 nm.[3] All pores in the condensate are filled with liquid helium. This method has substantially improved the efficiency of atom stabilization and has led to achievement of relative concentrations of nitrogen atoms [N]/[N$_2$] in the range 10-30 percent.[5, 6]

A variety of atomic and molecular impurities can be injected into bulk superfluid helium such as N$_2$, O$_2$, H$_2$, D$_2$, and noble gases.[7, 8, 9] There are different techniques such as electron spin resonance (ESR), [10, 11], optical spectroscopy, [12, 13, 14], x-ray diffraction [3, 4, 15, 16], and ultrasound [3, 17, 18], that can be employed for characterization of samples and investigation of the quantum phenomena during the sample warming up processes. Although there exists a variety of techniques, ESR and optical spectroscopy have been mostly used for investigation of IHCs prepared with different impurities. Optical spectroscopy methods were extensively used in the past for studies of atoms and molecules in solid nitrogen. Thermoluminescence of
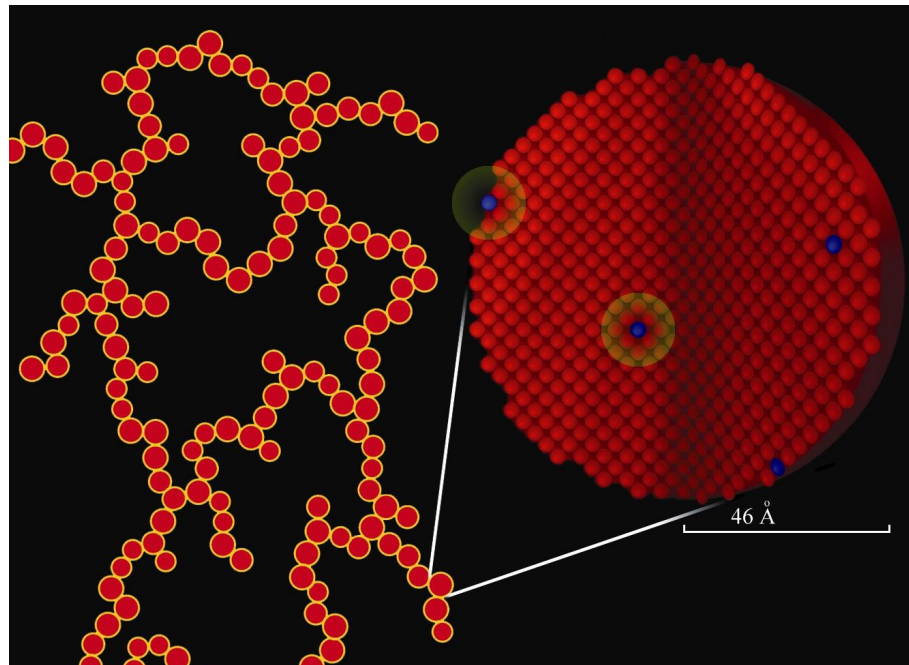
Figure 1.1: An idealized view of a nitrogen-helium condensate. Red shows nitrogen-molecules arranged in an FCC lattice. Yellow shows a monolayer of ^4He solidifed on the helium surface. The surrounding supefluid ^4He is not shown. Blue shows nitrogen atoms substituted within the molecular lattice.

nitrogen samples containing stabilized nitrogen atoms was explained by processes of the diffusion and recombination of nitrogen atoms. After removing liquid helium from the sample cell, increasing the temperature of the samples initiates the recombination of stabilized nitrogen atoms that accompanied by intense emission. The luminescence of the α-group of atomic nitrogen N($^2D \rightarrow ^4$S), the β-group emission of atomic oxygen O(^{1}S$\rightarrow^1$D) and Vegard-Kaplan molecular bands N$_2$(A$^3\Sigma_u^+$, $0 \rightarrow$ X$^1\Sigma_g^+$, ν'') can be detected as well as spectra of various molecules such as NO, NH, O$_2$ during the processes of sample destruction. The ESR method has also been extensively used to study the properties of IHCs. The ESR technique provides the spectroscopic characteristics of various free radicals such as N, and H atoms embedded in different matrix environments. Linewidth, g-factor and hyperfine splitting can be obtained from the shape and the position of the ESR spectra.

The main objective of this study is to investigate the chemical and physical properties of IHCs, and reveal the influence of the quantum properties of superfluid helium on the behavior of porous nanoclusters containing stabilized nitrogen atoms. In this work, we discuss optical spectroscopic studies of ensembles of nanoclusters formed in bulk superfluid helium. Investigations of solid nitrogen containing stabilized nitrogen atoms have a long history. [19, 20] Electrons and γ-rays were intensively used for excitation of atoms and molecules in solid nitrogen. [21, 22, 23] Luminescence of atoms and molecules from samples formed by condensation of the products of a discharge in nitrogen gas on the surfaces cooled by liquid helium was studied by Broida et al.[24] This study had the goal of obtaining high concentrations of stabilized atoms at low temperatures for possible practical applications. The idea that slowing down of the rate of any chemical reaction by lowering temperature can provide large concentration of stabilized atoms at low temperatures. However, the measurements of

magnetic susceptibilities of these samples showed only very low concentrations (0.1 %) of stabilized nitrogen atoms.[25] For the samples obtained by this method, the first peak of thermoluminescence upon warming was observed at a temperature near 9 K.[25] Most of optical the spectra were observed by integration of light emitted by the sample over a broad spectral range. The emission spectra of NO and O_2 trapped in N_2 matrices and rare gas matrices excited by e-beam bombardment have been studied by Peyron and Broida. [26, 27] They first identified the presence of the M-bands ($a^4\Pi \rightarrow X^2\Pi$ transitions) of NO molecules in solid nitrogen. This group also first observed the second Herzberg bands ($c^1\Sigma_u \rightarrow X^3\Sigma_g$ transitions) of O_2 molecules in solid nitrogen and in solid rare gas matrices, with the exception of neon. However, there was no information on the dynamics of luminescence from these species. Difficulties in obtaining the dynamics of luminescence for a broad spectral range from solid nitrogen containing stabilized atoms were attributed to very low concentrations of stabilized atoms and as a result, a low intensity of sample luminescence.

Later a method for condensing the products of electrical discharges in mixtures of nitrogen and helium gases into bulk superfluid helium was developed.[1, 28] By using this method, impurity-helium condensates (IHC) were formed in bulk superfluid helium.[29] These condensates consist of collections of nanoclusters, which form a porous structure similar to aerogel inside superfluid helium. ESR results shows that the N atoms mostly reside on the surfaces of molecular nitrogen nanoclusters.[30, 31] The addition of rare gases to nitrogen-helium condensates has substantially improved the efficiency of atom stabilization. High concentrations of nitrogen atoms stabilized in molecular nitrogen nanoclusters provided enough chemical energy for developing chain recombination reactions during warming of the samples. The fast release of stored energy resulted in intense sample thermoluminescence. In the past, studies

of the dynamics of thermoluminescence during destructions of impurity-helium condensates of N and N_2 were performed for the samples which also contained atoms of rare gases as well as small amount of oxygen.[14, 32, 33, 34] Strong emissions from α-, α'- and δ- groups of N atoms, β- and β'- groups of O atoms, Vegard-Kaplan (VK) bands of N_2, and M- bands of NO molecules were observed. Additionally, emissions corresponding to different transitions from XeO molecules were registered during destructions of nitrogen-xenon-helium samples.[34] Intense luminescence of oxygen atoms and oxygen containing molecules were explained by the shorter lifetimes of these species. During destructions of nitrogen-helium samples, only emissions from the β- and β'- groups of O atoms and the α-, α'- groups of N atoms were observed in similar experiments.[14, 32] In this work we studied the dynamics of thermoluminescence spectra emitted during the destruction of porous nitrogen-helium samples. We also investigated the influence of oxygen impurities on the spectra. It was found that a relatively small change of the oxygen impurity content drastically influenced the spectra obtained. The bands of oxygen atoms as well as NO and O_2 molecules became more intense at the end of the nitrogen-helium sample destruction. We observed the emissions corresponding to $c^1\Sigma_u \rightarrow X^3\Sigma_g$ and $c^1\Sigma_u \rightarrow a^1\Delta_g$ transitions of O_2 molecules in solid nitrogen.[35, 36] At the end of the destruction, we observed increasing of the relative intensity of the emission of NO molecules. This effect is a result of the process of accumulation of NO molecules in the sample during warming up process. Upon further warming of the sample, $(NO)_2$ dimers can be formed in the sample. The reaction of the $(NO)_2$ dimers with N atoms at the final stage of destruction led to the formation of two oxygen atoms in close vicinity. The recombination of these pairs of O atoms results in formation of excited O_2 molecules.

Additionally, analysis of the dynamics of sample luminescence allowed us to evaluate possible positions of the emitting species in the molecular nitrogen nanoclusters.

Apart from study of the influence of impurities during the sample destruction, we also proposed a new experimental technique for investigation quantum turbulence in superfluid helium. Quantum turbulence (QT) has been studied in HeII for more than half a century.[37, 38] Since QT research started to involve atomic Bose Einstein condensates, QT has recently become one of the hot-topics in low-temperature physics. In the past, many theoretical and experimental studies were performed for the visualization of quantized vortices.[39, 40, 41, 42] Considerable progress in this area of research has been achieved due to applications of new experimental methods.[43, 44, 45, 46, 47] Visualization of vortex cores has led to the observation of the reconnection of vortices and direct observation of Kelvin waves excited by quantized vortex reconnections.[48, 42] Dissipation of quantum turbulence was studied at the zero temperature limit.[49, 50] The technique of nano-wire formation by ablating metallic nanoparticles from a target in HeII was realized on the basis of coalescence of the nanoparticles on the vortices.[51, 52] All of these investigations were performed in bulk superfluid helium. Investigations of quantum turbulence in restricted geometries is challenging. The only example of this type of study is the investigation of quantum vortices inside free superfluid droplets with sizes ranging from 100 to 1000 μm.[53, 54]

In the past, many theoretical and experimental studies of the behavior of liquid helium in porous restricted geometries were performed [55, 56]. Liquid helium has long provided a testing ground for theories of phase transitions. Finite size effects might shift or smear out phase transitions. The multiply-connected substrate geom-

etry may change the effective dimensionality, or the disorder induced by the porous material may change the nature of the transition[57, 58].

In our work we have found a unique means for investigating the influence of the quantum properties of liquid helium on the stability and behavior of porous nitrogen-helium condensates containing stabilized nitrogen atoms. During heating of the IHCs sample immersed in superfluid helium, the green emission due to the α-group of nitrogen atoms and blue emission were detected and explained as a result of N(^2D) atom emission originated from N(^2D)-N$_2$ complexes.[13] The bright blue emission was assigned to the Vegard-Kaplan bands correspond to transitions N$_2$(A$^3\Sigma_u^+$, 0 $\rightarrow$ X$^1\Sigma_g^+$, ν'').[13] Recently, the thermoluminescence spectra of IHCs immersed in superfluid helium was observed and is explained possible mechanism as a neutralization reactions occurring in impurity nanoclusters.[59] We observed thermoluminescence of nitrogen atoms and molecules in molecular nanoclusters immersed in liquid helium while increasing the temperature from 1.3 to 4.4 K. Two thermoluminescence maxima were observed, one in superfluid helium at T$\sim$1.9 K and another in normal helium at T$\sim$3.2 K. Thermoluminescence in HeII was found to be a result of chemical reactions of nitrogen atoms residing on surfaces of nanoclusters initiated by quantum vortices. Developing our new experimental method has provided further understanding of the behavior of quantum turbulence in this field of research in confined geometries. We observed the thermoluminescence of ensembles of molecular nitrogen nanoclusters containing stabilized nitrogen atoms in superfluid helium due to the quantum turbulence. QT has been found to induce chemical reactions in porous ensembles of nanoclsuters. Using this new experimental approach, it is also possible to study chemical reactions of heavy atoms and molecules at very

low temperatures where normally their diffusion and tunneling in solid matrices not possible.

The structure of this dissertation reflects the fact that different samples were studied in our investigations of impurity-helium condensates. Section 2 is dedicated to investigations of thermoluminescence dynamics of the samples formed by nitrogen nanoclusters. And in section 2, We give description of the experimental apparatus and sample preparation method which we used in all the experiments. Section 3 describes our results for quantum vortices and thermally induced luminescence of nitrogen nanoclusters immersed in liquid helium. Although the sample preparation methods in this section is almost the same as the one described section 2, we also employed another experimental setup which enables simultaneous electron spin resonance (ESR) and optical studies of nanoclusters with stabilized free radicals. And in section 4, We investigated the addition of rare atoms (Ne, Ar, and Kr) to the condensed N_2-He gas mixture on the efficiency of stabilization of N atoms in IHCs. We also investigated the characteristics of the dynamic of the thermoluminescence spectra for different stabilized number of N atoms in the samples.

2. THERMOLUMINESCENCE DYNAMICS DURING DESTRUCTIONS OF POROUS STRUCTURES FORMED BY NITROGEN NANOCLUSTERS IN BULK SUPERFLUID HELIUM[*]

We studied dynamics of thermoluminescence during destruction of porous structures formed by nanoclusters of nitrogen molecules containing high concentrations of stabilized nitrogen atoms. Porous structures were formed in bulk superfluid helium by injection of the products of discharges in nitrogen-helium gas mixtures through the liquid helium surface. After evaporation of liquid helium from the sample cell, fast recombination of nitrogen atoms during warming-up led to explosive destruction of the porous structures accompanied by bright flashes. Intense emissions from the α-group of nitrogen atoms, the β-group of oxygen atoms and the Vegard-Kaplan bands of N_2 molecules were observed at the beginning of destruction. At the end of destruction the M- and β-bands of NO molecules as well as bands of O_2 molecules were also observed. Observation of the emissions from NO molecules at the end of destruction was explained by processes of accumulation of NO molecules in the system due to the large van der Waals interaction of NO molecules. For the first time, we observed the emission of the O_2 molecules at the end of destruction of the porous nitrogen structures as a result of the $(NO)_2$ dimers formation in solid nitrogen and subsequent processes leading to the appearance of excited O_2 molecules.

2.1 Theoretical background

In this work we studied spectra of the thermoluminescence of a nitrogen-helium condensates during their destruction. The destruction of IHC samples are stimulated by warming from 1.4 K to 14 K to initiate diffusion and the recombination of stabilized free radicals, thus leading to formation of excited atoms and molecules. In this section we will introduce the theoretical background of α-group of nitrogen atoms, the β-group of oxygen atoms and the Vegard-Kaplan bands of N_2 molecules as well as bands of O_2 and NO molecules.

2.1.1 Atomic systems

(a)Atomic nitrogen

The nitrogen has three electrons outside closed shells, and the electronic configuration is $1s^2 2s^2 2p^3$. The ground state of the nitrogen atom has all three spins aligned in the $^4S_{3/2}$. In the diagram(see figure 2.1), the $^2D_{5/2}$ and $^2D_{3/2}$ states lie as 2.38 eV above the $^2S_{3/2}$ ground state of N atom.[60] The α-group emission provides the characteristic green glow is due to the $N(^2D - ^4S)$ transition. In the gas phase the wavelengths of these forbidden transitions are $N(^2D_{5/2} - ^4S_{3/2})$: 520.0 nm, and $N(^2D_{3/2} - ^4S_{3/2})$: 519.8 nm and the lifetimes, τ, are 1.6×10^5s and 4.4×10^5s, respectively. Spin and parity selection rules for electric-dipole transitions strongly forbid the $N(^2D_{5/2} - ^4S_{3/2})$ transitions but they are dramatically enhanced in the solid phase due to interaction with the crystalline field and lattice phonons. In solid nitrogen this emission consists of eight main lines, the strongest lying at 522 nm (zero-phonon line) and a 523-525 nm (phonon induced wing). Furthermore, the lifetime of $^2D - ^4S$ emission in solid nitrogen is long 40 s.[61] In addition, in the solid N_2 or solid heavy
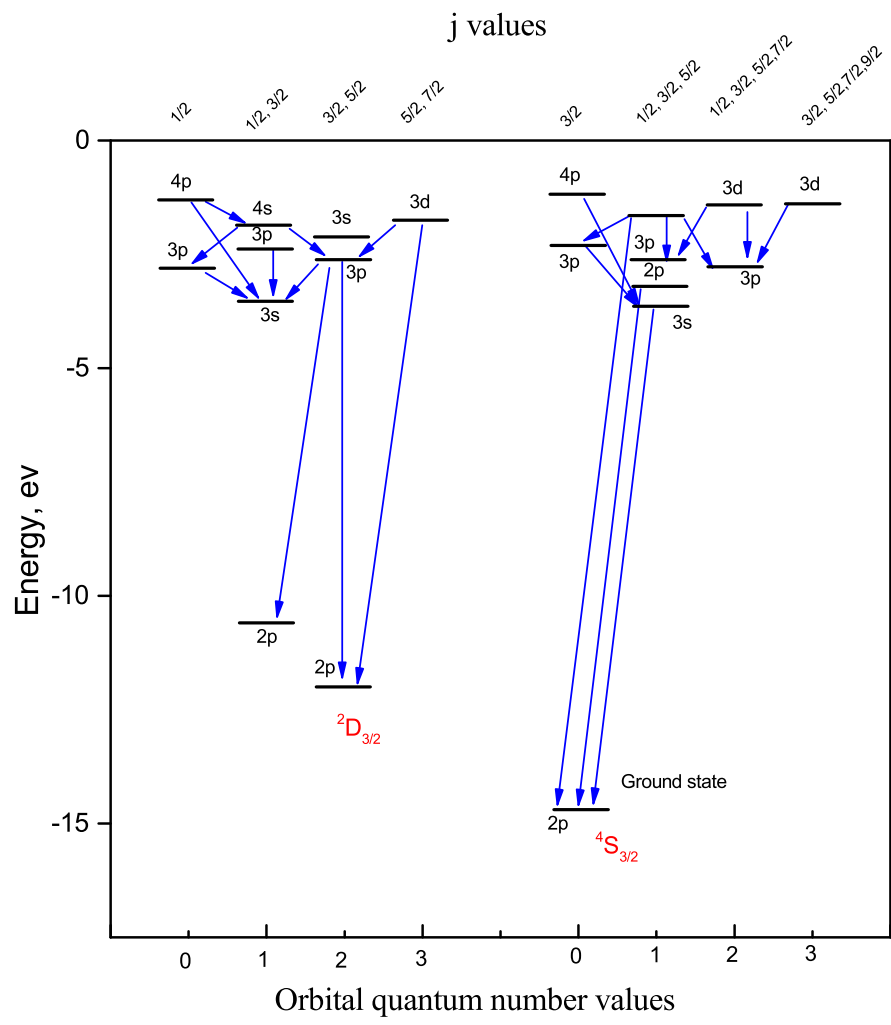
Figure 2.1: Nitrogen energy levels.

rare gas matrices the α- group transition is shifted, as a rule, to the red. In Kr-, Ar-, and Ne- containing IHCs the centers of α-group spectra were red-shifted by ~ 4, ~ 2.4, and ~ 1 nm, respectively, as compared to the $N(^2D -^4 S)$ transition in the gas phase.[13] The α-group was accompanied always by a less intense second group ~ 594 nm (this is called α'). In addition to the α', the α'' and α''' systems , which arise from a simultaneous transition of an N atom $(^2D -^4 S)$ with a $\Delta\nu = \pm 1$ transition of a neighboring N_2 molecule in ground state, were studied by Oehler et al. (1977) [62]. These transitions (α'' and α''') were not observed in our work. Dressler et al. have shown that the transitions responsible for α, α', α'' and α''' as

$$N(^2D) \rightarrow N(^4S) + \alpha\text{-}group, \tag{2.1}$$

$$N(^2D) + N_2(X^1\Sigma_g^+, \nu'' = 0) \rightarrow N(^4S) + N_2(X^1\Sigma_g^+, \nu'' = 1) + \alpha'\text{-}group; \tag{2.2}$$

$$N(^2D) + N_2(X^1\Sigma_g^+, \nu'' = \nu) \rightarrow N(^4S) + N_2(X^1\Sigma_g^+, \nu'' = \nu - 1) + \alpha''\text{-}group; \tag{2.3}$$

$$N(^2D) + N_2(X^1\Sigma_g^+, \nu'' = \nu) \rightarrow N(^4S) + N_2(X^1\Sigma_g^+, \nu'' = \nu + 1) + \alpha'''\text{-}group; \tag{2.4}$$

where (2.1), (2.2), (2.3), and (2.4) the excited $N(^2D)$ atoms can arise in the matrix due to energy transfer from excited $N_2(A^3\Sigma_u^+)$ molecules to $N(^4S)$ atoms,

$$N_2(A^3\Sigma_u^+) + N(^4S) \rightarrow N(^2D) + N_2(X^1\Sigma_g^+). \tag{2.5}$$

(b)Atomic oxygen

The oxygen has a total of eight electrons. Considering the Pauli exclusion principle and the electron orbitals, the electron configuration of atomic oxygen is $1s^2 2s^2 2p^4$. The 2p orbitals are partially filled, so there are three different ways to fill the electrons in the $2p_x$, $2p_y$ and $2p_z$ states. According to Hund's rules, the ground state of atomic oxygen is a ^3P, triplet P, state which has two unpaired electrons. The

configuration ^1D, singlet D, is the first excited state of atomic oxygen. The second excited state of atomic oxygen, is designated as the ^1S state.

The transition $^1S -^1 D$ of O atoms is also extremely forbidden in the gas phase but dramatically enhanced in the solid phase. A group of three broad lines centered around the 557 nm β-group with associated vibrational sidebands at $\sim$ 630 nm (this is called β') and at $\sim$ 496 nm (this is called β''), has been observed in a N_2 matrix. [63] The transfer of energy from an excited $N_2(A^3\Sigma_u^+)$ molecule to an oxygen atom is also allowed;

$$N_2(A^3\Sigma_u^+) + O(^3P) \rightarrow O(^1S) + N_2(X^1\Sigma_g^+) \tag{2.6}$$
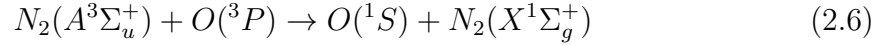
The emissions from this state produced β-group ($^1S \rightarrow^1D$) O atoms

$$O(^1S) \rightarrow O(^1D) + \beta\text{-}group. \tag{2.7}$$

And β', β'' and β''' are as follows:

$$O(^1S) + N_2(X^1\Sigma_g^+, \nu'' = 0) \rightarrow O(^1D) + N_2(X^1\Sigma_g^+, \nu'' = 1) + \beta'\text{-}group; \tag{2.8}$$

$$O(^1S) + N_2(X^1\Sigma_g^+, \nu'' = \nu) \rightarrow O(^1D) + N_2(X^1\Sigma_g^+, \nu'' = \nu - 1) + \beta''\text{-}group; \tag{2.9}$$

$$O(^1S) + N_2(X^1\Sigma_g^+, \nu'' = \nu) \rightarrow O(^1D) + N_2(X^1\Sigma_g^+, \nu'' = \nu + 1) + \beta'''\text{-}group; \tag{2.10}$$
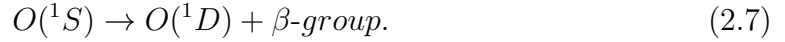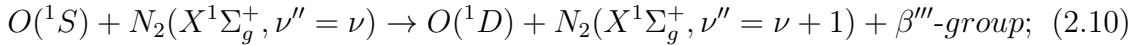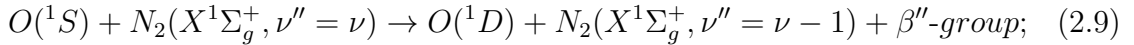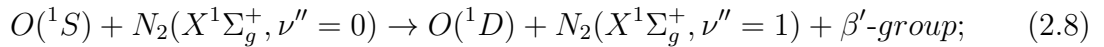
Energy levels for these emission features are shown in fig. 2.2.
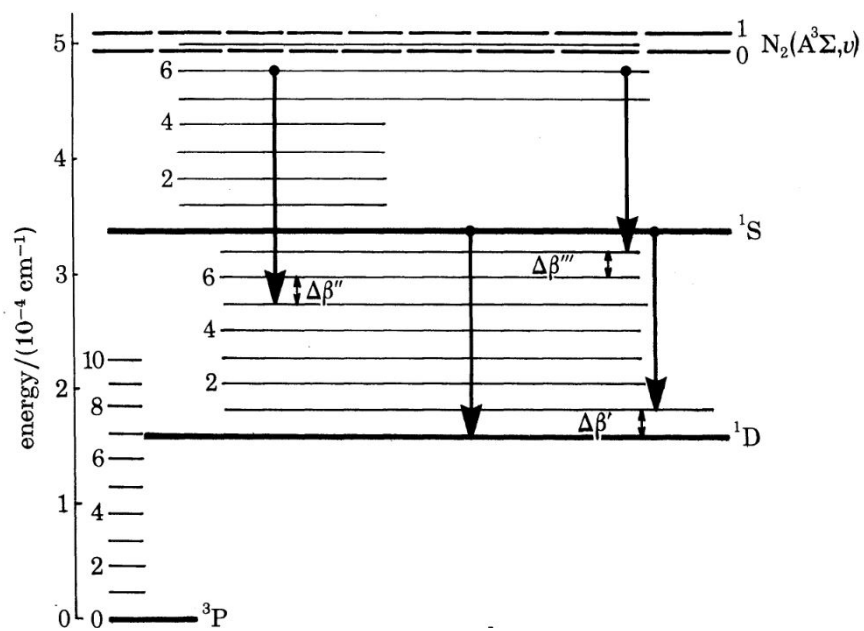
Figure 2.2: Energy-level diagram and schematic diagram of electronic O atom doped solid N_2. Reprinted with permission from [63].

2.1.2 Molecular systems

(a) O$_2$

There are six bound electronic states of O$_2$ molecule populated from the recombination of ground-state O(^3P) atoms. Figure 2.3 shows potential energy curves of O$_2$, and three metastable states designated as the Herzberg states $A^3\Sigma_\nu^+$, $c^1\Sigma_u^-$ and $C^3\Delta_u$. The a-X transition is the Herzberg I system, the c-X transition is Herzberg II system, and C-X transition is Herzberg III system. Three metastable states are just below the dissociation limit, which is ~ 41256.6 cm^{-1} ($D_0(X)$) in the gas phase. In the gas phase, O$_2$ can be efficiently dissociated through the Schumann-Runge absorption. In solids, however, the dissociation is extremely inefficient due to the so-called cage effect.[64] Emissions from the three upper O$_2$ states are much weaker. In the early work of Broida, the $c^1\Sigma_u^- \rightarrow X^3\Sigma_g^-$ Herzberg II system was observed in N$_2$ and rare gas matrices, but unfortunately they were misidentified. Later, Goodman and Brus [36] also detected this system, and also misidentified them as C-X(Herzberg III system). In the present work, during destruction of nitrogen nanoclusters containing stabilzed N and O atoms for the first time we observed an intensive band which correspond to the $c^1\Sigma_u^- \rightarrow X^3\Sigma_g^-$ and $c^1\Sigma_u^- \rightarrow a^1\Delta_g$ transitions of O$_2$ molecules in solid nitorgen. Koda and Kajihara [65] have observed the c-a emission of O in solid N$_2$ by a KrF excimer laser. The apperance of the excited $O_2(c^1\Sigma_u^-)$ molecules is a result of recombination of oxygen atoms in solid nitrogen.

$$O(^3P) + O(^3P) \rightarrow O_2(c^1\Sigma_u^-); \tag{2.11}$$
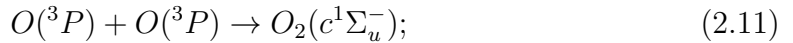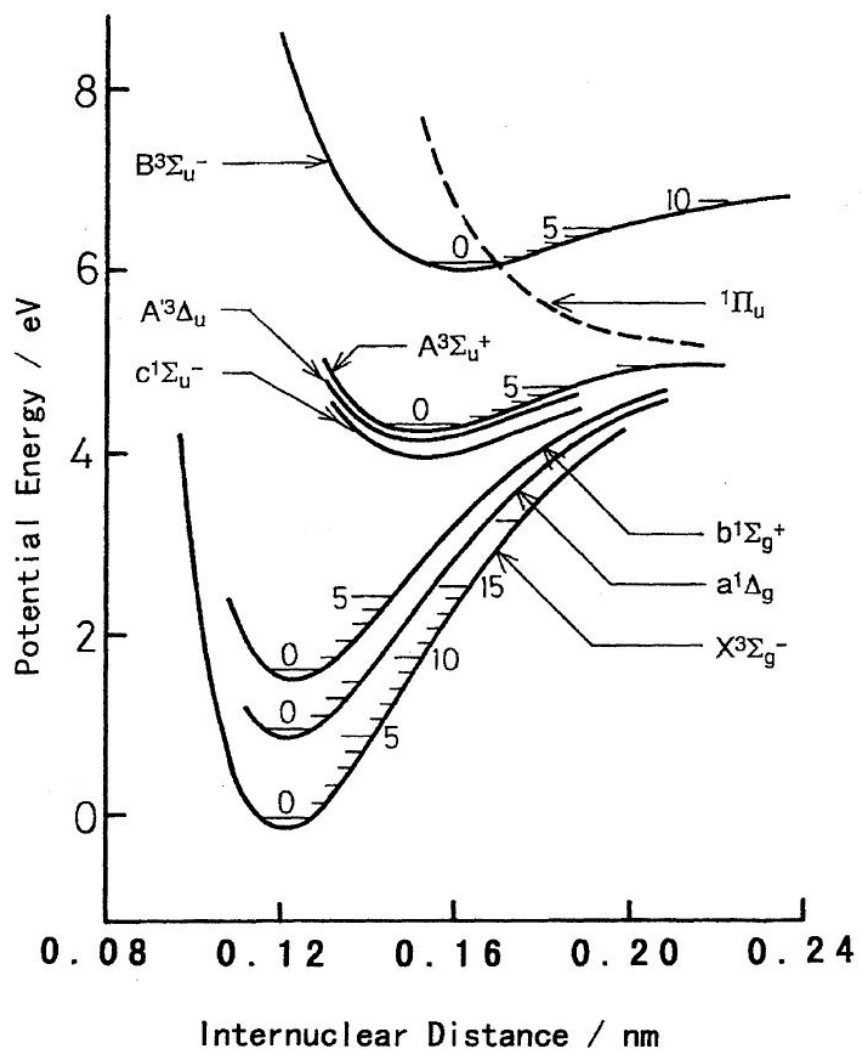
Figure 2.3: Potential energy curves of O_2. Reprinted with permission from [66].

(b) Vegard-Kaplan system

The Vegard-Kaplan (V-K) band system $A^3\Sigma_u^+ \rightarrow X^1\Sigma_g^+$ of nitrogen corresponds to an electric-dipole transition, occuring only by violating the approximate spin-selection rule $\Delta S = 0$. It is not ordinarily observed in either the discharge or afterglow regions, and has been detected only under rather special conditions. This system of the nitrogen molecules was observed in nitrogen solids at 4.2 K, the bands occurring very weakly at the higher oxygen concentration. The presence of oxygen leads nitrogen combining with oxygen to form nitric oxide, which seems to be quite effective in quenching the V-K bands.

(c) NO

Open-shell structure of the NO radical molecule is of great importance in atmospheric chemistry. The electronic configuration of the $X^2\Pi$ ground state of the NO radical is $1\sigma^2 1\sigma^{*2} 2\sigma^2 2\sigma^{*2} 3\sigma^2 1\pi^4 1\pi^*$. The electron transfer $\pi^4\pi^* \rightarrow \pi^3\pi^{*2}$ results in the valence states $a^4\Pi, B^2\Pi, L^2\Pi$, and $4^2\Pi$ in the experimental nomenclature. The ground X state is split into $^2\Pi_{1/2}$ and $^2\Pi_{3/2}$ components separated by 121.1 cm^{-1} and the $N(^4S) + O(^3P), N(^4S) + O(^1D)$ and $N(^2D) + O(^3P)$ atomic limits give birth to a complex set of valence excited states in the 5-9 eV range. The transition of M-band ($a^4\Pi \rightarrow X^2\Pi$) is spin-forbidden in the gas phase and it was not studied as much as the strongest spectroscopic transitions of the γ band ($A^2\Sigma \rightarrow X^2\Pi$) and β-band ($B^2\Pi \rightarrow X^2\Pi$).[67, 68]

2.2   Experimental setup and technique

2.2.1   Description of apparatus and procedure

The technique of preparation of IHCs was first developed in 1974 by E.B Gordon, L.P. Mezhov-Deglin and O.F. Pugachev as an attempt to stabilize the highest possible concentrations of free radicals.[1] The schematic diagram of our experimental setup is shown in Fig. 2.4. For sample preparation we employed a low-temperature cryostat and an external gas handling system. The low-temperature part of the set up consisted of two double-walled glass dewars for liquid helium (LHe) and liquid nitrogen (LN_2), an atomic source, a thermomechanical fountain pump, and an experimental cell. The inner surfaces of both dewars were partially covered with silver films to minimize the thermal radiation. For optical study and visual observations of sample preparation, 2 cm wide vertical strips remained uncovered by the silver films. The radiation baffles in the throat of helium dewar are used to block thermal radiation from top room temperature metal flange. The gas handling system consists of a cylinder manifold, a vacuum system for preparation of gas mixtures and cleaning of gaseous components, and lastly, a mass flow controller. For the preparation of nitrogen-helium gas mixtures, Linde research grade helium (99.9999% purity) was used. Oxygen contamination in these mixtures was determined to be 1ppm in the helium gas. The mixed gases were stored in a container at room temperature. The prepared gas mixtures entered the helium dewar through a quartz capillary, where they passed through a zone of RF discharge (frequency $\sim$ 50MHz, power $\sim$ 75 W) that dissociated the impurity molecules. The discharge was powered by an E&I 3100L RF amplifier which was used to amplify the RF signal generated by a Hewlett-Packard Signal generator, Model 8656B. The RF power was applied to the
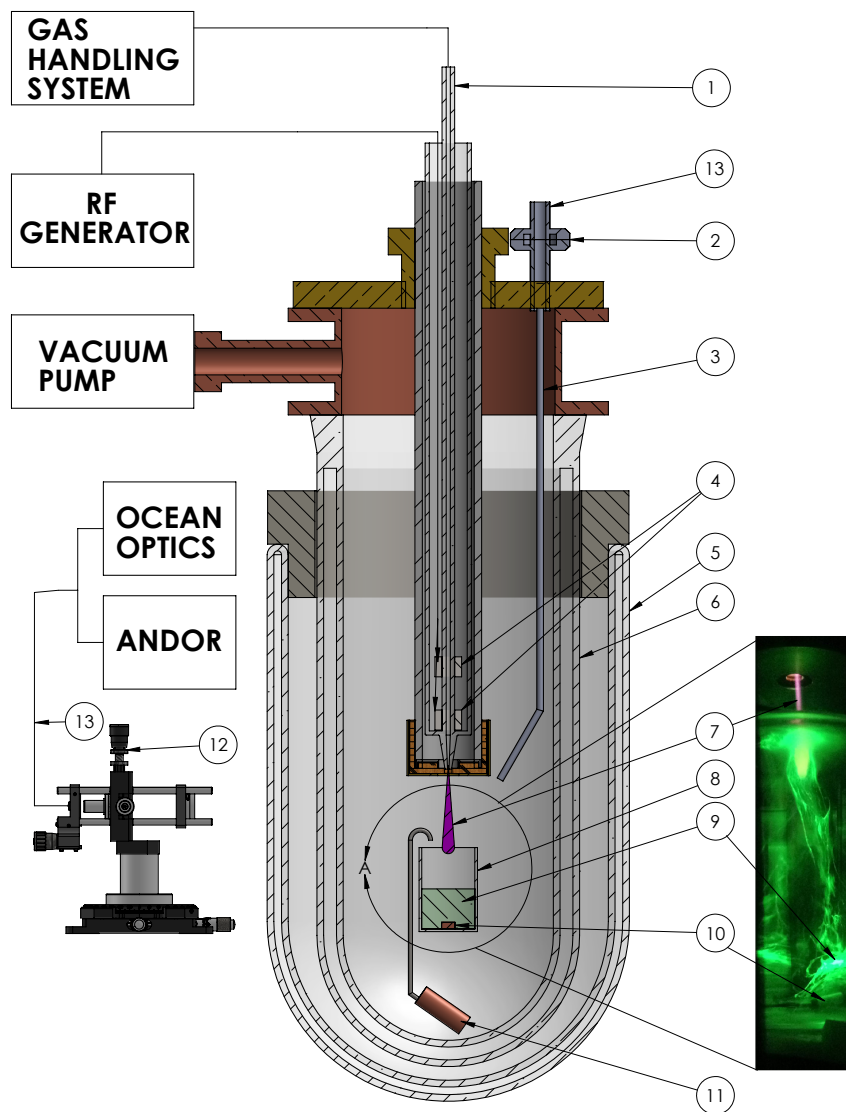
Figure 2.4: Scheme of the experimental setup for optical study of nitrogen-helium condensates: 1-quartz capillary, 2-feedthrough for optical fiber, 3-optical fiber, 4-electrodes for electrical discharge, 5- nitrogen dewar, 6- helium dewar, 7- gas jet, 8-quartz beaker for sample accumulation, 9- nitrogen-helium sample, 10- thermometer, 11- fountain pump, 12- motorized lab jack, 13- bifurcated optical fiber. Insert shows a photo of the nitrogen-helium sample accumulation process.

flowing gas by electrodes placed in the lower part of the capillary. The gas flow was accurately measured and controlled by a Brooks Model 5850E Mass Flow Controller which typically provided a constant flux of 5×10^{19} particles/sec. The discharge region of quartz source was constantly cooled with liquid nitrogen, which surrounded the quartz capillary. Thermal insulation of the quartz source was provided by a stainless steel double walled jacket. [29] After passing through the discharge, the gas mixtures were injected into the helium dewar through an orifice with diameter 0.75 mm. In the region under the orifice a well-formed gas jet was created (see insert in Fig.2.4). This jet was directed to a glass beaker (inner diameter of 2.2 cm, height 4 cm) filled with superfluid helium. The top of the beaker was placed 20 mm under the orifice. A constant level of superfluid helium in the glass beaker was maintained by means of a fountain pump placed at the bottom of the main liquid helium bath. Sample accumulation lasted 20-40 min. The volume of the sample accumulated in the glass beaker inside bulk He II was 10-12 cm^3. During the sample formation, the temperature of the main bath was maintained at 1.45 K with the aid of an Edwards model E2M80 Two Stage mechanical pump which provided helium gas pressures down to $\sim$ 250 Pa.

2.2.2   Systems for registration of optical spectra

We investigated the emission spectra during the process of condensation of gas mixtures and also luminescence spectra of the nitrogen-helium solid samples during their destruction. Recent developments in fiber optics technology have allowed us to improve the efficiency of the collection of light from the sample emissions. In a previous approach with our setup, the emitted light passed through slits in the silvering of the glass dewars. The light was then collected outside of the dewars

by a lens at the entrance of an optical fiber. Once the sample preparation was complete, the optical system was adjusted into position for the collection of light from the bottom of the beaker with the aid of a motorized lab jack to observe sample destruction. Later our cryogenic setup was equipped with an optical fiber assembly, part of which was installed inside the helium dewar (pos.3 in Fig. 2.4), where it was able to withstand liquid helium temperatures. The fiber was manufactured by Gulf Photonics using a special cryogenic adhesive. The open ferrules on the end of the optical fiber were directed into the bottom of the beaker. The low temperature fiber assembly is connected to the bifurcated fiber via a vacuum feedthrough. The vacuum feedthrough and the bifurcated fiber are mated using splice bushings. In our previous approach, the glass dewars restricted the accessible spectral range to 325-1100 nm. Having this new optical fiber assembly allowed us to detect emission spectra in the broader range of 200-1100 nm (UV-VIS-IR range).

Preparation for the sample destruction process involved turning off the fountain pump, leading to a decrease of the liquid helium level in the beaker and, as a result, the sample was compressed and collected near the bottom of the beaker. After cutting-off the HeII flow into the beaker, we waited 20 min to allow all the liquid helium to evaporate from the beaker. Leaving the formed solid sample in the dark for a while allows all trapped reactants to relax to the ground state, in particular radicals and excited species captured from the gas phase jet after having passed through the discharge zone. Then, to start the process of warming the samples, we stopped pumping the helium vapor from the cryostat. As a result, the temperature inside the beaker rose from 1.4 K to 14 K during a period of 40-150 sec. The temperature of the sample was recorded with a Lake Shore semiconducting thermometer calibrated in the region from 1.1K to 40K. This thermometer was placed at the bottom of the

21

glass beaker. The pressure of helium vapor in the dewar was registered by an MKS-626B manometer covering the range from 0.1 to 100 Torr. The rising temperature in the beaker initiated the destruction of the collected sample which was accompanied by spontaneous flashes. After the emitted light passed through the low temperature fiber assembly and vacuum feedthrough, the light was transferred to two different spectrometers with the bifurcated fiber assembly. By using the bifurcated fiber assembly, we could make simultaneous measurements in two different spectral ranges. The bifurcated fiber has two outlets, one for our Ocean Optics HR2000+ spectrometer and the other for an Andor Shamrock SR-500i spectrograph. The Ocean Optics spectrometer has a spectral resolution of 1.3 nm (FWHM) in the range 200-1100 nm. The Andor spectrometer consists of the Shamrock SR-500i, with a 0.52 nm (1st grating) resolution, equipped with a cooled EM-CCD (Newton 970) camera. The emission spectra are registered by the Andor spectrometer with a 150 lines/mm grating (blaze wavelength 500 nm), and a wavelength range of 340 nm (λ nm =325-665 nm) with a Newton CCD detector unit cooled to -60 C (for higher sensitivity). Temporal resolution was achieved with a camera, the output of which was amplified 200 times by electron multiplying CCD. The image detected by the camera has a size of 1600x200 pixels. Signals obtained are decoded by the Andor & Solis software supplied by the Andor Company. The improved spectral resolution allowed us to observe the detailed structure of our spectra with high precision. During the sample destruction, the registration times of spectra were 100 ms or 250 ms for the Ocean Optics spectrometer, and only 3 ms for the Andor registration. This high detection sensitivity system allowed us to study the dynamics of the spectra.

2.3 Experimental results

2.3.1 Thermoluminescence spectra of samples prepared by different nitrogen-helium gas mixtures

Increasing the temperature of the nitrogen-helium sample initiates the recombination of stabilized nitrogen atoms that is accompanied by luminescence of the sample which lasted 150 s (final 27.5 s of destruction is shown in Fig. 2.5). The warm-up thermogram and pressure diagram during sample destruction are presented in the insert of Fig. 2.5. Sublimation of helium atoms adsorbed on impurity cluster surfaces was a trigger, initiating the recombination of the stabilized radicals, which was accompanied both by intense emission and a rapidly increasing temperature.[14] It was previously proved that chemical reactions of N atoms in solid N_2 can proceed at temperatures above 8 K.[69]   Figure 2.5 shows the dynamics of thermoluminescence during the final stage of destruction of the sample condensed from the gas mixture $[^{14}N_2]$:[He]=1:100. Each spectrum in Fig. 2.5 was taken with an exposure time of 250 ms. At the beginning of observation, only the luminescence of the α-group of atomic nitrogen N($^2D \rightarrow ^4$S) and Vegard-Kaplan molecular bands N_2(A$^3\Sigma_u^+$, 0 $\rightarrow$ X$^1\Sigma_g^+$, ν'') can be seen, and their intensities grow with increasing temperature. It should also be noted that the intensity of the β-group emission of atomic oxygen O(^{1}S$\rightarrow^1$D) is relatively small at the beginning, but it increases very steeply with the simultaneous appearance of the M-bands (transitions a$^4\Pi \rightarrow$ X$^2\Pi$) of NO molecules. This correlation between the β-group of O atoms and M-bands of NO molecules continues during the entire destruction process. The M- bands are very broad with unresolved structure. In addition to the β- groups of O atoms, and the sequence of M-bands of NO molecules, the β-bands of NO molecules, corresponding to the
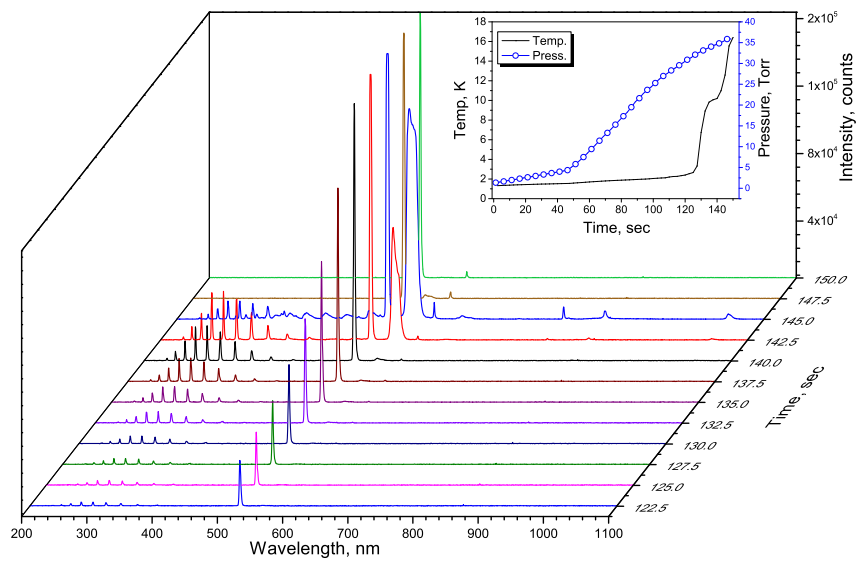
Figure 2.5: Dynamics of the luminescence spectra of nitrogen-helium sample during destruction. The sample was prepared from the gas mixture $[^{14}N_2]/[He]=1/100$. Spectra were obtained by the Ocean Optics spectrometer. Each spectrum shown in the Figure is a sum of 10 spectra detected with exposure time 250 ms. Temperature and pressure dependences on time during sample destruction are shown in the insert.

B$^2\Pi$-X$^2\Pi$ transitions, and the Herzberg II system of O$_2$ molecules, corresponding to the (c$^1\Sigma_u^- \rightarrow$X$^3\Sigma_g^-$) transitions, appeared at the end of the sample destruction (see Fig. 2.6a and 2.6b). The spectrum of the most intense flash is shown in Fig. 2.6b, where one can see the δ -group (transition ^{2}P- ^{2}D) and δ''-group of atomic nitrogen as well as β'- and β''- groups of O atoms in addition to the above-mentioned bands. The positions and origins of all molecular bands in the observed spectra are listed in Tables 2.1 and 2.2. The presence of α'-, β'-, β''-, δ'- groups of N and O atoms in the spectra indicates that N$_2$ molecules are neighbors of these atoms.[14, 62]

One can also see the γ- line at 793 nm, which has now been identified as the bound-bound transition $^1D - ^3P$ of nitrogen anions N$^-$.[70] The thermoluminescence maximum was detected during sample destruction at a temperature of 12 K. From comparison of the spectra shown in Fig. 2.6a and 2.6b, we can conclude that very significant changes in the spectra occur during the final stage of sample destruction. The most striking change was the enhancement of the luminescence from O atoms as well as NO and O$_2$ molecules. To study these effects in more detail, we performed investigations of the dynamics of the luminescence spectra from a sample prepared from the gas mixture N$_2$:He=1:400. In this sample the ratio of oxygen to nitrogen content should be 4 times larger in comparison with the sample prepared from the gas mixture N$_2$:He=1:100 as a result of somewhat larger amounts of oxygen contaminated helium gas. Spectra were obtained by the Andor spectrometer, which provided a better sensitivity and time resolution (3 ms). Figure 2.7a shows the dynamics of the luminescence spectrum during the last 12 seconds of sample destruction. Spectra were studied in the spectral range 325-665 nm where we expected to observe the bands of NO and O$_2$ molecules. Each spectrum presented in Fig. 2.7a represents a sum of 500 spectra taken by the Andor spectrometer with exposure time 3 ms.
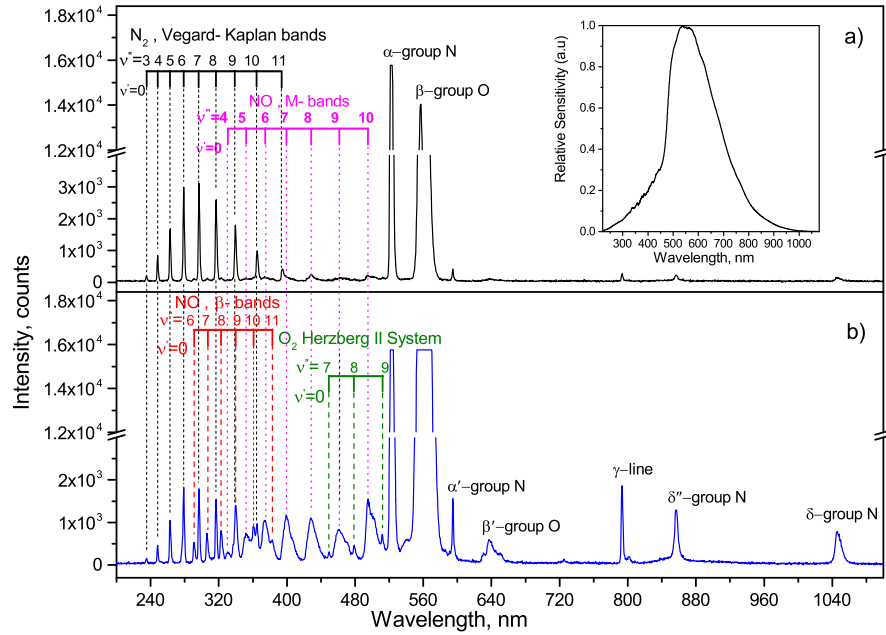
Figure 2.6: Two spectra taken by Ocean Optics spectrometer at the end of destruction of the sample which was prepared from the gas mixture $[^{14}N_2]/[He]$=1/100 a) spectrum taken 400 ms before the end of the destruction, sensitivity dependence of Ocean Optics spectrometer is shown in the insert. b) spectrum for the most intense final flash at the end of destruction. Exposure time for each spectrum is 250 ms.

Table 2.1: Positions of the NO M-bands ($a^4\Pi \rightarrow X^2\Pi$) and NO β-bands ($B^2\Pi - X^2\Pi$) emitted during destruction of the samples prepared from gas mixtures $[^{14}N_2]$:[He] =1:100 and $[^{15}N_2]$:[He] =1:100.

Band	$^{14}N^{16}O$	$^{14}N^{16}O$	$^{15}N^{16}O$	$^{14}N^{16}O$	$^{14}N^{16}O$	$^{15}N^{16}O$
(ν',ν'')	M-bands	M-bands[71]	M-bands	β-bands	β-bands[71]	β-bands
(0,4)	330.70	331.80	-	-	263.40	-
(0,5)	353.56	352.10	-	-	276.90	275.37
(0,6)	373.97	374.60	370.74	290.84	290.50	289.12
(0,7)	398.64	399.40	396.32	306.36	306.00	304.27
(0,8)	428.84	428.70	422.92	322.52	322.40	320.79
(0,9)	461.17	462	455.90	339.74	340.40	337.28
(0,10)	494.36	-	496.22	360.79	359.30	378.58
(0,11)	-	-	-	383.75	381.20	-

Table 2.2: Positions of the N$_2$ Vegard-Kaplan bands ($A^3\Sigma_u^+, 0 \rightarrow X^1\Sigma_g^+, \nu''$) emitted during destruction of the samples prepared from gas mixtures $[^{14}N_2]$: [He] =1:100 and $[^{15}N_2]$: [He] =1:100.

Band (ν',ν'')	$^{14}N_2$	$^{14}N_2$[72]	$^{15}N_2$	$^{15}N_2$[72]
(0,3)	235.40	235.08	233.67	233.74
(0,4)	248.33	248.17	246.20	246.24
(0,5)	263.00	262.60	260.11	259.97
(0,6)	278.94	278.59	275.28	275.11
(0,7)	297.01	296.40	291.96	291.89
(0,8)	316.99	316.34	310.70	310.59
(0,9)	339.74	338.83	331.59	331.55
(0,10)	365.04	364.37	355.71	355.20

As one can see from Fig.2.7a, the appearance of the NO bands starts ~ 6 seconds before the end of sample destruction. One of the spectra observed in the last 6 second is shown in Fig. 2.7b with identification of emitted bands. Figure 2.7c shows the dynamics of luminescence at the final 30 ms of sample destruction. Only one spectrum was registered during this last brief period. The details of this spectrum with identification of all of the bands are shown in Fig. 2.7d. Surprisingly, only the β-group of O atoms and the second Herzberg bands of molecular oxygen were found in this spectrum. Table 2.3 shows the positions of the O_2 bands emitted at the end of the destruction of the samples prepared from gas mixture $[^{14}N_2]$:$[He]$=1:400.

As one can see from Figs. 2.5,2.6, and 2.7 we observed rather intense bands of NO and O_2 molecules during the most intense luminescence flashes at the end of sample destruction. The NO $(a^4\Pi, 0 \rightarrow X^2\Pi, \nu'')$ bands were broad. These bands correspond to the envelope of overlapping bands from NO molecules in different environments. NO molecules have a wide distribution of positions and orientations in the N_2 matrix which is responsible for the broadening of the bands [71].

2.3.2 Influence of oxygen on thermoluminescence spectra of nitrogen-helium samples

As was mentioned earlier, we did not add intentionally any oxygen to the gas mixtures. The presence of oxygen in the samples is a result of small contaminations of oxygen in the helium and nitrogen gases used for preparation of the samples. To study the influence of the oxygen impurities on spectra of nitrogen-helium samples during destruction we performed investigations of three different samples which were formed from $^{15}N_2$:He gas mixtures with different nitrogen contents - 0.1%, 0.25% and 1%. The integrated spectra of luminescence of these samples during destruction are
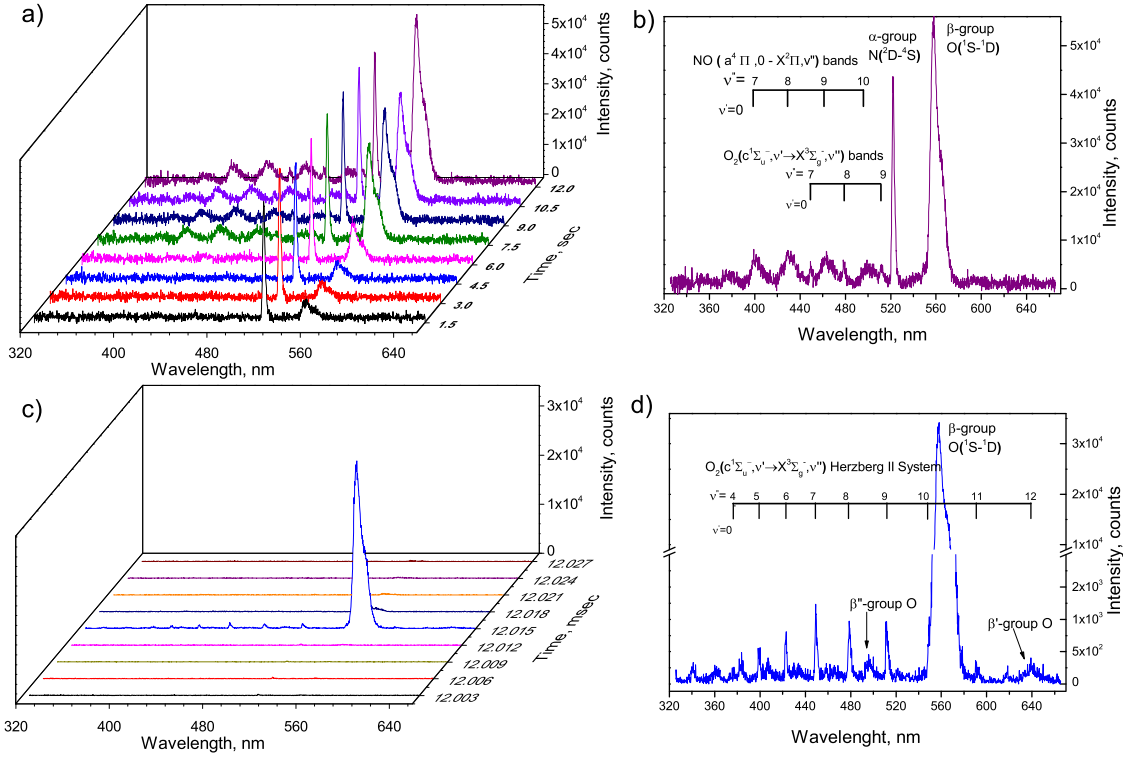
Figure 2.7: Dynamics of the luminescence spectra of nitrogen-helium sample at the end of destruction: a) dynamics of spectra which were accumulated during period 1.5 s, b) the spectrum which corresponds to 12th second in Fig. 2.7 is shown with identification of the observed bands, c) dynamics of spectra during last 30 ms of sample destruction, d) final spectrum registered during sample destruction with identification of the observed bands. Sample was prepared from gas mixture $[^{14}N_2]/[He]=1/400$. Spectra were obtained by the Andor spectrometer with exposure time 3 ms.

Table 2.3: Positions of the O_2 second Herzberg bands $(c^1\Sigma_u^-, 0 \to X^3\Sigma_g^-, \nu'')$ emitted at the end of the destruction of the sample prepared from gas mixture $[^{14}N_2]$:[He] =1:400.

Band (ν', ν'')	Band position λ (nm)	Solid N_2 λ (nm)[73]	Gas phase λ (nm)
(0,4)	377.12	377.1	376.21
(0,5)	398.43	398.7	398.03
(0,6)	423.28	422.5	422.4
(0,7)	449.02	449.0	449.1
(0,8)	478.77	478.4	479.15
(0,9)	511.07	511.3	512.88
(0,10)	-	548.7	551.00
(0,11)	591.0	590.8	594.52
(0,12)	638.97	639.3	644.51

shown in Fig.2.8. For the spectra obtained in the case of the sample prepared from the gas mixture $^{15}N_2$:He =1:100, only intense α- and β- groups are observed. In the cases of two other samples the spectra are less intense, but in addition to α- and β-groups, the bands of NO and O_2 molecules are also present. Moreover, for the gas mixture with smaller nitrogen content, the intensity of NO and O_2 bands increased relative to the intensity of α- and β- groups.

The most intense spectrum observed at the end of destruction of the sample prepared from a gas mixture $[^{15}N_2]$:[He] =1:100 is shown in Fig. 2.9. For this sample we have observed one more O_2 band system as compared with the spectrum obtained during destruction of the sample prepared from gas mixture $[^{14}N_2]$:[He] =1:100. This system corresponds to the $c^1\Sigma_u^- \to a^1\Delta_g$ transitions of O_2 molecules. Table 2.4 presents the positions of the observed bands with references to the O_2 $(c^1\Sigma_u^- \to a^1\Delta_g)$ system observed in solid N_2. Three bands of the Herzberg II system $(c^1\Sigma_u^- \to X^3\Sigma_g^-)$ were also detected.

The difference between the thermoluminescence spectra of the samples containing various nitrogen isotopes might be explained by different oxygen contents of the gas mixtures used. Although most of oxygen contamination is provided by the helium gas, the nitrogen gases also contain oxygen impurities. For the preparation of the gas mixture for the lighter nitrogen isotope - $[^{14}N_2]$: [He] =1:100, a Matheson nitrogen research grade gas was employed with an oxygen content smaller than 0.5 ppm, whereas for preparation of the gas mixture from the heavier nitrogen isotope - $[^{15}N_2]$:[He] =1:100, a Cambridge Isotope Laboratories nitrogen gas was employed with an oxygen content 24 ppm. As a result, the oxygen content is higher in the mixture containing $^{15}N_2$ as compared with the previous mixture. This explanation is supported by the fact that the integrated intensity ratio of the β- and α- groups
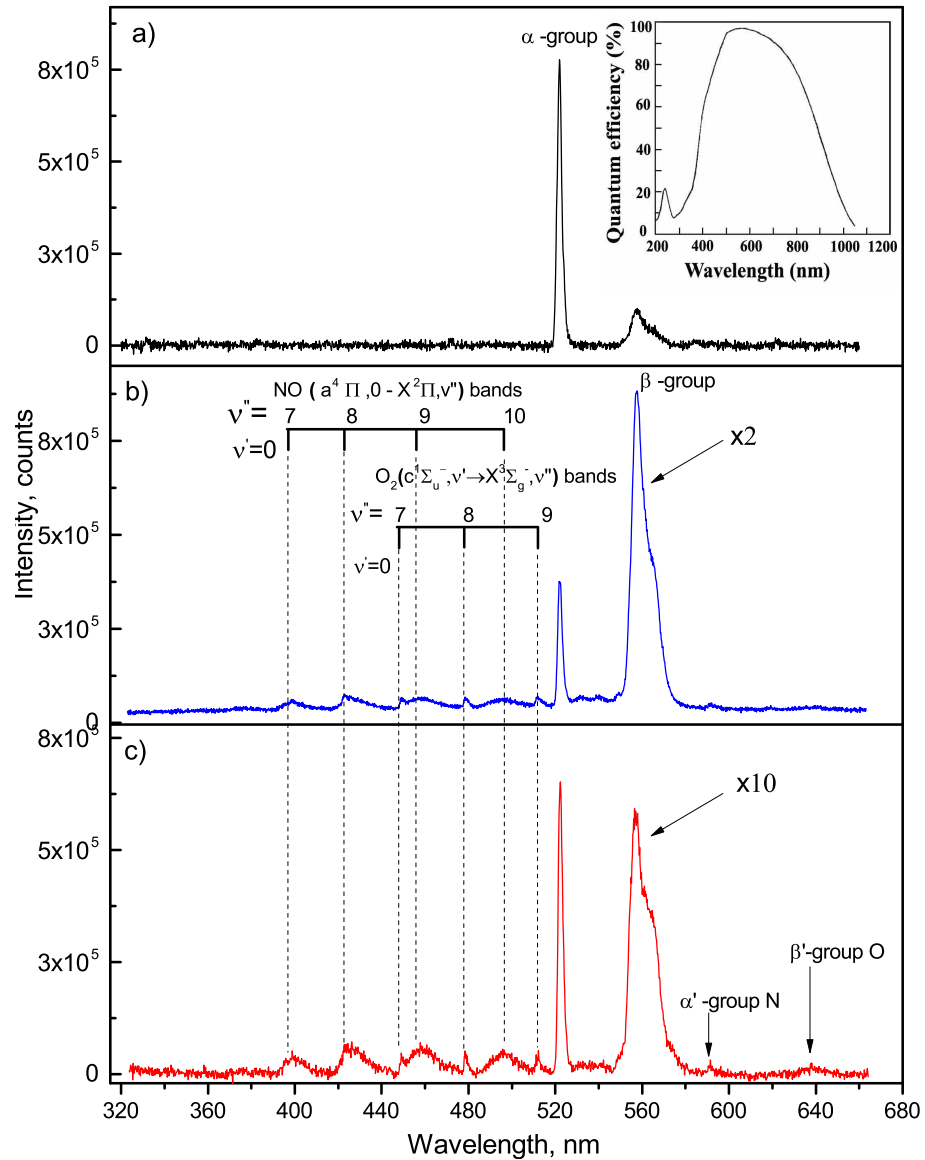
Figure 2.8: Integrated luminescence spectra obtained during destructions of three nitrogen-helium samples. Samples were prepared from different $^{15}N_2$:He gas mixtures: a) 1:100, b) 1:400, c) 1:1000. Quantum efficiency for the Newton CCD detector is shown in the insert.
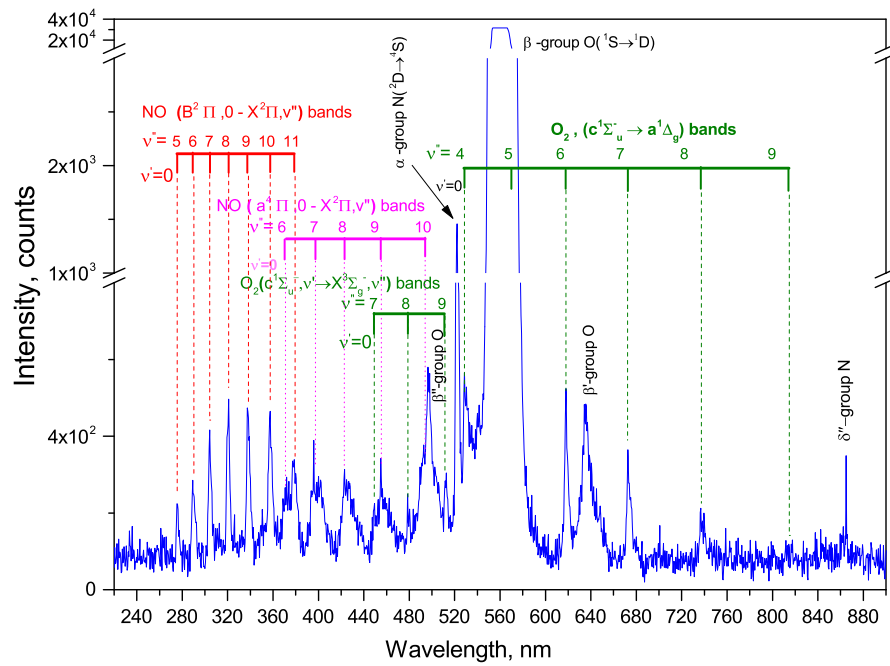
Figure 2.9: The spectrum of the most intense flash at the end of the destruction of the sample which was prepared from the gas mixture $[^{15}N_2]/[He]=1/100$. Spectrum was obtained by Ocean Optics spectrometer with an exposure time 400 ms.

Table 2.4: Band positions of the transitions $(c^1\Sigma_u^-, 0 \to a^1\Delta_g, \nu'')$ of O_2 molecules emitted during the destruction of the samples prepared from a gas mixture $[^{15}N_2]$:$[He]$ =1:100.

Band (ν', ν'')	Band position λ (nm)	Solid N_2 λ (nm)[35]	Gas phase λ (nm)[73]
(0,4)	529.28	529.52	526.39
(0,5)	-	570.84	567.56
(0,6)	618.21	618.42	614.74
(0,7)	673.12	673.67	669.25
(0,8)	738.18	737.73	732.92
(0,9)	814.32	814.00	808.14

(I_β/I_α) for the spectrum obtained during destruction of the sample prepared from the [$^{14}N_2$]: [He] =1:100 gas mixture (I_β/I_α=0.3) was smaller than that obtained during destruction of the sample prepared from the heavier nitrogen isotope - [$^{15}N_2$]:[He] =1:100 gas mixture (I_β/I_α=0.4).

2.4   Discussion

Impurity-helium condensates (IHCs) are porous nanomaterials formed by nanoclusters of impurities injected into superfluid helium. Nanoclusters create a semi-rigid network inside the superfluid helium. The characteristic size of impurity nanoclusters is of order 5 nm and the density of impurities inside superfluid helium is of order 10^{20} cm^{-3} as determined from x-ray experiments.[2, 3, 29] Atomic species formed in gas phase discharges were captured mostly on the surfaces of impurity nanoclusters.[30, 31] The average concentrations of nitrogen atoms in nitrogen-helium condensates were found to be as high as $10^{19}cm^{-3}$.[6] The values of local concentrations of N atoms in the samples were substantially larger, ($8.10^{20}cm^{-3}$).[6] As a result, the nitrogen-helium samples are characterized by very high specific energy contents (up to $\sim 10^4$ J/g).[10] One or two layers of solid helium covered the surfaces of impurity nanoclusters preventing connections between N atoms residing on surface layers of the nanoclusters. These samples were rather stable while immersed in bulk superfluid helium. Removing liquid helium from the sample led to collapsing of the pores in the samples and compressing of the sample. During this process the association of nanoclusters occurs as a result of developing connections between nanoclusters, which is accompanied by sublimation of the layers of solid helium and recombination of nitrogen atoms residing on the surfaces of nanoclusters. As a result, the temperature of the samples was increased and they emitted light. First

we analyze the dynamics of the luminescence spectra during sample destruction obtained in the experiments. At the beginning of destruction we observed that the glowing of the samples increased in intensity with time. As in the earlier studies of nitrogen-neon-helium and nitrogen-krypton-helium samples,[14, 32, 33] in this stage of the nitrogen-helium sample destruction, emissions from the α-group of N atoms, the Vegard-Kaplan (V-K) bands of N_2 molecules, and also the β-groups of O atoms were observed. The mechanism of sample luminescence at this stage of destruction is well known.[21, 33, 62] Diffusion and recombination of nitrogen atoms in the ground ^4S state produce metastable $N_2(A^3\Sigma_u^+)$ molecules:

$$N(^4S) + N(^4S) \rightarrow N_2(A^3\Sigma_u^+) \tag{2.12}$$
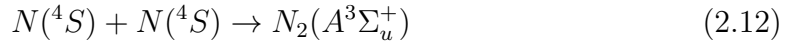
The excitations from these molecules were efficiently transferred along the N_2 matrix to the stabilized $N(^4S)$ and $O(^3P)$ atoms, resulting in excitation of ^2D- state of N atoms and ^1S- state of O atoms

$$N_2(A^3\Sigma_u^+) + N(^4S) \rightarrow N(^2D) + N_2(X^1\Sigma_g^+), \tag{2.13}$$

$$N_2(A^3\Sigma_u^+) + O(^3P) \rightarrow O(^1S) + N_2(X^1\Sigma_g^+) \tag{2.14}$$
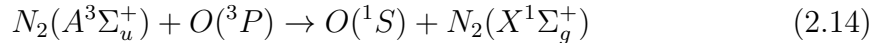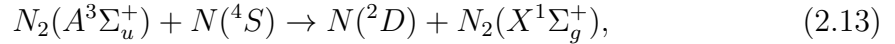
The emissions from those excited states produced the α-group ($^2D \rightarrow ^4S$) of N atoms and β-group ($^1S \rightarrow ^1D$) of O atoms

$$N(^2D) \rightarrow N(^4S) + \alpha\text{-}group, \tag{2.15}$$

$$O(^1S) \rightarrow O(^3P) + \beta\text{-}group. \tag{2.16}$$
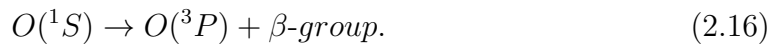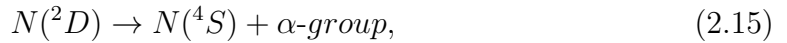
The intensity of the β-group emission of O atoms is considerably larger than the intensity of α-group emission of N atoms because of the much higher ($\sim 10^5$ times) probability of the O($^1S \rightarrow ^1$D) transition as compared with that of the N($^2D \rightarrow ^4$S) transition in a nitrogen matrix.[14, 74] Although the concentration of stabilized N atoms in the clusters is two or three orders of magnitude larger than that of the O atoms, the significantly larger probability of the transition of O atoms leads to a stronger emission from the O atoms. Some of the metastable $N_2(A^3\Sigma_u^+)$ molecules emitted light, providing Vegard-Kaplan bands. Recombination of N atoms did occur mostly near the surfaces of N_2 nanoclusters and the energy released in chemical reactions was transferred inside nanoclusters. The energy was captured by N and O atoms stored in the layers closest to the surface.

At the next stage, when the temperature was raised further and the diffusion of atoms became faster, the conditions for chain reactions involving N atoms to take place were satisfied and we observed explosion-like destruction of the samples, which was accompanied by bright light flashes. At this stage the recombination of N atoms was more frequent and the rate of energy release became much larger, allowing excitation of atoms and molecules stored in all layers of the nanoclusters. The emission from the species with short lifetimes became more intense. In the spectra the broad M-band of NO molecules and intense β-group of O atoms were observed at this stage (see Fig.2.7a). The intensities of emission of the V-K bands of N_2 molecules were substantially decreased. At the final stage, in addition to the above mentioned bands, the β-bands of NO molecules, the second Herzberg bands of O_2 molecules, the β'- and β''-group of O atoms as well as α'-, δ- and δ''- groups of N atoms were observed (see Fig. 2.6b). The weak luminescence of the α'-, δ- , δ''-

and the β'- and β''- corresponded to the following processes:

$$N(^2D) + N_2(X^1\Sigma_g^+, \nu'' = 0) \rightarrow N(^4S) + N_2(X^1\Sigma_g^+, \nu'' = 1) + \alpha'\text{-}group; \quad (2.17)$$

$$N_2(A^3\Sigma_u^+) + N(^4S) \rightarrow N(^2P) + N_2(X^1\Sigma_g^+); \quad (2.18)$$

$$N(^2P) \rightarrow N(^2D) + \delta\text{-}group; \quad (2.19)$$

$$N(^2P) + N_2(X^1\Sigma_g^+, \nu'' = 1) \rightarrow N(^2D) + N_2(X^1\Sigma_g^+, \nu'' = 0) + \delta''\text{-}group; \quad (2.20)$$

$$O(^1S) + N_2(X^1\Sigma_g^+, \nu'' = 0) \rightarrow O(^3P) + N_2(X^1\Sigma_g^+, \nu'' = 1) + \beta'\text{-}group; \quad (2.21)$$

$$O(^1S) + N_2(X^1\Sigma_g^+, \nu'' = 1) \rightarrow O(^3P) + N_2(X^1\Sigma_g^+, \nu'' = 0) + \beta''\text{-}group. \quad (2.22)$$

As can be seen from Fig. 2.7b, at the end of the destruction of the nitrogen-helium samples the most intense bands in the luminescence spectra corresponded to the species containing oxygen, such as is O, NO and O_2. This fact provides evidence for the existence of a mechanism for accumulating oxygen-containing species in the nanoclusters during the whole process of sample destruction. We will discuss this mechanism later.

We will emphasize that only investigations of the dynamics of the sample luminescence permitted observation of bands of NO and O_2 molecules in the spectra at the very end of the destruction process. In earlier studies of luminescence during the destruction of nitrogen-helium samples prepared from the gas mixture N_2:He=1:100, the integrated spectra did not show any bands of NO and O_2 molecules.[32] Similar results were obtained in this work. Those bands were absent in the integrated spectra for the sample prepared from gas mixture N_2:He=1:100 as shown in Fig. 2.8a. In this sample the ratio between oxygen and nitrogen molecules (O_2/N_2) (taking into consideration the contamination of oxygen in the helium gas of 1 ppm) should be of

order 10^{-4}. We investigated the influence of increasing the relative oxygen content in the nitrogen-helium gas mixtures on the luminescence spectra of the nitrogen-helium samples during destruction. As can be seen from Fig. 2.8b, increasing the ratio O_2/N_2 to 4×10^{-4} in the gas mixture N_2:He=1:400 used for sample preparation led to the appearance of the M bands of NO and the second Herzberg bands of O_2 molecules in integrated luminescence spectra obtained during sample destruction. Further increasing the ratio O_2/N_2 to 10^{-3} in the gas mixture N_2:He=1:1000 provided evidence that most of the luminescence at the very end of sample destruction occurs from oxygen atoms and oxygen-containing molecules (NO, O_2) (see Fig. 2.8c). It should be mentioned that the overall intensity of luminescence for the last sample was one order magnitude smaller than that for sample prepared from gas mixture N_2:He=1:100.

The precise registrations of the luminescence spectra during the destruction of the samples provide information about the emitting species. Table 2.1 list the positions of the M- and β- bands of $^{14}N^{16}O$ and $^{15}N^{16}O$ molecules. Table 2.2 shows the positions of V-K bands of $^{14}N_2$ and $^{15}N_2$ molecules. Tables 2.3 and 2.4 show the band positions of the second Herzberg system and the bands corresponding to the transitions ($c^1\Sigma_u^- \rightarrow a^1\Delta_g$) of O_2 molecules. Comparisons between the experimentally observed N_2, NO and O_2 band positions with the results of previous work [35, 36, 71, 72, 73] actually lead us to conclude that the species emitting light in our experiments were indeed in a N_2 matrix. Emission spectra of NO/N_2 system have been reported earlier using direct depostion of nitrogen from an electrical discharge [26, 21] as well as after excitation by electronic impact on O_2 doped N_2 solids [74], and also after excitation of NO doped N_2 solids by VUV lamps [75], by synchrotron radiation or an ArF laser.[71]

The effects of increasing emissions from NO and O_2 molecules in the samples prepared mainly from N_2 molecules and N atoms are of special interest. First, let us consider an analysis of the nanocluster compositions. Nanoclusters were formed in the cold helium gas upon injection of the products of a nitrogen-helium gas phase discharge through the surface of superfluid helium. In the gas mixture N_2:He=1:100 a small quantity of oxygen is present. The ratio of O_2 to N_2 is equal to 10^{-4}. For such a small content of the oxygen in helium gas (10^{-6}) all oxygen molecules should be dissociated in discharge. The dissociation efficiency of N molecules is also high (of order 30%).[5] Part of the nitrogen atoms recombined in the cold dense helium gas, producing the so-called nitrogen afterglow in the jet. We can suggest that the recombination of N and O atoms can only rarely occur in the gas phase to produce NO molecules. NO molecules have a high van-der Waals interaction and become the centers of formation of nanoclusters, which contain mostly N_2 molecules and also small quantities of N and O atoms. From the results of x-ray and ESR investigations of nitrogen-helium condensates, we can estimate the composition of the nanoclusters. As was mentioned earlier, the density of the impurities is of order 10^{20} cm^{-3} and the average size of nanoclusters is equal to 5 nm. This allows an estimate of the number of molecules in the nanocluster to be ~ 5000 and the concentration of nanoclusters to be $\sim 2 \times 10^{16}$cm^{-3}. It is known from ESR experiments that ratio N/N_2 in the sample is approximately equal to 10%.[6] This means that on average 500 nitrogen atoms should be in each cluster. The quantity of O atoms in one cluster should be equal to $5000 \times 10^{-4} = 0.5$. On average each two clusters should have one oxygen atom. Summarizing the above arguments, we can conclude that each cluster in as-prepared samples contain on average of $\sim$4500 N_2 molecules and 500 N atoms. The O atom could be found in half of the nanoclusters and the NO molecules could be found even

more rarely in the nanoclusters of as-prepared samples. In the nanoclusters where the NO molecules are present they reside in the centers of nanoclusters, whereas the N and O atoms mostly occupied the surfaces of nanoclusters.

The structure and content of the nanoclusters makes it possible to understand the observed dynamics of sample luminescence. At the initial stage of sample destruction, diffusion of N atoms led to their recombination and formation of metastable $N_2(A^3\Sigma_u^+)$ molecules. The energy from these molecules is delivered to N and O atoms stabilized in the upper layers of an N_2 cluster. At the same time the nanoclusters fused together forming larger crystallites.[4] Some N atoms and N_2 molecules sublimate from the surfaces of nanoclusters when the temperature had risen substantially. Further increases in the temperature speed up the diffusion rate of atomic nitrogen and provide even more efficient recombination of N atoms and further growth in the sizes of crystallites. As a result the concentration of metastable N_2 $(A^3\Sigma_u^+)$ molecules increased leading to an increase of Vegard-Kaplan N_2 molecular emissions. At this stage the excitation of NO molecules stabilized at the centers of clusters also became possible as well as the formation of new NO molecules due to recombination of N and O atoms, leading to the appearance of NO molecular emission. The following processes are responsible for the formation of the NO excited states and the emission:

$$N_2(A^3\Sigma_u^+) + NO(X^2\Pi) \rightarrow N_2(X^1\Sigma_g^+) + NO(a^4\Pi); \tag{2.23}$$

$$N(^4S) + O(^3P) \rightarrow NO(a^4\Pi); \tag{2.24}$$

$$NO(a^4\Pi) \rightarrow NO(X^2\Pi) + h\nu \ (M\text{-}bands); \tag{2.25}$$

$$N_2(A^3\Sigma_u^+) + NO(X^2\Pi) \rightarrow N_2(X^1\Sigma_g^+) + NO(B^2\Pi); \tag{2.26}$$

$$N(^2D) + O(^3P) \rightarrow NO(B^2\Pi); \qquad\qquad (2.27)$$

$$NO(B^2\Pi) \rightarrow NO(X^2\Pi) + h\nu \ (\beta\text{-}bands). \qquad\qquad (2.28)$$
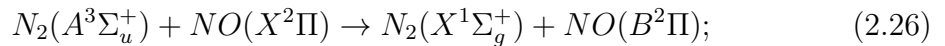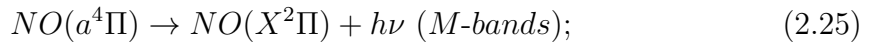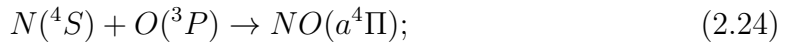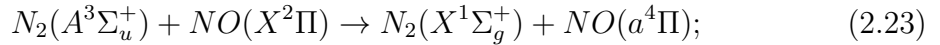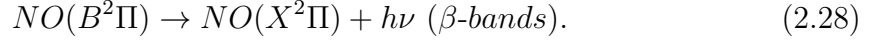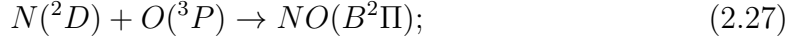
The quenching of metastable $N_2(A^3\Sigma_u^+)$ due to the excitation of NO molecules was studied by Piper $et\ al.$[76] After formation, the NO molecules remained in the nanoclusters due to the higher value of their van-der-Waals interaction compared to that of all other species in the nanoclusters, providing a mechanism for keeping oxygen in the samples. We think that this is the main process for preventing the escape of O atoms initially present in the sample and the accumulation of NO molecules in the nanoclusters. At the final stage of destruction the chain reactions of N atoms lead to a high efficiency of excitation for all species in the sample. At this stage the emission from the species with shorter lifetimes such as O atoms and NO molecules became more efficient. The appearance of the emissions from O_2 molecules at the end of destruction is very unusual. It might be explained as result of recombination of two O atoms. How can two oxygen atoms find each other in the sample with substantially larger concentrations of N atoms? These events have a very low probability. All of the single O atoms should meet N atoms in the sample and form NO molecules. The appearance of pairs of O atoms in close vicinity might be a consequence of the appearance of $(NO)_2$ dimers in the sample. If temperature inside the growing clusters increases to ~ 26 K, the process of dimerization of NO molecules in N_2 matrix becomes very efficient.[77] The increase in local temperature inside the nanoclusters (above the average temperature as measured by thermometer) was possible due to the recombination of N atoms in the nanoclusters. The $(NO)_2$ dimers can react with two N atoms resulting in the release of two oxygen atoms and two nitrogen molecules. Being formed in close vicinity to each other, these two oxygen atoms can recombine, forming excited O_2 molecules which provide the emissions recorded at

the end of destruction, as indicated below:

$$O(^3P) + O(^3P) \rightarrow O_2(c^1\Sigma_u^-); \tag{2.29}$$

$$O_2(c^1\Sigma_u^-) \rightarrow O_2(X^3\Sigma_g^-) + h\nu; \tag{2.30}$$

$$O_2(c^1\Sigma_u^-) \rightarrow O_2(a^1\Delta_g) + h\nu. \tag{2.31}$$
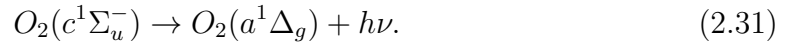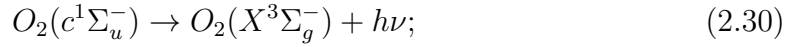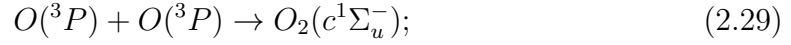
Another possibility to explain the appearance of excited O_2 molecules involves the transfer of excitation from $N_2(A^3\Sigma_u^+)$ molecules to $(NO)_2$ dimers, leading to the formation of two NO molecules. Following the reaction of NO molecules with N atoms[78], two O atoms can also be produced in close vicinity. These pairs of O atoms can recombine and create excited states of O_2 molecules.

3. QUANTUM VORTICES AND THERMALLY INDUCED LUMINESCENCE OF NITROGEN NANOCLUSTERS IMMERSED IN LIQUID HELIUM

We studied thermoluminescence of ensembles of molecular nitrogen nanoclusters, containing stabilized nitrogen atoms, immersed in liquid helium. We obtained experimental evidence for quantum vortex induced chemical reactions for nitrogen atoms in HeII leading to the appearance of luminescence. Thermoluminescence was also observed in HeI due to the process of nanocluster association resulting in thermal explosions of a small fraction of nanoclusters. This research opens new possibilities for studying a broad range of chemical reactions initiated by quantum vortices in HeII and for studying quantum turbulence in porous materials.

3.1 Theoretical background

In this section, we will introduce a brief physical properties of liquid helium and superfluidity, the two-fluid model and quantum vortices. It will help us to explain the effects taking place in the experiments, such as thermoluminescence which was observed in He I and He II.

3.1.1 He I and He II

In the experiments we start with helium-4 above 2.17K which is the normal liquid with characteristics behaving like a Newtonian fluid. As shown in a phase diagram figure 3.1, He I boils at 4.2 K at atmospheric pressure, and compare to the all other substances, the solid state is only obtainable in helium at pressure above 25 bar. When He I is cooled to a lower temperature, a phase transition occurs across so-called λ-point of ^4He in the phase diagram. The transition occurs at the temperature of
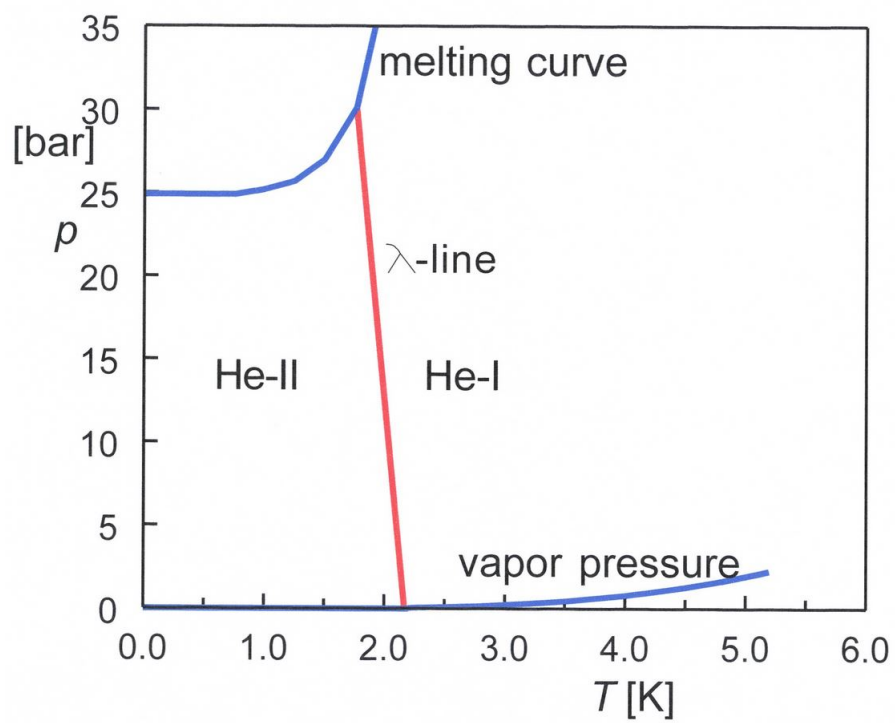
Figure 3.1: Phase diagraam of ^4He.

2.177 K under the saturated vapor pressure of liquid helium. As shown by the specific heat in figure 3.2, the name lambda-line comes due to the temperature plot which is resemble to the Greek letter λ. We have performed the experiments described in this work mostly at very low temperatures. Below the λ-line the liquid is known as superfluid helium which is mostly referred to as He II. The superfluid state has remarkable properties such as zero viscosity, and zero entropy, and an extraordinary high thermal conductivity, though He II shows all these truly exceptional property only at absolute zero. Another remarkable feature of the new state is the appearance of vortices with quantized circulation.

3.1.2 The two-fluid model and quantum vortices

Below the λ-point the liquid is not purely a superfluid as long as for temperatures above absolute zero. He II can be regarded as two interpenetrating fluids: a normal fluid and superfluid with different velocity fields and density, ν_n and ρ_n and ν_s and ρ_s, respectively. The sum of the densities of the two liquids gives the total density of the liquid: $\rho = \rho_s + \rho_n$. Laszlo Tisza first propsed the two-fluid model and Dingle presents this model as shown in figure 3.3. The ratios of the respective densities ρ_s/ρ and ρ_n/ρ vary with temperature in the way shown in figure 3.3. Below 1 K the helium is almost pure superfluid phase. On the other hand, at the lambda point He II is completely normal fluid.

According to Landau, the equation of motion for two fluid system can be found as

$$\rho_n \frac{\partial \nu_n}{\partial t} = -\frac{\rho_n}{\rho} \nabla P + \rho_s S \nabla T + \eta \nabla^2 \nu_n \tag{3.1}$$

$$\rho_s \frac{\partial \nu_s}{\partial t} = -\frac{\rho_s}{\rho} \nabla P - \rho_s S \nabla^2 \nu_n \tag{3.2}$$
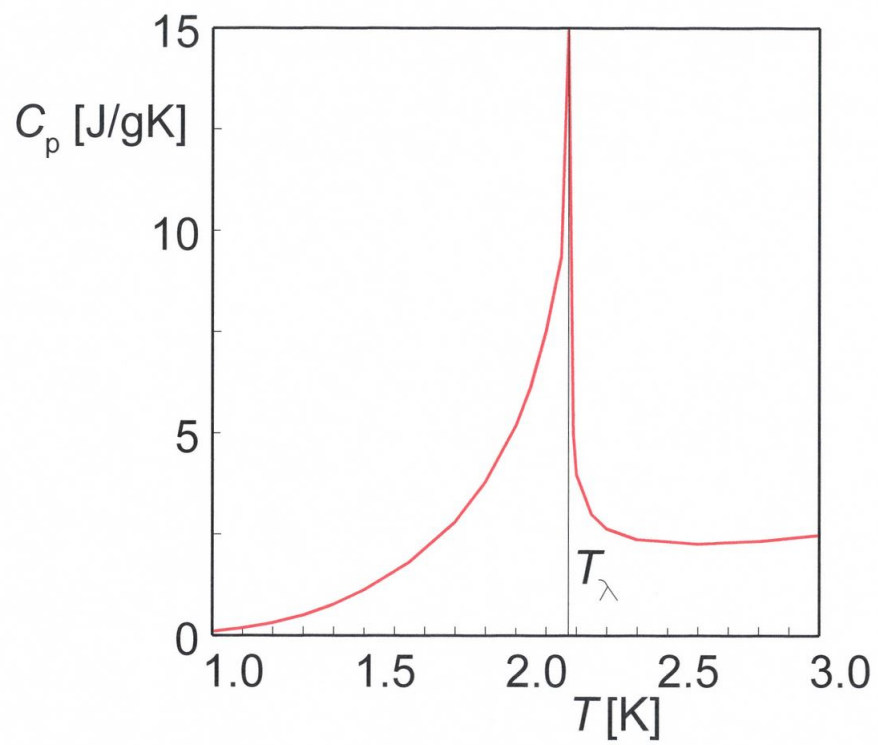
Figure 3.2: Heat capacity of ^4He at saturated vapor pressure as function of the temperature.
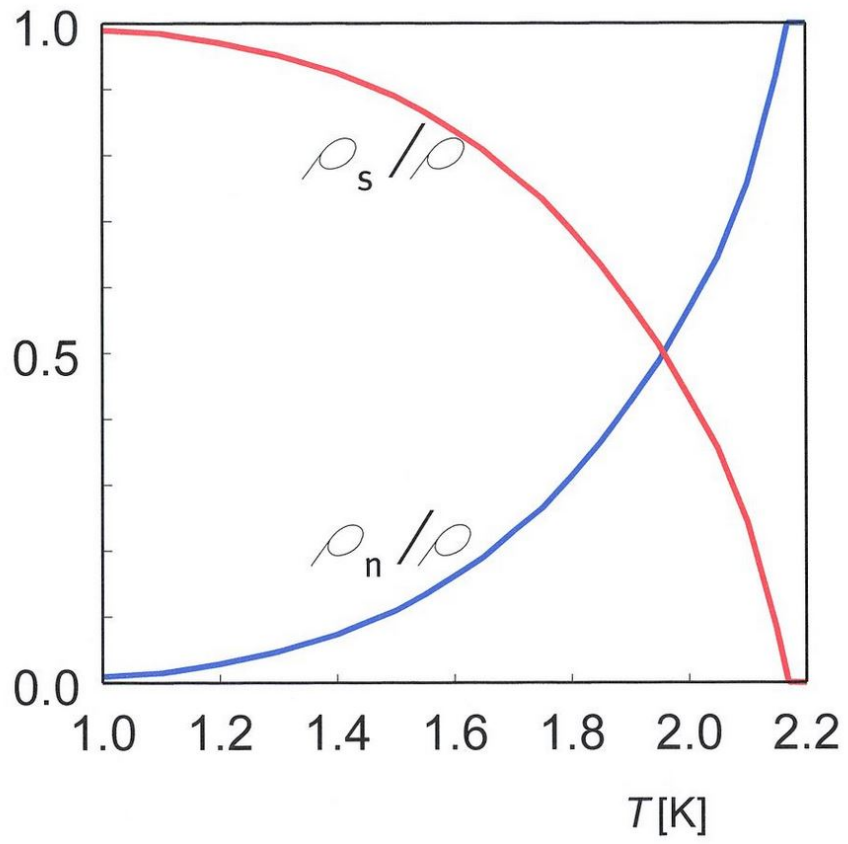
Figure 3.3: Temperature dependence of the relative normal and superfluid components ρ_s/ρ and ρ_n/ρ as functions of T.

where S is entropy, P pressure, η viscosity, and T temperature.

Due to the the quantum mechanical probability current $\overrightarrow{j}$, the flow is completely irrotational in the bulk of the superfluid helium;

$$\overrightarrow{j} = \frac{\hbar}{2mi}(\Psi^*\nabla\Psi - \Psi\nabla\Psi^*),\tag{3.3}$$

Here $\hbar$ is the Planck constant, m is the particle mass, and i is the imaginary unit. When we insert the Madelung transform $\Psi = \sqrt{\rho_s}e^{i\phi}$, where ρ_s represents the number density of the superfluid helium part, and ψ is the order parameter's phase. $\overrightarrow{j}$ can be expressed as;

$$\overrightarrow{j} = \frac{\hbar\rho_s}{m}\nabla\phi,\tag{3.4}$$

This probability current is the mass flux per unit area, in units of kg/(sm^2). To obtain the superfluid velocity field, divide by the superfluid density;

$$\overrightarrow{\nu_s} = \frac{\hbar}{m}\nabla\phi,\tag{3.5}$$

As a result,

$$\nabla \times \overrightarrow{\nu_s} = \nabla \times (\frac{\hbar}{m}\nabla\phi) = 0.\tag{3.6}$$

This equations yields the result that the vorticity of the superflow is zero everywhere in the fluid. It was not correct totally at any point in the fluid since the superfluid can have circulation.

According to the Stokes theorem, $\nabla \times \overrightarrow{\nu_s} = 0$ can be expressed as

$$\oint \nu_s d\mathbf{r} = 0,\tag{3.7}$$

49

where the integration is taken any contour in the fluid. However, we can rewrite the above expression in terms of the superfluid velocity, and the complex field Ψ that remains single valued if the macroscopic phase ϕ changes by $\pm 2\pi n$, where n is an integer.

$$\oint_c \overrightarrow{\nu_s} \cdot \overrightarrow{dl} = \oint_c (\frac{\hbar}{m}\nabla\phi) \cdot \overrightarrow{dl} = \frac{\hbar}{m}(2\pi)n, n = 0, 1, 2.... \quad (3.8)$$

As a result, for $n = 0$ the circulation is zero, and for the case of $n = 1$ we named this feature quantized vortex.

Where (3.8)

$$\kappa_0 = \frac{2\pi h}{m}, \quad (3.9)$$

is the quantum circulation with $\kappa_0 = 9.97 \times 10^{-8} m^2/s$ in He-4.

According to the two-fluid model, heat transport through superfluid helium is as follows; basically, heat is transported by opposing superfluid flow and normal fluid flow giving a counterflow. Superfluid part rushes toward at the hot surface where it receives energy, and as a result it is converted to normal state. A very effective way of transporting heat due to the counter flow of the two fluids for He II leads to an immense effective thermal conductivity. The counterflow can be characterized by ν_{ns} which is the difference in velocities between the normal fluid and the superfluid parts averaged over time and space.[79] Tough et al.[80] shows that the flow becomes unsteady at counterflow velocities of a few mm/s for small channels. Superflow becomes turbulent above a certain critical heat flux. The critical velocity $\nu_c \sim$ $0.2cm/s$ is temperature independent. Vortex lines are generated and the vortex line density is $L^{1/2} = \gamma(T)(\nu - \nu_c)$, where ν is the mean superflow velocity and the coefficient $\gamma(T)$ has been measured experimentally.[81]

3.2 Experimental setup and method

The sample preparation method in this section is almost the same as the one described in previous section. The main difference is that the experimental setup enables simultaneous electron spin resonance (ESR) and optical studies of nanoclusters with stabilized free radicals. The ESR measurements were collected on a Bruker spectrometer operating in the X-band (8.91GHz). The cryogenic fluids are contained in a Janis Super VariTemp (SVT) liquid helium cryostat, whose tail was centered between the pole faces of a homogeneous Varian 7800 electromagnet (see figure 3.4). The Janis cryostat incorporated in a variable temperature insert (VTI), which is thermally insulated from the main 4K helium bath. The main helium bath and VTI are connected via a needle valve which allows helium flow from the main reservoir into the VTI. Figure 3.5 shows a homemade insert for sample formation and optical and ESR investigations of atoms contained in the IHCs. ESR measurements were taken for samples immersed in superfluid helium at ~ 1.32 K which can be achieved by pumping on the VTI with a roots blower backed by a mechanical pump. Gas mixtures containing N_2 and (Ne, Ar and Kr) atoms along with helium gas were prepared in a container at room temperature and transported through Mass Flow Controller (a Brooks Model 5850E) with a constant flux of 5×10^{19} particles/sec to the cryogenic region. When the prepared gas mixtures pass through a quartz capillary surrounding by liquid nitrogen, high-power radio-frequency (f$\sim$53 Mhz, power$\sim$ 75 W) was applied to electrodes which were placed around the lower portion of the capillary to dissociate the nitrogen molecules into atomic free radicals. The presence of the helium gas in the gas mixture increase the efficiency of dissociation of the N_2 molecules in the discharge due to interaction between the energetic metastable helium atoms and impurity atoms. A gas jet was created as the mixed gases passed

51

LIQUID NITROGEN
FILL / VENT

VARIABLE TEMPERATURE INSERT
(VTI)

NEEDLE VALVE

LIQUID HELIUM FILL

KF FLANGE FOR
VACUUM JACKET

CRYOSTAT

JANIS
RESEARCH

CRYOSTAT SUPPORTS

MAGNET

WINDOW
MAGNETOMETER
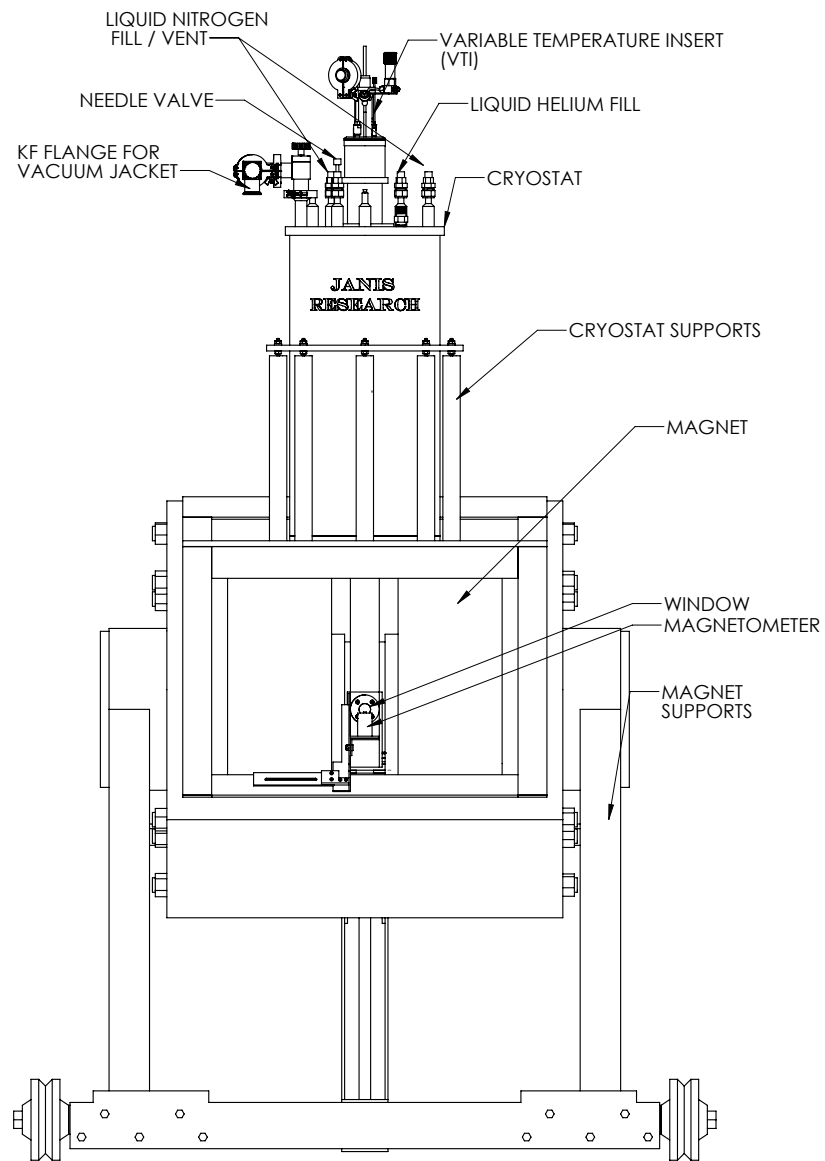
MAGNET
SUPPORTS

Figure 3.4: Magnet and cryostat front view.
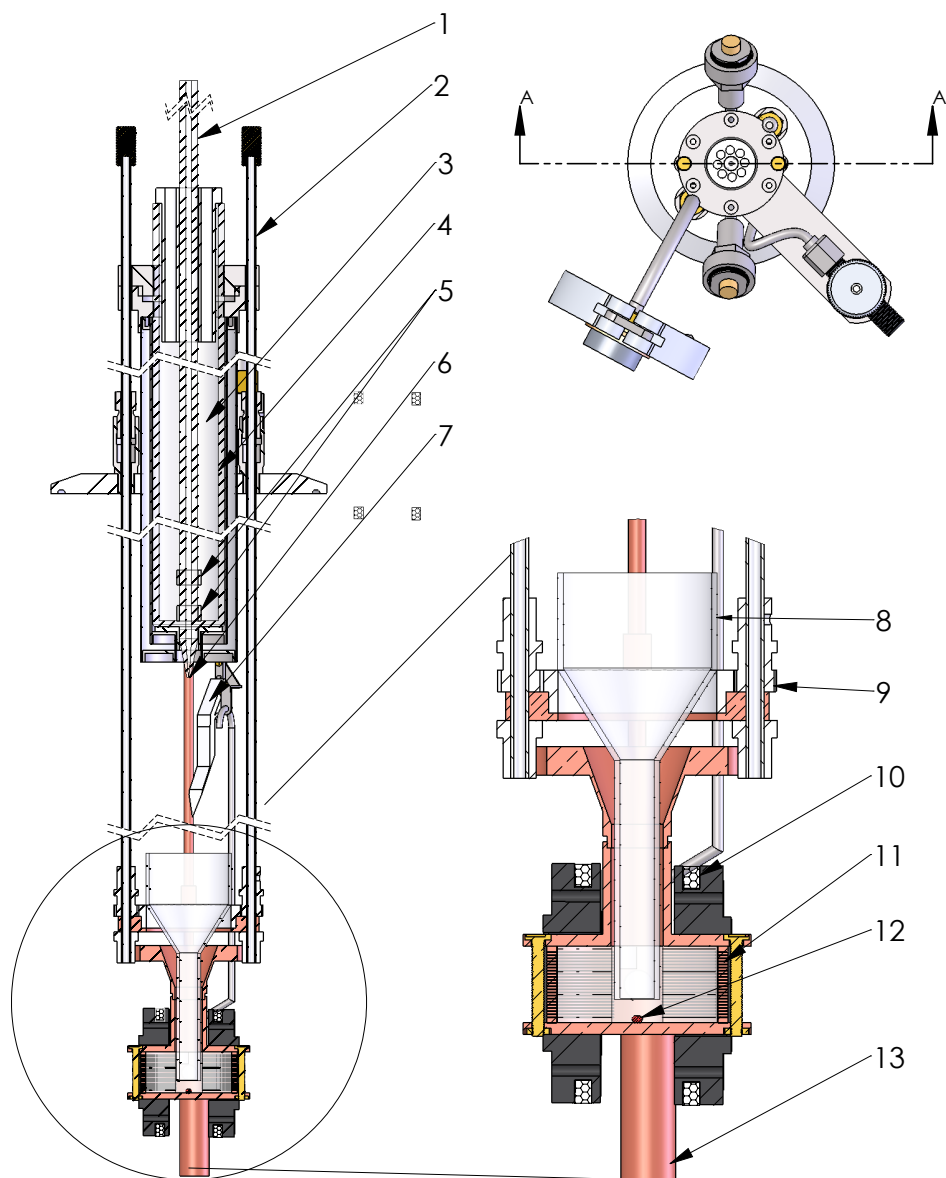
Figure 3.5: Low temperature insert for VTI used in the ESR investigation of IHCs. 1- quartz capillary, 2- tubes for displacement of the beaker in vertical direction, 3- liquid nitrogen, 4- quartz tube, 5- discharge electrodes, 6- orifice, 7- teflon blade, 8- sample collection beaker, 9- beaker rotation gear, 10- modulation coil, 11- horizontal slits on cavity, 12- ruby crystal 13- fountain pump.

through an orifice with diameter 0.75 mm at the bottom of the quartz capillary. The jet impinged on the surface of superfluid helium placed in a small beaker below an orifice at the capillary outlet at a distance of 2.5 cm between the orifice and the top of the beaker. A fountain pump placed at the bottom of the liquid helium bath in the VTI maintained a constant level of superfluid helium in the beaker. Once the jet meets cold helium vapor evaporating from the liquid helium, formation of nanoclusters containing nitrogen molecules and N and O atoms trapped in the clusters took place. The presence of oxygen in the samples is due to the small contamination of oxygen in the helium (1ppm) gas. The jet penetrated through the superfluid He surface and a gel-like sample was created. This process continued as sample was accumulated on the conical part of the beaker. A set of teflon blades was employed to scrape the sample from the walls of the funnel while the beaker was rotated so that all of the sample collected onto funnel surface fell into the cylindrical part of the beaker. Sample accumulation lasted 10 min. During the sample formation, the temperature was 1.5 K which was maintained with the aid of the needle valve.

Once we have $\sim$ 0.3-0.4 cm^3 of sample in the cylindrical part of the beaker, sample accumulation was terminated, and the beaker was lowered into the ESR cavity by a pair of sliding tubes. The lower part of the cryostat with the experimental cell is shown in figure 3.5. The cavity operating in the TE$_{011}$ mode was situated at the bottom of the cryostat in the center of an electromagnet, allowing optical access to the sample. ESR signals were typically detected for samples immersed in superfluid helium at $\sim$1.32 K. The level of liquid helium in the sample tube was measured by a superconducting wire sensor connected to an LM500 level meter. The modulation frequency was set at 100 kHz, and derivatives of the ESR absorption lines were obtained at magnetic field $\sim$0.32 T by a lock-in amplifier. For recording
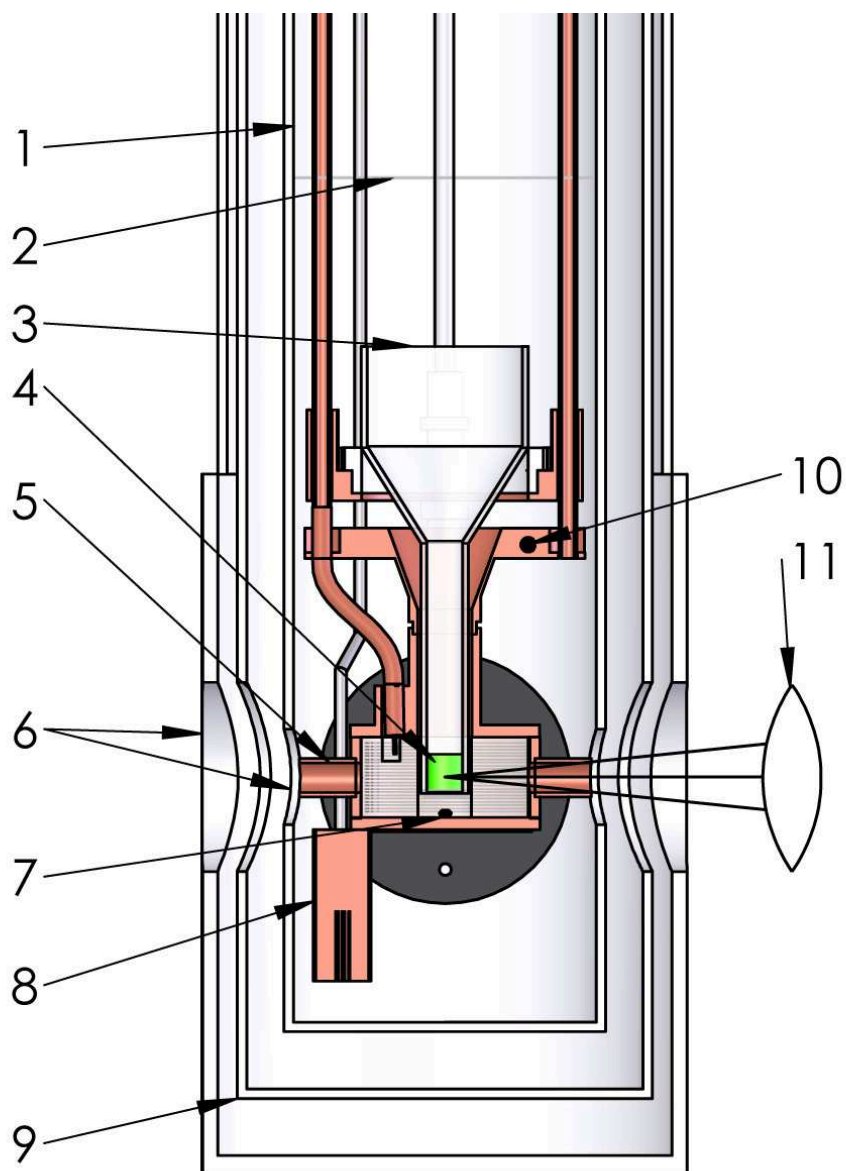
Figure 3.6: Schematic of the set-up for electron spin resonance and spectroscopic study of the ensembles of nanoclusters immersed in liquid helium. 1-sample tube containing the main helium bath, 2-level of liquid helium in the sample tube, 3-quartz beaker, 4-sample, 5-microwave cavity with optical access, 6-quartz windows, 7- ruby crystal, 8-fountain pump, 9-liquid nitrogen shield, 10-thermometer, 11-lens for collecting light from the sample.

the ESR spectra of stabilized atoms we used a Bruker EPR EMX console. ESR measurements were initially performed to provide an estimate of the average and local concentrations of $N(^4S)$ atoms. After that, we ceased the pumping on the helium vapor from the sample reservoir, and let the temperature rise from T$\sim$ 1.32 to 2.16 K. The temperature of the sample was recorded with a germanium thermometer attached to the top of the cavity. Warming up the nitrogen-helium condensates led to intense thermoluminescence. The emitted light passes through the fused silica quartz cylinder in the cavity, then through the holes in the microwave cavity, and finally through the quartz window in the cryostat. The window material and the fused silica quartz are transparent for the wavelength range 200-1100nm. In this experiment, the luminescence from the sample was collected by a lens attached to the end of an optical fiber (see 11 on Fig.3.6).The fiber then transfers light to the entrance of the Andor spectrometer. The Shamrock SR-500i Andor spectrometer with a 0.52 nm (1st grating) resolution, was equipped with a cooled EM-CCD (Newton 970) camera. The emission specrta are detected by the Andor spectrometer with a 150 lines/nm grating (blaze wavelength 500 nm), and a wavelenght range of 340 nm (mostly λ nm= 240-580 nm) with a Newton CCD detector unit cooled to -60 C. During the sample warm up, the registration times of spectra were 50 ms. We opened the main pumping line just before passing the λ-point and cooled down the liquid helium with the sample to an initial temperature T$\sim$ 1.32 K and then would perform ESR registration.

Table 3.1: Average concentration of N atoms in the samples prepared from different nitrogen-helium gas mixtures.

Gas mixtures $[^{14}N_2]/[He]$	Average concentration, cm^{-3}
1/100	5.09×10^{18}
1/400	2.47×10^{18}
1/800	1.21×10^{18}

3.3 Experimental results and discussion

3.3.1 ESR measurements of nitrogen atoms stabilized in N-N$_2$-He samples immersed in superfluid helium

The ESR method can provide the spectroscopic signature for N atoms stabilized in solid matrices. Linewidth, hyperfine splitting and g-factor can be obtained from the shape and position of the ESR spectra. From this data, the average and local concentration of N atoms were determined in our work. To obtain the average concentration of N(^{4}S), we permanently placed a ruby crystal at the bottom of the microwave cavity (see figure 3.5), and the calibration of the signal from ruby crystal was made by reference to a diphenyl-picrylhydrazil (DPPH), sample with a known number of spins $\sim 2.4 \cdot 10^{17}$. We thus used the ruby crystal as a secondary standard. The average concentrations of N(^{4}S) were calculated by comparison between double integrals of ESR signals of the N(^{4}S) atoms and that from ruby signals under the same experimental conditions. Table 3.1 shows the average concentrations of N atoms stabilized in the samples prepared from different nitrogen-helium gas mixtures.

We also determined the local concentration of N atoms from the broadening of the ESR spectra. The characteristic features of the ESR spectra of N atoms in as-prepared samples of nitrogen-helium condensates are the broad wings and weak triplet at the central part. All these features of the spectra were fitted with a sum of three triplets of Lorentzian lines, as shown in figure 3.7. The fitting process was performed by a Graphic User Interface (GUI) program written in Matlab. This GUI program can simulate the experimental signal using up to eight Lorentzian/Gaussian function components. It automatically searches for the best hyperfine splitting constant and line-width corresponding to each triplet. When the difference between

the simulated and experimental curves becomes minimal, the program stops searching and gives the corresponding parameters. Figure 3.7(a) shows an experimental ESR spectrum for N atoms in the collection of nanoclusters prepared from the $[^{14}N_2]/[He]=1/100$ gas mixture, and the sum of the three fitting triplets which provide a rather good agreement to the experimental spectra. Figure 3.7(b) shows three fitting lines composed from the triplets with different hyperfine splittings and line widths. Each of the triplets is assigned to atoms in specific environments. A similar analysis was performed on all spectra obtained for samples prepared from different nitrogen-helium gas mixtures. The results of this analysis are presented in Table 3.2.

The local concentrations of N atoms were obtained[82] from equation

$$\Delta H_{pp} = 2.3g\mu_0\sqrt{S(S+1)}n_l, \tag{3.10}$$

(3.10) was modified for N atoms ($n_l=5.4 \cdot 10^{18} \Delta H_{pp}$) where ΔH_{pp} is the peak to peak width of the ESR lines in Gauss, and n_l is the local concentration of the atoms per cm^3. In a previous study, it has been found that the spectrum with larger line widths belongs to the N atoms located on the surface of the N_2 nanoclusters, and the smaller line width can be assigned to N atoms stabilized inside the N_2 nanoclusters. From the results obtained for different nitrogen-helium samples, we can conclude that decreasing the size of the nanoclusters by reducing content of N_2 molecules in a condensed nitrogen-helium gas mixture leads to increasing of local concentration of N atoms residing on the surfaces of the N_2 nanoclusters.

Table 3.2: Hyperfine constants, A, peak to peak line widths, ΔH_{pp}, and local concentrations of N atoms in nitrogen-helium condensates obtained from ESR line fittings.

Gas mixtures, N_2:He	Curve type	A, G	ΔH_{pp}, G	Local concentration, n_N cm^{-3}	Weight, %	
1:100	Lorentzian	4.00	19.1	$1.03 \cdot 10^{20}$	77.9	
	Lorentzian	4.20	8.7	$4.69 \cdot 10^{19}$	18.4	
	Lorentzian	4.10	3.2	$1.73 \cdot 10^{19}$	3.7	
1:400	Lorentzian	4.00	24.7	$1.33 \cdot 10^{20}$	80.2	
	Lorentzian	4.20	10.1	$5.45 \cdot 10^{19}$	19.8	
1:800	Lorentzian	4.00	35.2	$1.90 \cdot 10^{20}$	67.2	
	Lorentzian	4.20	12.5	$6.75 \cdot 10^{19}$	32.8	
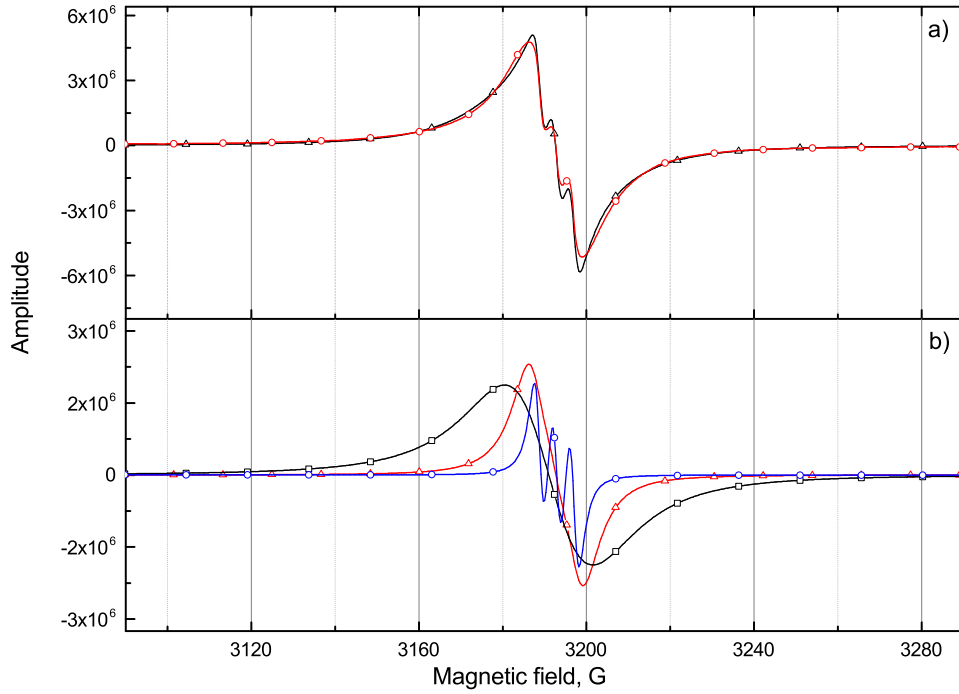
Figure 3.7: Experimental ESR spectrum of N atoms for an as-prepared nitrogen-helium sample formed by the $[^{14}N_2]/[He]=1/100$ gas mixture is shown as a black line with open-triangles (a). The sum of the fitting lines is shown as red line with circles (a). Three triplet of fitting lines used for decomposing the experimental ESR spectrum are shown in (b): blue line with circles is a triplet of Lorentzian lines with the width 3.2 G, red line with open triangles is a triplet of Lorentzian lines with the width 8.7 G, black line with squares is a triplet of Lorentzian lines with the width 19.1 G.

3.3.2 Studies of thermoluminescence during warming up of N-N_2-He samples immersed in superfluid helium

We warmed up the samples immersed in liquid helium, by closing off the pumping of helium vapors from the sample tube and waited as the temperature rose from T $\sim$ 1.2 to 2.16 K. After that we pressurized the cryostat with helium gas to 780 torr and waited as temperature of the sample increased to 4.4 K. Then we opened the main pumping line and cooled down the liquid helium along with the sample to T $\sim$ 1.32 K. Usually warming up to T $\sim$ 2.16 K lasted $\sim$ 8 min and warming up to T $\sim$ 4.4 K lasted $\sim$ 35 min. The level of liquid helium in the sample tube was measured by a superconducting wire sensor connected to an LM500 level meter.

We studied the thermoluminescence of nitrogen-helium condensates containing stabilized nitrogen atoms during the entire temperature sweeps. Warming up the nitrogen-helium condensates led to intense luminescence. Figure 3.8a shows the dynamics of thermoluminescence of a nitrogen-helium sample prepared from the gas mixture [N_2]:[He] =1:400 in the spectral range of 260 - 600 nm. The integrated intensity of the spectra obtained during the thermoluminescence process is shown in figure 3.8b. The α-group, the α'-group of nitrogen atoms, the β-group of oxygen atoms and Vegard-Kaplan (VK) bands of N_2 molecules are present in the spectra. The α-group corresponds to the $^2D \rightarrow {}^4$S transition of nitrogen atoms, the β-group corresponds to the ^{1}S$\rightarrow{}^1$D transition of oxygen atoms and the V-K band corresponds to transitions $A^3\Sigma_u^+ \rightarrow X^1\Sigma_g^+$ of N_2 molecules.[62] Figure 3.8c shows the time dependence of α-group and β-group intensities during warming from 1.2 to 4.4 K. There are two intensity maxima of luminescence in this temperature range. The first maximum occurs in superfluid helium at T $\sim$ 1.9 K and the second one appears in normal helium at T $\sim$ 3.25 K. In order to understand the nature of the appearance of two

62
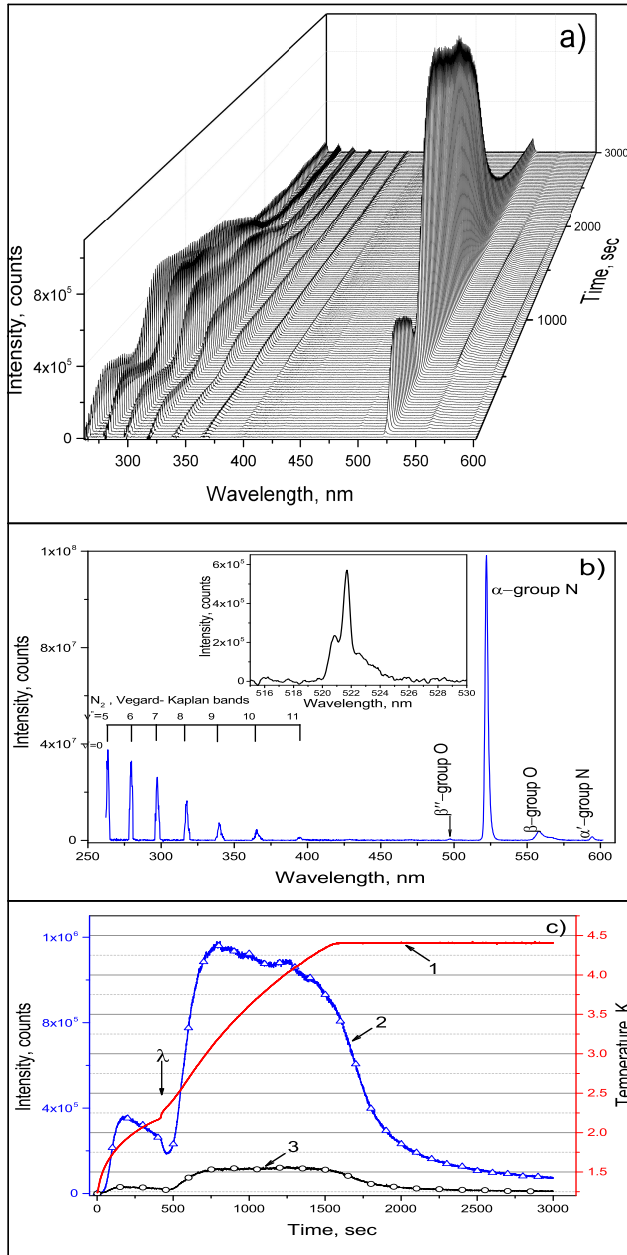
Figure 3.8: Thermoluminescence of nitrogen - helium sample immersed in liquid helium. a) Dynamics of thermoluminescence spectra of nitrogen-helium sample during warming up from 1.3 to 4.4 K. Each spectrum in the figure is a sum of 10 spectra taken with exposure time 10 ms. Sample was prepared from gas mixture $[^{14}N_2]/[He]=1/400$. b) Integrated thermoluminescence spectra obtained during entire warming process. Inset shows spectrum of the α-group obtained with the spectral resolution 0.05 nm. c) Time dependence of sample temperature (1). Vertical arrow shows a position of λ-point. Time dependence of thermoluminescence intensity for nitrogen (2) and oxygen(3) atoms.

63
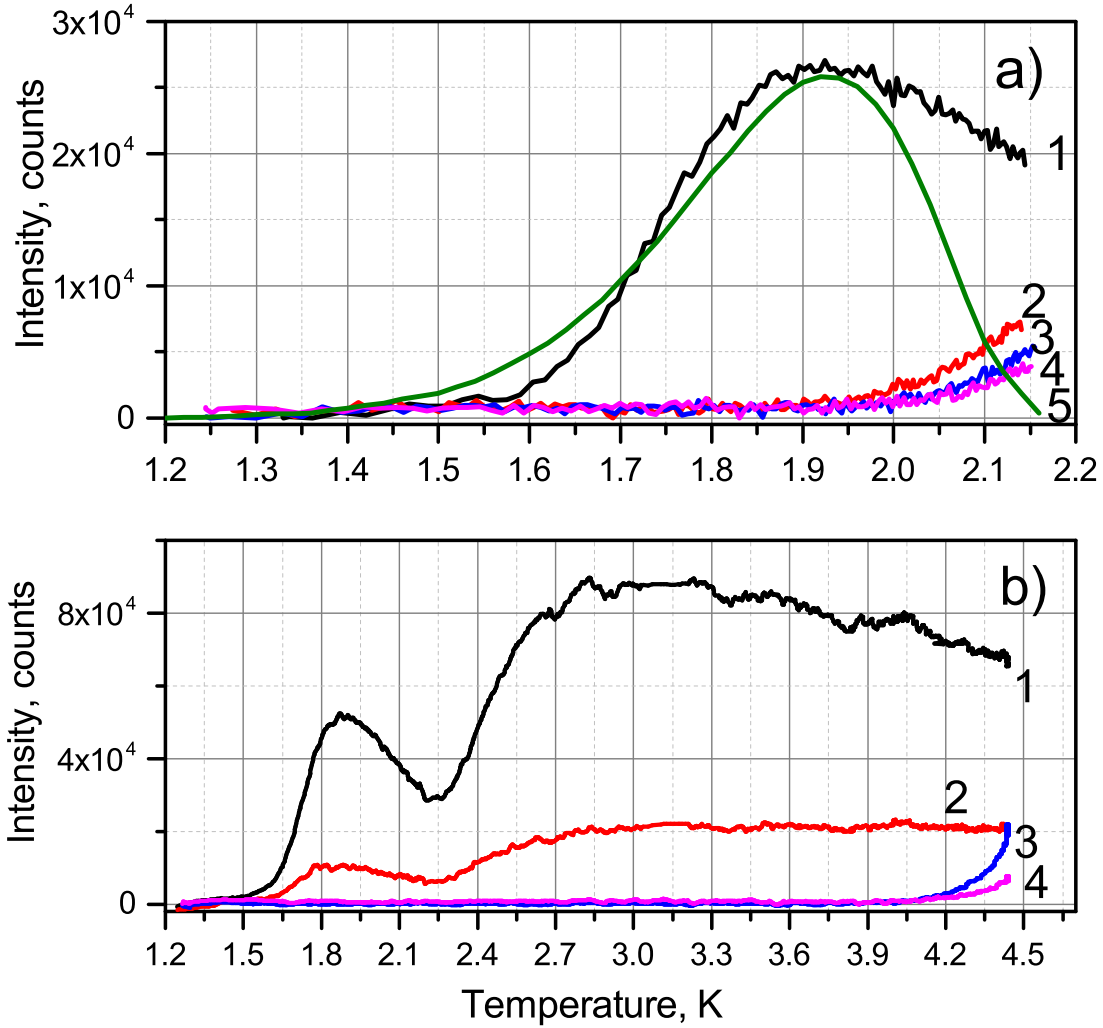
Figure 3.9: Temperature dependence of thermoluminescence of nitrogen-helium condensates. a) Thermoluminescence of nitrogen atoms during warming up from 1.25 to 2.15 K for as prepared sample - 1, during second warming - 2, during third warming - 3, during fourth warming - 4. Heat conductivity function for turbulent HeII - 5.[83]. b) Thermoluminescence of nitrogen (1) and oxygen (2) atoms during warming up from 1.25 to 4.4 K of as prepared sample and during second warming (3) and (4), correspondingly. Samples were prepared from gas mixture $[^{14}N_2]/[He]=1/100$.

maxima in the intensity of thermoluminescence, we studied of the behavior of the samples during cycling of warming up and cooling down of the samples immersed in liquid helium. Figure 3.9a shows the dependence of the thermoluminescence during four consecutive warm ups after subsequent cool downs cycles of a sample immersed in superfluid helium from 1.3 to 2.16 K. Figure 3.9a shows that the thermoluminescence intensity for each successive warming process is completely different. The thermoluminescence starts at a higher temperature and monotonically increases with increasing temperature. Also the intensity of thermoluminescence became smaller for each successive warming process. Next, we studied the temperature dependence of thermoluminescence of a nitrogen-helium sample during the two consecutive warming up processes over an even broader temperature range from 1.2 to 4.4 K and cooling back (see Fig. 3.9b). In this case, during the first warming up of the as-prepared sample, the thermoluminescence intensity has two maxima. However, during the second warm up, the thermoluminescence only starts at a higher temperature, T $\sim$ 4.1 K, which is close to the final temperature (T $\sim$ 4.4) achieved in the first warming, and monotonically increases with temperature (see figure 3.9b).

We assigned the appearance of thermoluminescence to the recombination of nitrogen atoms stabilized in nanoclusters. We performed ESR experiments on the behavior of N atoms during the process of warming the samples immersed in liquid helium.The ESR spectra of N(^{4}S) atoms were obtained for three different samples at temperature T $\sim$ 1.32 K, just before warming the samples and again after cycles of warming up to temperatures of either 2.16 K or 4.4 K followed by cooling down to T $\sim$ 1.2 K. It was found that annealing of the samples to 2.16 K does not change the ESR signals. However, annealing of the samples to 4.4 K resulted in an increase of the ESR signals for two of the samples but does not change the signal of the sample
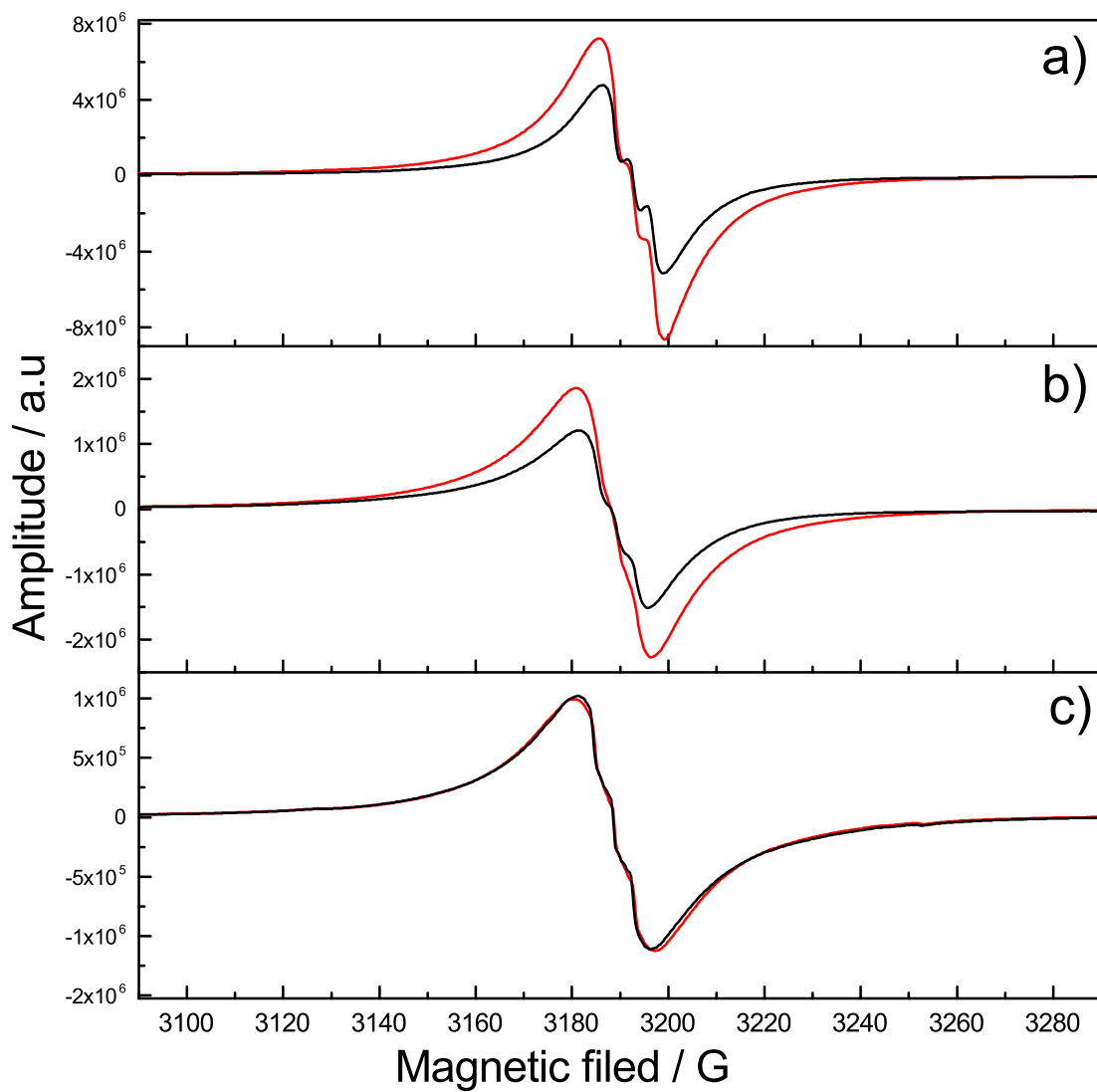
Figure 3.10: Comparison of the ESR spectra for as-prepared samples (black) and after warming to 4.4 K (red). Spectra were obtained for samples prepared from nitrogen-helium mixtures $[N_2]$:$[He]$ = 1:100 (a), 1:400 (b) and 1:800 (c).

prepared from the $[N_2]$:[He] = 1:800 gas mixture(see figure 3.10). All of the samples studied contained high concentrations of stabilized nitrogen atoms. We recorded the ESR spectra of N atoms with the average concentrations in the range between $1 \cdot 10^{18}$ cm^{-3} and $5 \cdot 10^{18}$ cm^{-3} and the local concentrations of atoms which were mostly residing on the surfaces of nanoclusters were even larger $(1 - 2) \cdot 10^{20}$ cm^{-3}. The ESR measurements show that high concentrations of N atoms do not changed during the process of warming samples in liquid helium and do not show any sign of N atom recombination.

We performed experiments to determine the absolute number of photons emitted from the sample prepared from gas mixture $[^{14}N_2]/[He]=1/400$ during the entire process of warming from 1.2 to 4.4 K. A Hamamatsu photomultiplier tube (PMT) R928 was used to detect the emitted light. Figure 3.11 illustrates the scheme for collection of the emitted light from the sample located in the center of the cavity. The emitted light passes along the fused silica quartz cylinder in the cavity, then through the holes in the cavity, and finally through the quartz window in the cryostat. The window material and the fused silica quartz are transparent for the wavelength range 200 nm-1100 nm. The emitted light was collected from the cell at an angle of 11.73°, and guided to the photon-multiplier tube with the help of the lens (f=100 mm). The output of the PMT was fed into a LeCroy Waverunner 62Xi-A Oscilloscope. Figure 3.12 shows the time dependence of the PMT signal for the sample prepared from the $[^{14}N_2]/[He]=1/400$ gas mixture during the process of warming. We also performed a calibration of the PMT response to the light emitted from an Ocean Optics DH-2000 balanced halogen source with known output power (see Fig 3.13a.). For the PMT calibration, we used a dichroic filter transmitting the specific portion of the spectrum (see Fig 3.13b.). A low band-pass filter was also used to attenuate the signal. For
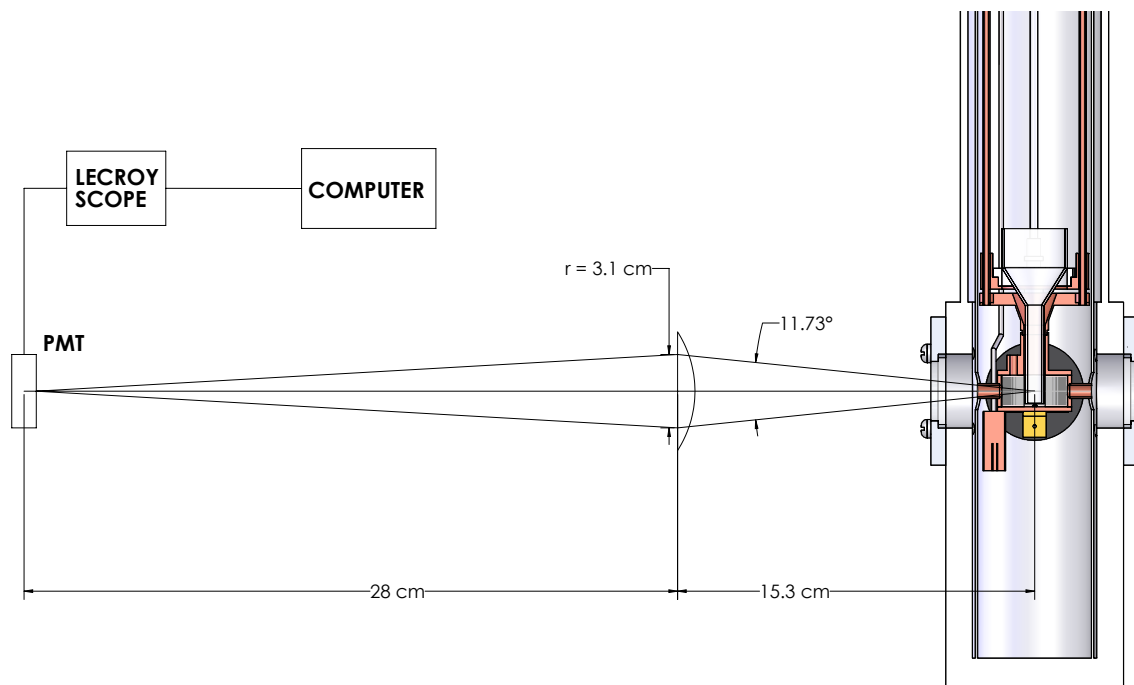
Figure 3.11: Scheme for collection of luminescence from the sample located inside the ESR cavity.
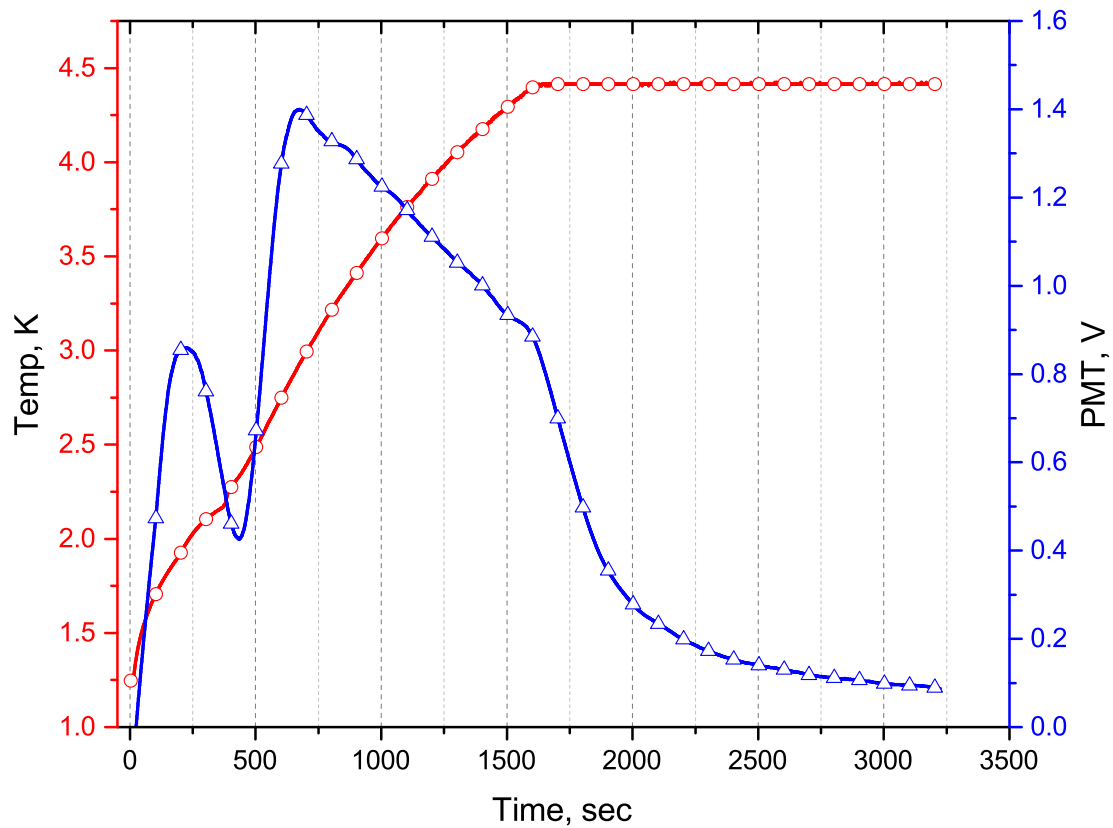
Figure 3.12: Time dependence of the sample temperature denoted as red line with circles, and time dependence of PMT signal denoted as blue line with triangles. The applied voltage to the PMT was 800V.
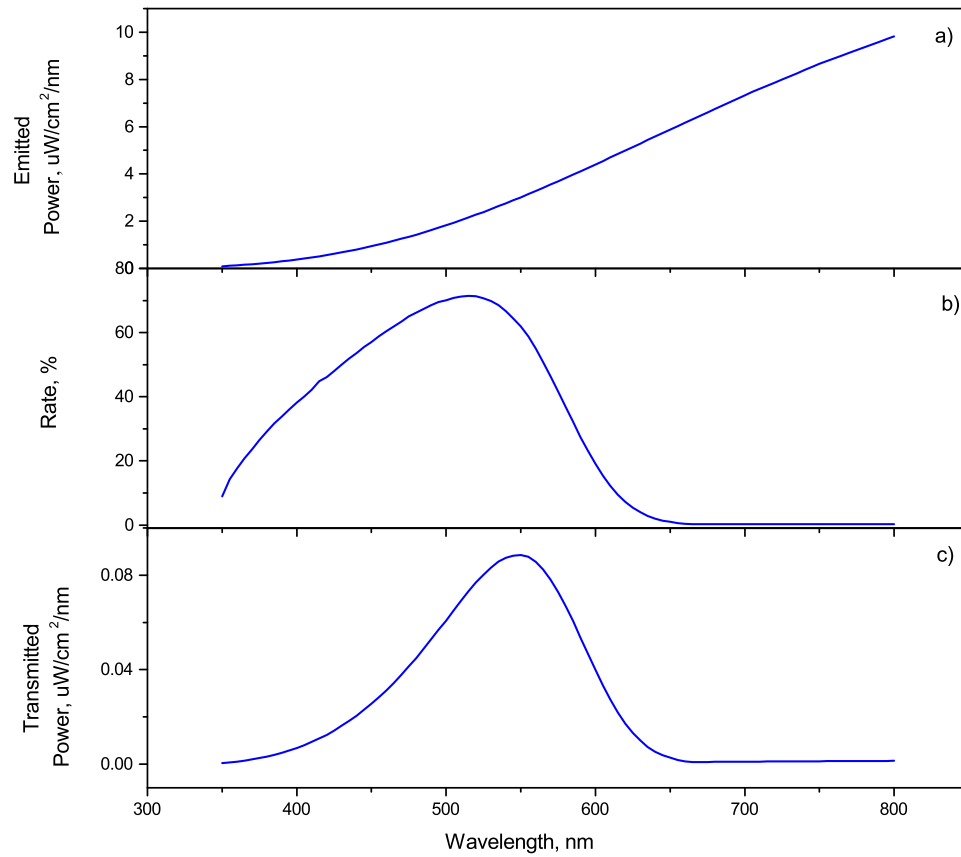
Figure 3.13: a) Emitted power of Ocean Optics DH-2000 halogen lamp. b) Transmission rate for UG18-dichroic filter. c) Transmitted halogen lamp power after filters.

the PMT with an applied voltage of 800 V, a filter with a transmission of 4.75% was used to prevent overloading. After considering the effect of these two filters, the TOTAL power radiated within a given wavelength range was measured to be equal to 11.1 μW/cm^2 (see Fig 3.13c.). Since at the entrance of the source we used a cosine corrector with 39 micron diameter, the overall power reaching the tube is equal to 1.32×10^{-4} μW. For this amount of radiated light to the tube, the read out on the scope was 3.1 V.

This result indicated that, the signal with amplitude 1 Volt on the scope corresponds to 4.27×10^{-5} μW power of light irradiated onto the tube. From Figure 3.12, the integrated signal was calculated as 2411 V·s during the ENTIRE warming of the sample. We collected only the part of the emission from the sample in the solid angle dΩ which can be estimated from the formula:

$$d\Omega = \frac{\pi r^2}{R^2} = 0.033,$$

(3.11)

where above r=1.57 cm is the radius of the circle on the lens which is illuminated, and R=15.3 cm is the distance between the lens and light source. The total energy of the radiated light from the sample during the entire warming period can be calculated as follows:

$$4.27 \times 10^{-5} \frac{\mu W}{V} \times 2411 V \cdot s \times \frac{4\pi}{d\Omega} = 3.92 \times 10^{-5} J,$$

(3.12)

We consider that the most intense emission was from the α-group of nitrogen atoms at $\lambda \sim 523$ nm, and the energy of a photon at 523nm is 3.8×10^{-19} J. We can find the number of emitted photons by dividing the total energy of radiated light from the sample by the quantum of energy of a photon at 523 nm. From these

considerations, the total number of emitted photons from the sample during the entire process of warming up, was found to be $\sim 1 \times 10^{14}$.

This fact means that only a small fraction ($\sim 4 \cdot 10^{-5}$) of all atoms participated in processes generating luminescence. The integrated intensity of thermoluminescence in HeII is approximately one order magnitude less than that in HeI, leading us to the estimate that an even smaller fraction of nitrogen atoms ($\sim 4 \cdot 10^{-6}$) recombine in HeII. Such small magnitudes of changes of N atom concentrations can not be determined by the ESR method.

Thermoluminescence of samples in HeI can be explained by thermal explosions of a small fraction of the nanoclusters initiated by the process of association of nanoclusters. It has been observed in X ray experiments that the nanoclusters grow during warming in HeI[2, 84, 29]. Thus the density of the porous material increases. The increase of the ESR signals of N atoms during samples warming in HeI, observed in this work, also indicate increase of the density of the sample due to the entrance of additional sample material which was initially accumulated in the beaker above the sensitive zone of the ESR cavity. The growth of the nanoclusters and collapsing of the pores in the samples in HeI led to their compression. As the nanoclusters make contact, N atoms on the surfaces recombine, eventually, leading to recombination of other N atoms contained in these nanoclusters. The poor thermal conductivity of liquid helium above T_λ does not allow the heat, released as a result of chemical reactions, to spread rapidly to other nanoclusters.

The observation of thermoluminescence in HeII is an unusual phenomenon even if we consider that nitrogen-helium condensates contain a high density of stored energy. Existing explanations of this phenomenon as a result of association of N(^{2}D) atoms and N_2 molecules in solidified helium[13] and electron-ion recombination of

charged particles stored in the samples[59] are not supported enough by experimental evidence. We explain thermoluminescence in HeII as a result of recombination of nitrogen atoms stabilized on the surfaces of nanoclusters. The process of atom recombination might be initiated by quantum vortices. The temperature dependence of thermoluminescence for an as-prepared sample is similar to the temperature dependence of the thermal conductivity function due to turbulence in HeII (see curve 5 in figure 3.9a) and, more importantly, is similar to the temperature dependence of the mutual friction between the normal and superfluid components of liquid helium.[83] Mutual friction is responsible for the formation of quantum vortices in the counterflow of normal and superfluid components when heat flux is applied. Our estimate of the heat flux during the process of warming up of our samples is 50 mW/cm². This value is larger than the critical value for the creation of turbulence in bulk HeII[79] These facts provide evidence for the importance of the vortices formed in superfluid helium for the initiation of the thermoluminescence of nitrogen atoms at such low temperatures. Vortices can attract and capture in the vortex cores the strands of the sample. The force arising in this process, as well as, the process of reconnection of the vortices can lead to contacts of the surfaces of nanoclusters in different strands. This is the first observation of chemical reactions initiated by vortices in superfluid helium. Suppression of thermoluminescence during the second and later processes of warming can be explained by a reduction in the number of available sites for recombination of nitrogen atoms. This may be a consequence of the formation of chemical bonds between adjacent nanoclusters during the first warm-up. It is clear why thermolumoinescence in HeII is less efficient than in HeI. After recombination of N atoms the N_2 molecules are formed at high vibrational states. The vibrational relaxation of N_2 molecules is rather slow ($\sim$ 1 s)[85, 86] and the energy released can be eas-

ily removed in superfluid helium[83] preventing thermal explosions of nanoclusters containing stabilized nitrogen atoms.

The suggestion that we observed quantum vortices induced thermoluminescence was also supported by experiments with ensembles of nanoclusters with different sizes. Figure 3.14 shows the time dependence of thermoluminescence for samples formed by nanoclusters with different average size. It is known that reducing the ratio of concentration of the impurity relative to that of helium in the gas jet leads to a decrease in the size of nanoclusters forming the samples.[16] Reducing the concentration of N_2 molecules from 1% to 0.25% substantially increases the intensity of luminescence of the sample. During the investigation of the sample prepared from an even more dilute mixture, containing 0.125% of N_2 molecules, we observed a thermal explosion of nanoclusters inside HeII. The local concentration of N atoms stabilized in this sample was equal to $2 \cdot 10^{20}$ cm^{-3}. The explosion provided an intense emission, shown as a sharp peak on the red curve of Fig.3.14. Vortex induced recombination of stabilized atoms in this sample results in the initiation of thermal explosions of only a small fraction of the nanoclusters immersed in HeII as is indicated by the small number of photons detected during the explosion. The ESR signal of N atoms was almost unchanged. The peak observed at T $\sim$ 1.9 K might be a result of two opposite trends; the frequency of thermal fluctuation increases exponentially with temperature while the tension of vortex lines decreases (vanishing at 2.17K) hence, the impact of vortex lines should be strongest somewhere between 1.6K and 2.17K.

Another piece of evidence that thermoluminescence is connected to the density of the vortices in HeII was obtained from our investigations of the decay of thermoluminescence at constant temperatures T=1.82, 1.95, and 2.12 following step heating. The nitrogen-helium sample was prepared from a gas mixture N_2:He=1:400 at T $\sim$
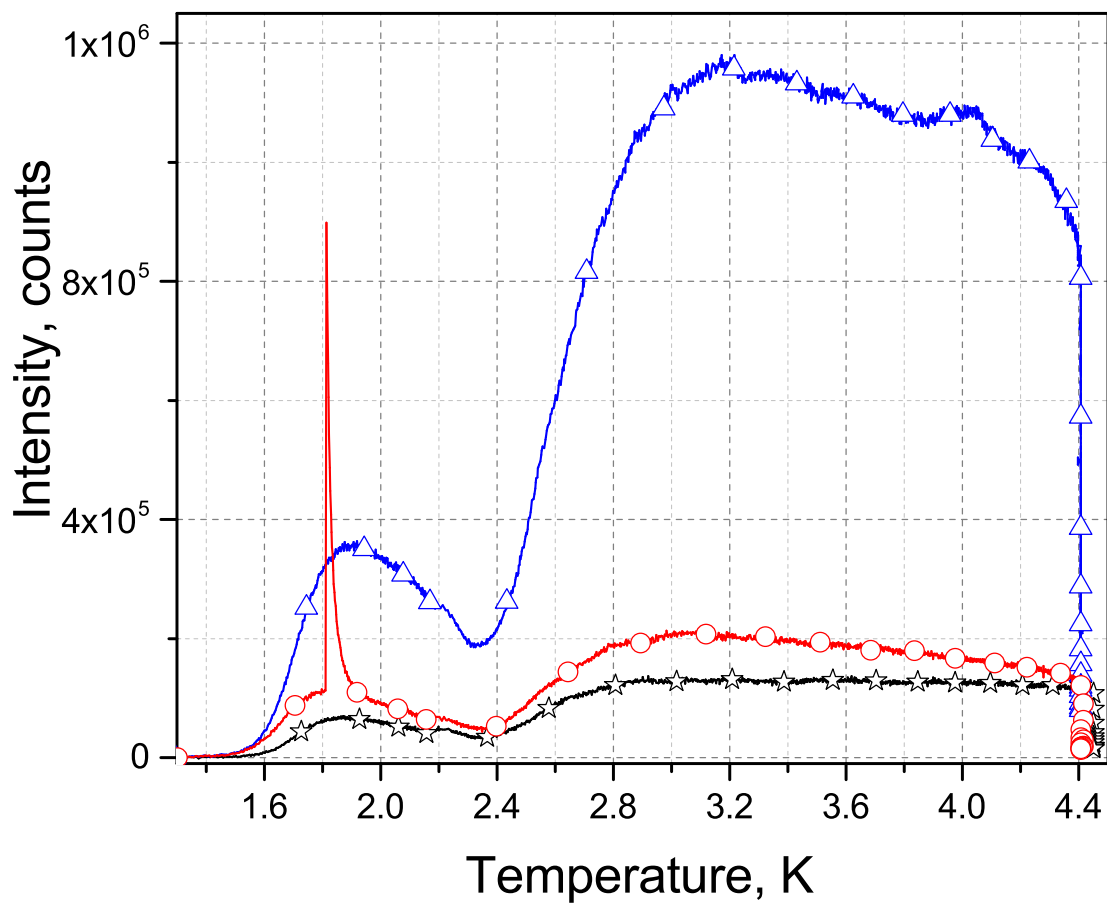
Figure 3.14: Temperature dependence of thermoluminescence intensity of nitrogen atoms for samples formed from different gas nitrogen-helium mixtures: 1:100 (black line with open stars), 1:400 (blue line with open triangles) and 1:800 (red line with open circles).
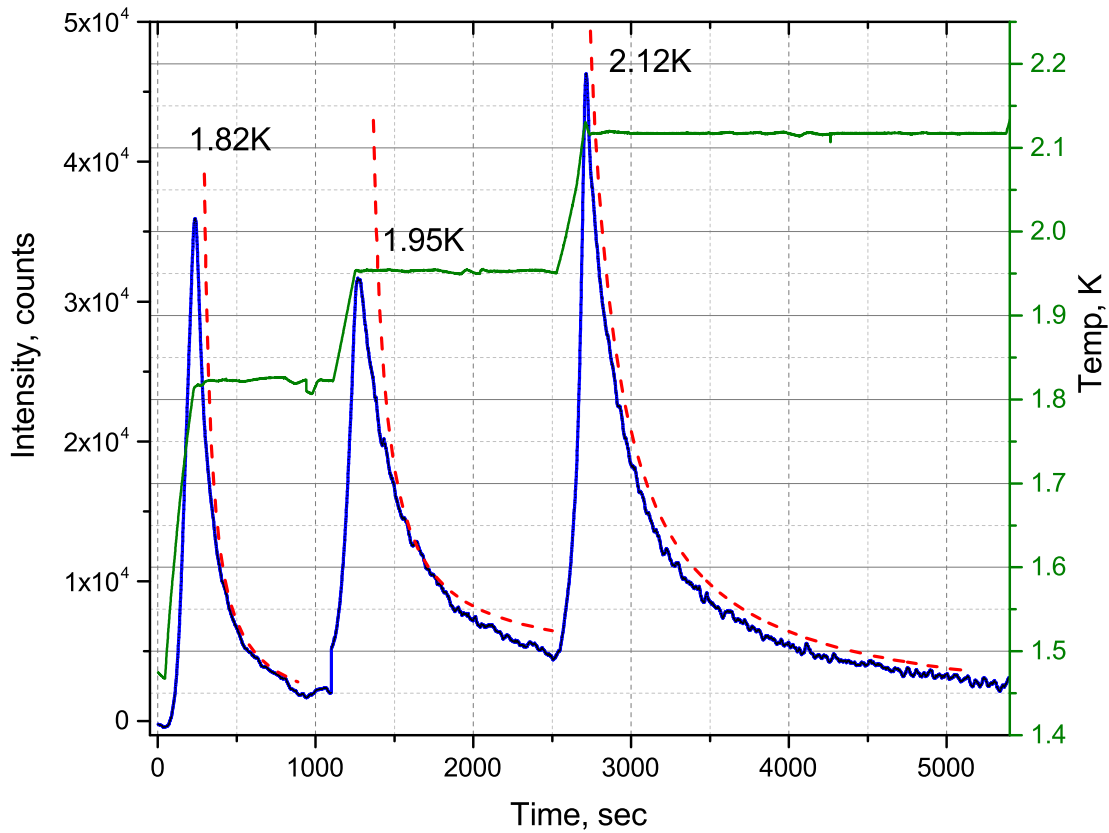
Figure 3.15: Kinetics of thermoluminescence intensity for nitrogen-helium sample (blue-line), under step heating from 1.47K to 2.12K (green-line). Red dashed curves were obtained by computer fitting of experimental results in accordance with a hyperbolic law. The sample was prepared from gas mixtures N_2:He=1:400.

1.5 K during ∼20 min of accumulation. After stopping the discharge, we waited until the afterglow became weak. The sample was submerged inside superfluid helium during the entire warming process. Increasing the temperature led to a strong enhancement of the thermoluminescence. A typical dependence of the thermoluminescence intensity on the temperature of the nitrogen-helium sample during the three-stage step heating is presented in figure 3.15. The time dependence of thermoluminescence intensity (I) at constant temperature is best described by hyperbolic law I∼t^{-1}. A similar result for thermoluminescence decay was also observed in earlier work.[13]. Thus the thermoluminescence decay is consistent with a hyperbolic law decay of the vortex densities in superfluid helium.[87, 88] The long time decay of the vortex density with similar characteristic time (hours) was observed in Ref.[88]. We suggested that the long decay of the vortices occurred in the voids of the sample. From the decay time of the luminescence observed in the experiment the size of the voids in the sample was estimated as following:

$$\tau = \frac{10d^2}{\kappa},$$
(3.13)

where τ is vortex density relaxtion time, d is characteristic size, and κ is quantum circulation given by

$$\kappa = \frac{h}{m_4} = 10^{-3} cm^2 s^{-1},$$
(3.14)

where h is Planck's constant and m_4 is the mass of a ^4He atom. As a result, the size of the voids appears to be as large as ∼0.3cm.

4. OPTICAL AND ELECTRON SPIN RESONANCE STUDIES OF NITROGEN-RARE GASES-HELIUM CONDENSATES IMMERSED IN SUPERFLUID HELIUM

Impurity-helium condensates created by injection of nitrogen atoms and molecules as well as rare gas (RG) atoms (Ne, Ar and Kr) into superfluid ^{4}He have been studied via electron spin resonance (ESR) techniques and optical spectroscopy. Measurements of the ground-state spectroscopic parameters of nitrogen atoms show that the nanoclusters have a shell structure. N and O atoms reside in solid molecular layers of N_2. These layers form on the surfaces of RG (Ar or Kr) nanoclusters. We studied the dynamics of thermoluminescence spectra emitted during the warming of porous N-N_2-RG-He samples inside the superfluid helium. We have shown an experimental evidence that quantum vortices may initiate chemical reactions in porous ensembles of nanoclusters. Using this experimental approach, it is possible to study chemical reactions of heavy atoms and molecules at very low temperatures where normal diffusion and quantum tunneling in solid matrices should not occur.

4.1   Experimental results

The experimental setup for preparing and investigating simultaneous electron spin resonance (ESR) and optical studies of nanoclusters with stabilized free radicals, immersed in liquid helium has been described in more detail in the section 3. In this work, we again injected nitrogen atoms and molecules into superfluid ^{4}He, but additionally we injected rare gas (RG) atoms (Ne, Ar and Kr) into superfluid ^{4}He. First, we investigated the addition of rare atoms (Ne, Ar and Kr) to the condensed

N$_2$-He gas mixture on the efficiency of stabilization of N atoms in IHCs. Second, we also investigated thermoluminescence dynamics during the warming of samples immersed in superfluid helium.

4.1.1   ESR measurements

We performed ESR investigations of the samples formed by injecting the [N$_2$]:[Ne]:[He] and [N$_2$]:[Ar]:[He] gas mixtures with different ratios into HeII. We begin by describing of the effect of addition of Ne gas to the condensed nitrogen-helium gas mixtures. The ratio of nitrogen molecules to neon atoms [N$_2$]/[Ne] in the gas mixtures were changed from 1/50 to 1/1. However, the ratio between the impurity gas ([N$_2$]+[Ne]) and He gas in the mixtures was fixed at 1/20. Figure 4.1 displays the ESR spectra of N atoms in samples prepared from different nitrogen-neon-helium gas mixtures. For the ESR spectra from [N$_2$]/[Ne]: 1/1, 1/5, and 1/50 the amplitudes of the signals were increased by a factor of 4, 2 and 1.3, respectively. We detected very broad ESR spectra of N atoms stabilized in the sample prepared from gas mixture [N$_2$]:[Ne]:[He]=1:1:50. The increasing of the [N$_2$]:[Ne] ratio in the condensed gas mixture led to a increasing of the amplitude and decreasing of broadening of the N atom signal. As we can see the Fig.4.1, the most resolved, spectra of N atoms were obtained for the sample prepared from tha gas mixture [N$_2$]:[Ne]:[He]=1:50:1000.

We also studied the effect of adding different quantities of Ar atoms into the nitrogen-helium gas mixture on the efficiency of stabilization of N atoms in IHCs. The ratio of nitrogen molecules to argon atoms [N$_2$]/[Ar] in the gas mixture was increased from 1/50 to 1/1. However, the ratio between impurity species ([N$_2$]+[Ar]) and He in the gas mixture was fixed to 1/100. In Fig. 4.2, one can see that less resolved ESR spectra are obtained for the sample prepared from the gas mixture

Figure 4.1: Experimental ESR spectra of N atoms stabilized in sample prepared from different nitrogen-neon-helium gaseous mixtures: $[N_2]$:$[Ne]$:$[He]$=1:1:50 (a), $[N_2]$:$[Ne]$:$[He]$=1:5:100 (b), $[N_2]$:$[Ne]$:$[He]$=1:20:400 (c), $[N_2]$:$[Ne]$:$[He]$=1:50:1000 (d). All spectra were obtained at 1.35 K.
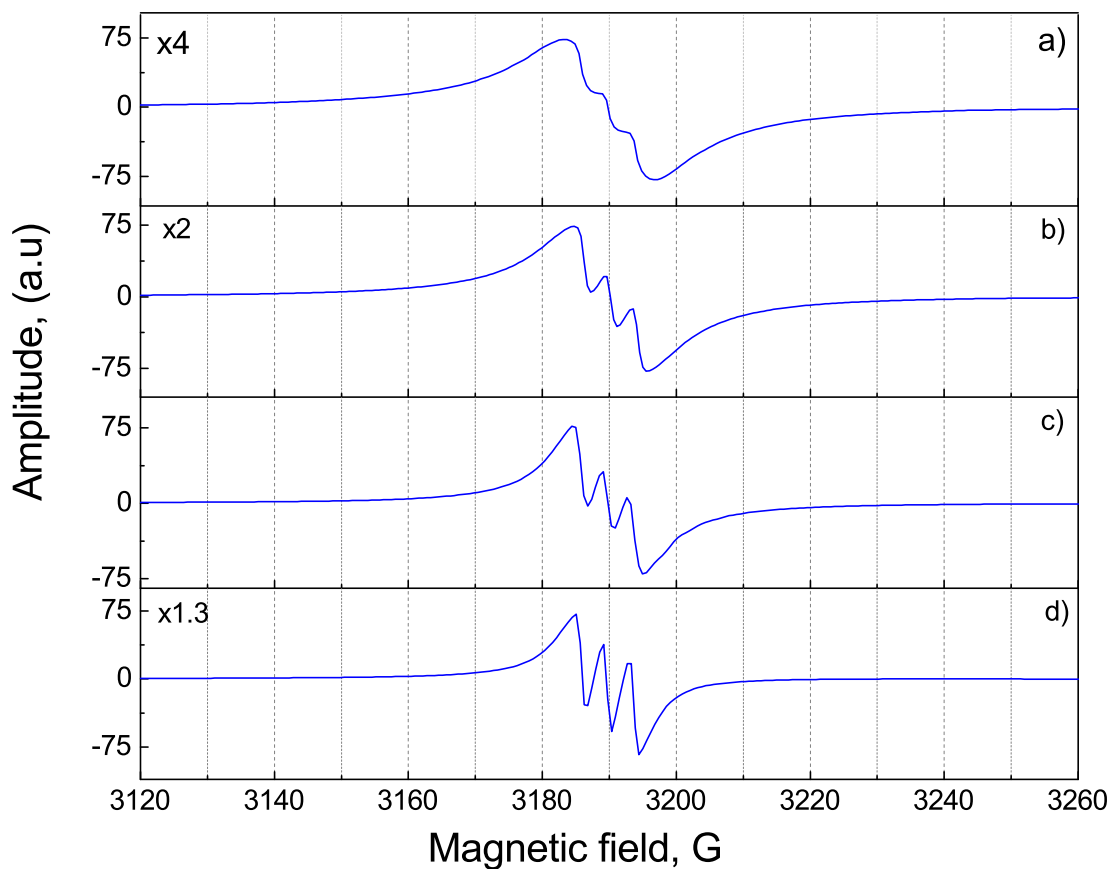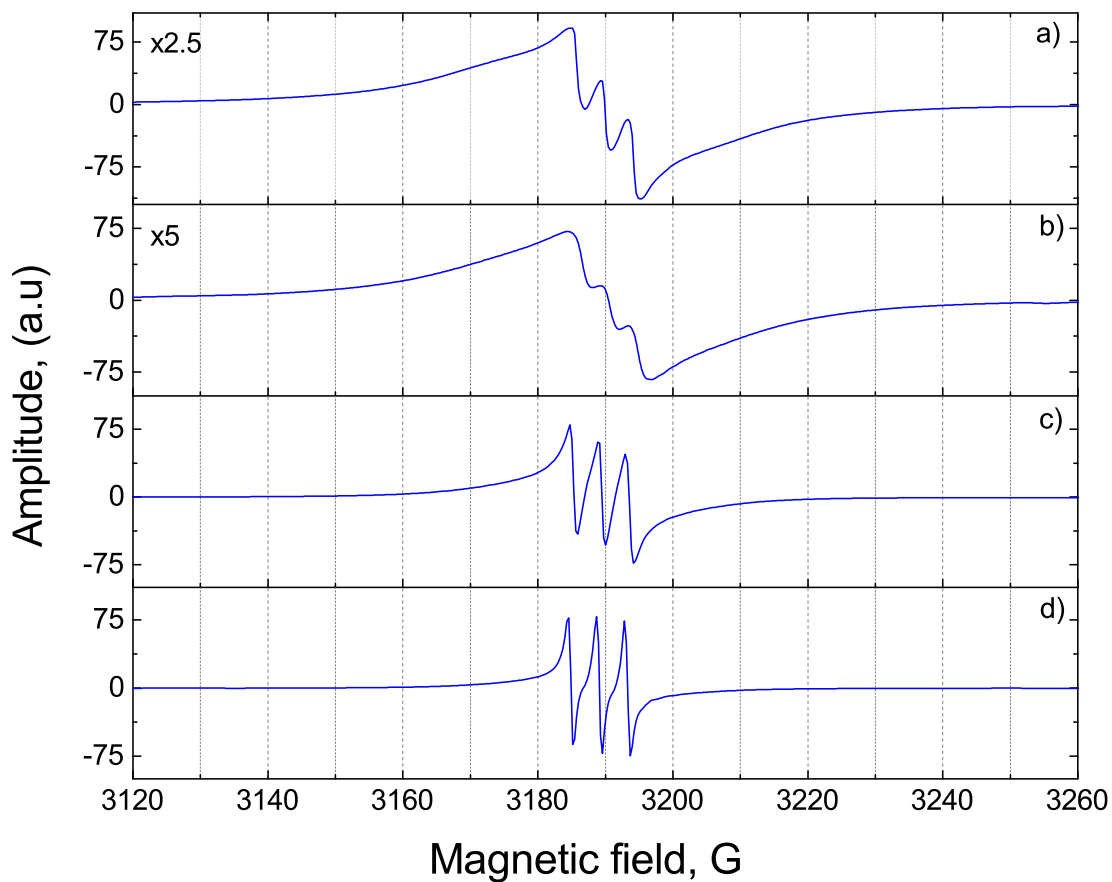
Figure 4.2: Experimental ESR spectra of N atoms stabilized in sample prepared from different nitrogen-argon-helium gaseous mixtures: $[N_2]:[Ar]:[He]=1:1:200$ (a), $[N_2]:[Ar]:[He]=1:5:600$ (b), $[N_2]:[Ar]:[He]=1:20:2000$ (c), $[N_2]:[Ar]:[He]=1:50:5000$ (d). All spectra were obtained at 1.35 K.

$[N_2]:[Ar]:[He]=1:5:600$, and the amplitude of the signal is half the size compared to the spectra obtained from the gas mixture $[N_2]:[Ar]:[He]=1:1:200$. More resolved ESR spectra of N atoms was detected for the sample prepared from the gas mixture $[N_2]:[Ar]:[He]=1:1:200$. Further the increases of the $[N_2]/[Ar]$ ratio to 1/20 and 1/50 led to even better resolved N atom signals. Finally, we investigated two types of samples obtained by condensation of gaseous mixtures of different compositions: $[N_2]:[He]$, and nitrogen-krypton-helium $[N_2]:[Kr]:[He]$. We can estimate the average concentration of N atoms in the samples by doubly integrating the derivatives of the ESR signals of the $N(^4S)$ and comparing with ruby reference signals. Table 4.1 gives the conditions of sample preparation and the calculated average concentration of $N(^4S)$ atoms as well as the efficiency of capturing of N atoms in the samples obtained for different gas mixtures. It can be seen from Table 4.1 that adding neon atoms to nitrogen-helium gas mixtures does not affect the efficiency of stabilization of N atoms. However, the addition of the Ar atoms to nitrogen-helium gas mixture led to an increase in the efficiency of stabilization of N atoms. The average concentration of N atoms is equal to $\sim 5\times10^{18}$ in the sample prepared from the gas mixture $[N_2]:[He]=1:100$, whereas for the sample prepared from the gas mixture $[N_2]:[Ar]:[He]=1:1:200$ the capturing efficiency is 4 times higher than that without the addition of Ar atoms to N_2-He gas mixture, and the average concentration of N atoms in this sample is equal to $\sim 1\times10^{19}$. It has also been found that addition of Kr atoms to nitrogen-helium gas mixtures leads to even larger increase in the average concentration of N atoms in the sample. For instance, for the $[N_2]:[He]=1:400$ gas mixture the average concentration of $N(^4S)$ atoms is $\sim 2.5\times10^{18}$, whereas for the $[N_2]:[Kr]:[He]=1:1:400$ gas mixture it is $\sim 1\times10^{19}$. Further increasing the addition of Kr atoms to the condensed nitrogen-helium gas mixture led to further increasing

Table 4.1: Experimental conditions for condensing IHCs, and average concentration of $N(^4S)$ atoms in IHCs with capturing efficiency.

Gas mixture	N_2 Flow Rate/s	Sample Accum. time, s	Average concent. cm^{-3}	N atoms Capture, Efficiency, %
$[^{14}N_2]:[He]$=1:100	5.00×10^{17}	600	5.09×10^{18}	1.0 %
$[^{14}N_2]:[He]$=1:400	1.25×10^{17}	600	2.47×10^{18}	1.95 %
$[^{14}N_2]:[He]$=1:800	6.25×10^{16}	600	1.21×10^{18}	1.90 %
$[^{14}N_2]:[Ne]:[He]$=1:1:50	1.00×10^{18}	600	9.06×10^{18}	0.9 %
$[^{14}N_2]:[Ne]:[He]$=1:5:100	5.00×10^{17}	600	5.19×10^{18}	1.0 %
$[^{14}N_2]:[Ne]:[He]$=1:20:400	1.25×10^{17}	600	2.11×10^{18}	1.7 %
$[^{14}N_2]:[Ne]:[He]$=1:50:1000	5.00×10^{16}	600	1.56×10^{18}	3.1 %
$[^{14}N_2]:[Ar]:[He]$=1:1:200	2.50×10^{17}	600	9.85×10^{18}	4.0 %
$[^{14}N_2]:[Ar]:[He]$=1:5:600	8.30×10^{16}	600	5.96×10^{18}	7.0 %
$[^{14}N_2]:[Ar]:[He]$=1:20:2000	2.50×10^{16}	600	2.58×10^{18}	10.0 %
$[^{14}N_2]:[Ar]:[He]$=1:50:5000	1.00×10^{16}	600	2.00×10^{18}	20.0 %
$[^{14}N_2]:[Kr]:[He]$=1:1:400	1.11×10^{17}	600	9.93×10^{18}	8.75 %
$[^{14}N_2]:[Kr]:[He]$=1:2:600	7.76×10^{16}	600	2.16×10^{19}	27.0 %
$[^{14}N_2]:[Kr]:[He]$=1:5:1200	4.25×10^{16}	600	3.04×10^{19}	70.0 %

the efficiency of N atom capture. For samples prepared from [N$_2$]:[Kr]:[He]=1:2:600 and [N$_2$]:[Kr]:[He]=1:5:1200 gas mixtures the efficiencies of N atom capture are 27 % and 70 %, respectively.

Analysis of the shape and width of the ESR spectra can also provide valuable information about structure of IHCs and matrix environments of stabilized nitrogen atoms. ESR linewidths ΔH$_{pp}$, the local concentrations, and hyperfine constants A of nitrogen atoms in N-Ne-He and N-Ar-He IHCs investigated in this work are shown in Table 4.2. The dipole-dipole broadening due to the electron spin-spin interactions between N atoms leads to broadening of ESR spectra of the N(^4S) atoms. We can determine the local concentration of N atoms in a specific environments by having determined the width of an individual triplet of the spectrum. The local concentrations of N atoms were obtained from equation as indicated earlier:

$$\Delta H_{pp} = 2.3 g \mu_0 \sqrt{S(S+1)} n_l, \tag{4.1}$$

[82] (4.1) was modified for N atoms (n$_l$=5.4 · 10^{18} ΔH$_{pp}$) where ΔH$_{pp}$ is the peak to peak width of the ESR lines in Gauss, and n$_l$ is the local concentration of the atoms per cm^3. For determination of the width of individual components, and the hyperfine splitting constant we employed a Graphic User Interface (GUI) program. The fitting process by GUI program was described in more detail section 3. As is seen in Fig. 4.3(a), Experimental ESR spectra of the nitrogen atoms can be convoluted as a sum of three triplets of Lorentzian lines as shown previously. Each of the triplets is assigned to N(^4S) atoms stabilized in different environment. We might identify the triplet (red-line) in Fig. 4.3(b) with N atoms trapped in the Ar matrix (A=4.30G); the narrow triplet (blue-line) in Fig. 4.3(b) is assigned to the N atoms inside the N$_2$ nanoclusters (A=4.20G); and the broad triplet (black-line) in Fig. 4.3(b) belongs to

Table 4.2: Analysis of ESR spectra of N atoms for different N_2/Ne/He and N_2/Ar/He samples, where A is the hyperfine structure constant, g corresponds to the g factors for N atoms, and ΔH_{pp} is the peak to peak width.

Sample	Curve type	A, G	ΔH_{pp}	Local concent. cm^{-3}	Weight %	g
$[^{14}N_2]$:[Ne]:[He]=1:1:50	L	4.12	28.47	$1.54 \cdot 10^{20}$	69	2.0021
	L	4.10	10.54	$5.69 \cdot 10^{19}$	30.5	2.0021
	L	4.20	1.34	$7.24 \cdot 10^{18}$	0.5	2.0021
$[^{14}N_2]$:[Ne]:[He]=1:5:100	L	4.12	23.94	$1.29 \cdot 10^{20}$	70.2	2.0025
	L	4.10	9.23	$4.98 \cdot 10^{19}$	28.1	2.0025
	L	4.20	1.61	$8.69 \cdot 10^{18}$	1.6	2.0025
$[^{14}N_2]$:[Ne]:[He]=1:20:400	L	4.12	26.58	$9.19 \cdot 10^{19}$	69.2	2.0022
	L	4.10	8.50	$4.17 \cdot 10^{19}$	25	2.0022
	L	4.20	3.20	$9.40 \cdot 10^{18}$	5.7	2.0022
$[^{14}N_2]$:[Ne]:[He]=1:50:1000	L	4.12	22.17	$8.88 \cdot 10^{19}$	73.1	2.0021
	L	4.10	5.02	$6.05 \cdot 10^{19}$	22.6	2.0021
	L	4.20	1.95	$4.13 \cdot 10^{19}$	4.2	2.0021
$[^{14}N_2]$:[Ar]:[He]=1:1:200	L	4.12	26.02	$1.41 \cdot 10^{20}$	76.5	2.0020
	L	4.30	14.73	$7.95 \cdot 10^{19}$	19.6	2.0020
	L	4.20	2.40	$1.30 \cdot 10^{19}$	3.8	2.0020
$[^{14}N_2]$:[Ar]:[He]=1:5:600	L	4.12	27.41	$1.48 \cdot 10^{20}$	79.6	2.0022
	L	4.30	12.37	$6.68 \cdot 10^{19}$	18.8	2.0022
	L	4.20	2.34	$1.26 \cdot 10^{18}$	1.5	2.0022
$[^{14}N_2]$:[Ar]:[He]=1:20:2000	L	4.12	14.33	$7.74 \cdot 10^{19}$	80.1	2.0020
	L	4.30	6.95	$3.75 \cdot 10^{19}$	13.6	2.0020
	L	4.20	1.19	$6.43 \cdot 10^{18}$	6.2	2.0020
$[^{14}N_2]$:[Ar]:[He]=1:50:5000	L	4.12	14.06	$7.59 \cdot 10^{19}$	70.9	2.0022
	L	4.30	6.24	$3.37 \cdot 10^{19}$	20	2.0022
	L	4.20	0.76	$4.10 \cdot 10^{18}$	9.1	2.0022
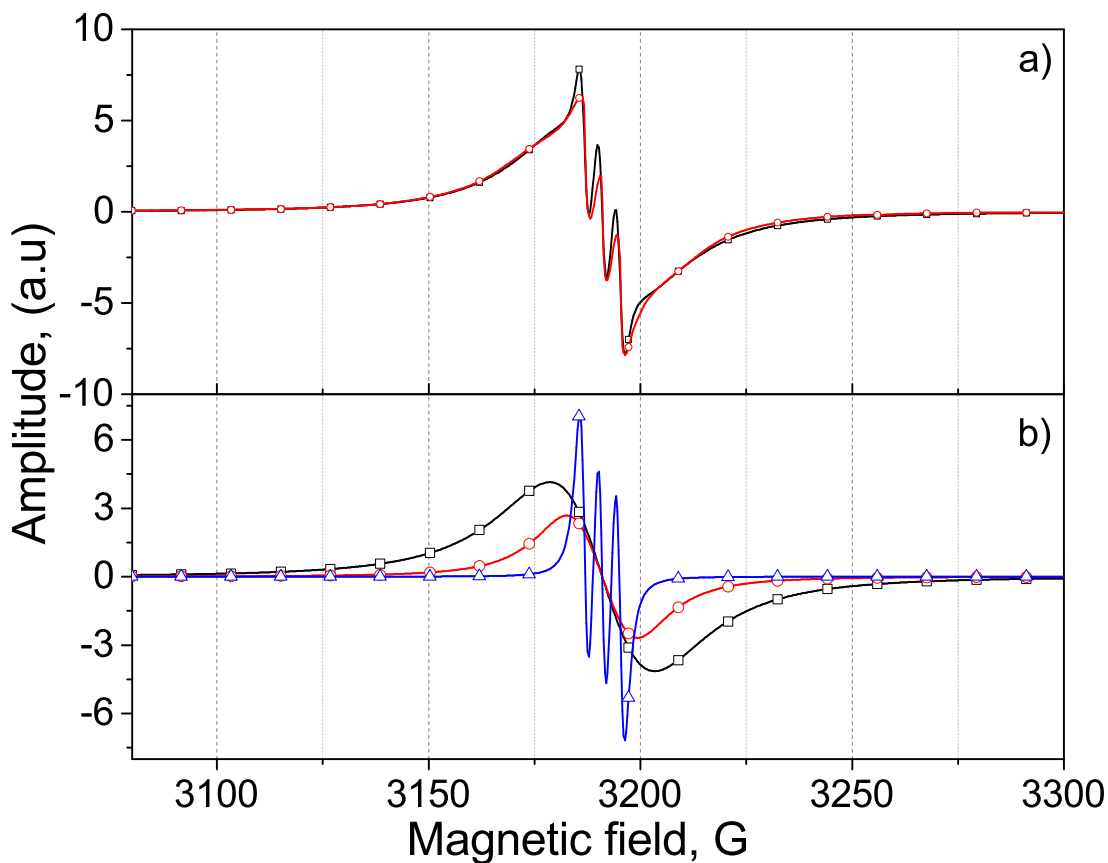
Figure 4.3: Experimental ESR spectrum of N atoms for an as-prepared nitrogen-helium sample formed from $[^{14}N_2]/[Ar]/[He]=1//1/200$ gas mixture is shown as a black line with squares and the sum of the fitting lines is shown as red line with circles (a). The three triplets of fitting lines used for deconvoluting the experimental ESR spectrum are shown in (b): blue line with triangles is a triplet of Lorentzian lines with the width 3.9 G, red line with circles is a triplet of Lorentzian lines with the width 22.4 G, black line with squares is a triplet of Lorentzian lines with the width 39.5 G.

N atoms located on the surface of the N_2 nanoclusters (A=4.12G), where A is the hyperfine constant.

4.1.2 Studies of thermoluminescence during warming up of N-N_2-Ne-He and N-N_2-Ar-He samples immersed in superfluid helium

We also studied thermoluminescence of N-N_2-Ne-He and N-N_2-Ar-He condensates containing stabilized nitrogen atoms during the warming up from 1.35 K to 2.16 K. After performing the registrations of ESR signals for as-prepared samples at T=1.35 K, the samples were heated to 2.16 K by ceasing pumping on the helium vapor. It is worth noting that the samples remain inside the superfluid helium during the entire period of warming up. Dynamics of the thermolumniesnce of a nitrogen-argon-helium sample prepared from the gas mixture [N_2]:[Ar]:[He]=1:1:200 is presented in Fig. 4.4 (a). Fig. 4.4(b) shows the integrated intensity of the spectra detected during the thermoluminescence process. The integrated spectra consists of an intense Vegard-Kaplan molecular band $N_2(A^3\Sigma_u^+, 0 \rightarrow X^1\Sigma_g^+, \nu'')$, the luminescence of the α-group of atomic nitrogen $N(^2D \rightarrow {}^4S)$, the β-group emission of atomic oxygen $O(^1S \rightarrow {}^1D)$. In addition to above-mentioned bands, a weak β''- groups of O atoms can be seen as a result of N_2 molecules being neighbors of the emitting O atoms. Fig. 4.4(c) presents the time dependence of the α- group, the Vegard-Kaplan bands, and the β-group intensities during warming from 1.32 K to 2.16K. It can be seen from Fig. 4.4(c), that there are a maxima of intensity of the luminescence at T $\sim$ 1.9 K for all three lines.

The maxima at T $\sim$ 1.9 K in the intensity of thermoluminescence may hold the key to understanding the nature of thermoluminescence at very low temperatures. Therefore, we performed studies of the behavior of the thermoluminescence

Figure 4.4: Thermoluminescence of nitrogen-argon-helium sample immersed in superfluid helium. Sample was prepared from gas mixture $[^{14}N_2]/[Ar]/[He]=1/1/200$. a) Dynamics of thermoluminescence spectra of the sample during warming up from 1.3 to 2.15 K. Each spectrum in the figure is a sum of 100 spectra taken with exposure time 50 ms. b) Integrated thermoluminescence spectra obtained during entire warming process. c) Time dependence of sample temperature (red-line). Time dependence of thermoluminescence intensity for nitrogen molecules (black-line with squares), nitrogen (blue-line with circles) and oxygen(magenta-line with triangles) atoms.

Figure 4.5: Temperature dependence of thermoluminescence intensity of nitrogen atoms for samples formed from different nitrogen-argon-helium gas mixtures: 1:1:200 (red-line with squares), 1:5:600 (black-line with triangles) and 1:20:2000 (blue-line with circles). Heat conductivity function for turbulent HeII (green-line).[83] Warm up to T $\sim$ 2.15 K lasted 202 s, 165 s, and 215 s, respectively.

dynamics for the samples prepared from gaseous mixtures of different compositions. Fig. 4.5 shows the temperature dependence of thermoluminescence for samples formed by injecting the gas mixtures of $[N_2]$:$[Ar]$:$[He]$ with different ratios. In Fig. 4.5 intensity of thermoluminescence for the samples prepared from gas mixtures $[N_2]$:$[Ar]$:$[He]$=1/5/600 and $[N_2]$:$[Ar]$:$[He]$=1/20/2000 were increased by a factor of 4 and 50, respectively. As one can see in Fig. 4.5 the position of the peak does not change for the three temperature dependence. In addition, it should be emphasized that the temperature dependence of thermal conductivity function of HeII due the turbulence (see in Fig. 4.5; green-line) fits fairly well with the temperature dependence of thermoluminescence for an as-prepared sample.

We also investigated the effect of adding different quantities of Ne atoms to the nitrogen-helium gas mixture on the behavior of the luminescence of N atoms in IHCs. Fig. 4.6(a) presents the dynamics of the thermoluminescence of a nitrogen-neon-helium sample prepared from the gas mixture $[^{14}N_2]$/$[Ne]$/$[He]$=1/1/100. The integrated intensity of the spectra obtained during the thermoluminescence process is shown in Fig. 4.6(b). Figure 4.6(c) shows the time dependence of intensity of α-group and Vegard-Kaplan bands. The intensities of α-group and Vegard-Kaplan bands for this sample are smaller due to lower the average concentration of N atoms (5.00×10^{18}) in contrast the sample formed from to 1/1/200 in the case of nitrogen-argon-helium gas mixtures, where the average concentration of N atoms is equal to 10×10^{18}. The integrated spectra of thermoluminescence of three different samples which were formed from $^{14}N_2$:Ne:He gas mixtures during warming up are shown in Fig. 4.7. Although only α-, β- groups and Vegard-Kaplan bands are detected for the sample prepared from the gas mixture $[^{14}N_2]$/$[Ne]$/$[He]$=1/1/100, in the case of $[^{14}N_2]$/$[Ne]$/$[He]$=1/20/400 and $[^{14}N_2]$/$[Ne]$/$[He]$=1/50/1000 samples the spectra
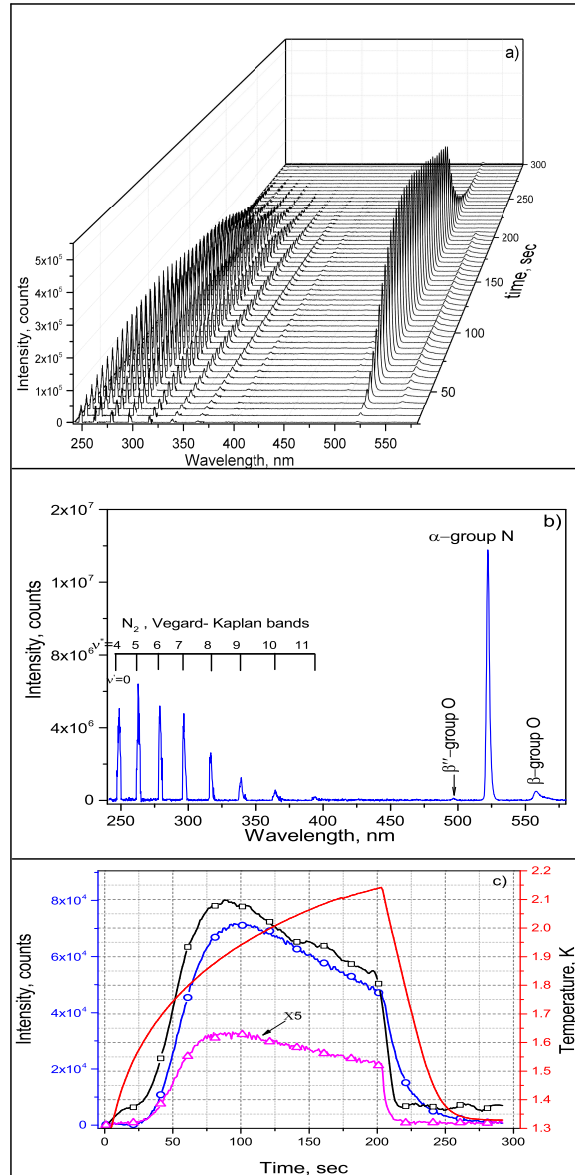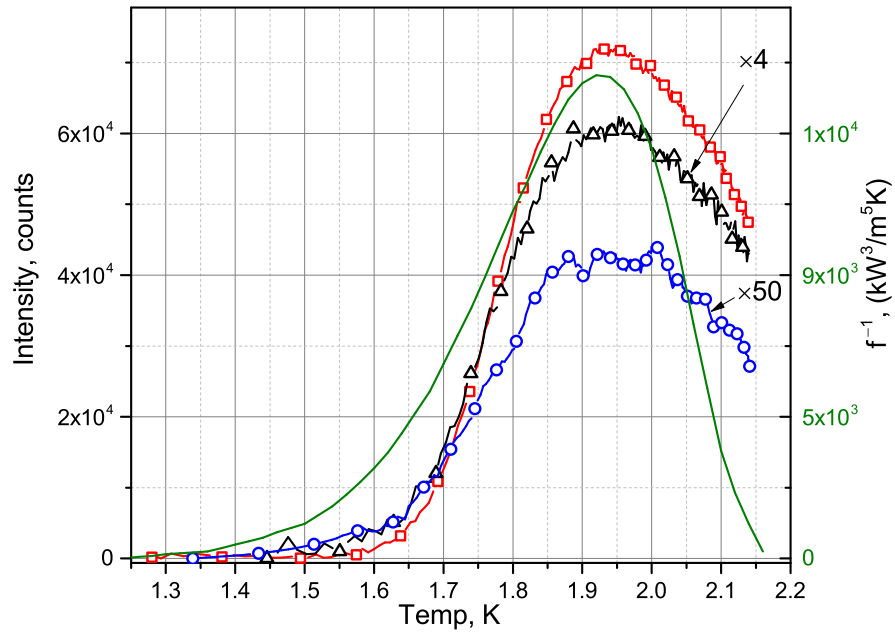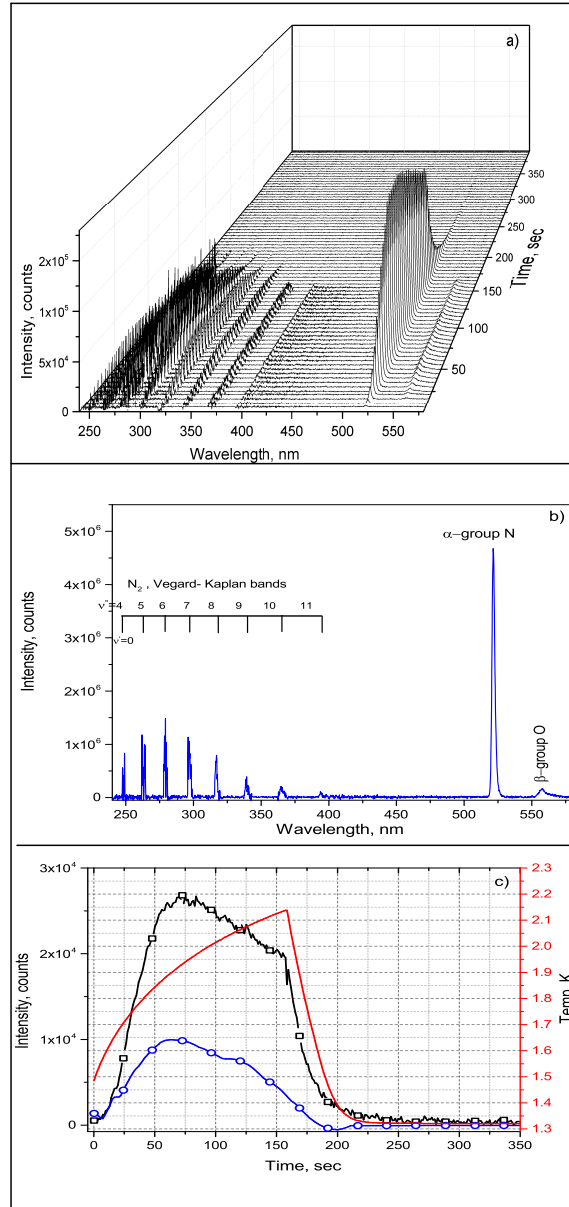
Figure 4.6: Thermoluminescence of nitrogen-neon-helium sample immersed in superfluid helium. Sample was prepared from gas mixture $[^{14}N_2]/[Ne]/[He]=1/1/100$. a) Dynamics of thermoluminescence spectra of the sample during warming up from 1.3 to 2.15 K. Each spectrum in the figure is a sum of 100 spectra taken with exposure time 50 ms. b) Integrated thermoluminescence spectra obtained during entire warming process. c) Time dependence of sample temperature (red-line). Time dependence of thermoluminescence intensity for nitrogen molecules (blue-line with circles), nitrogen (black-line with squares).
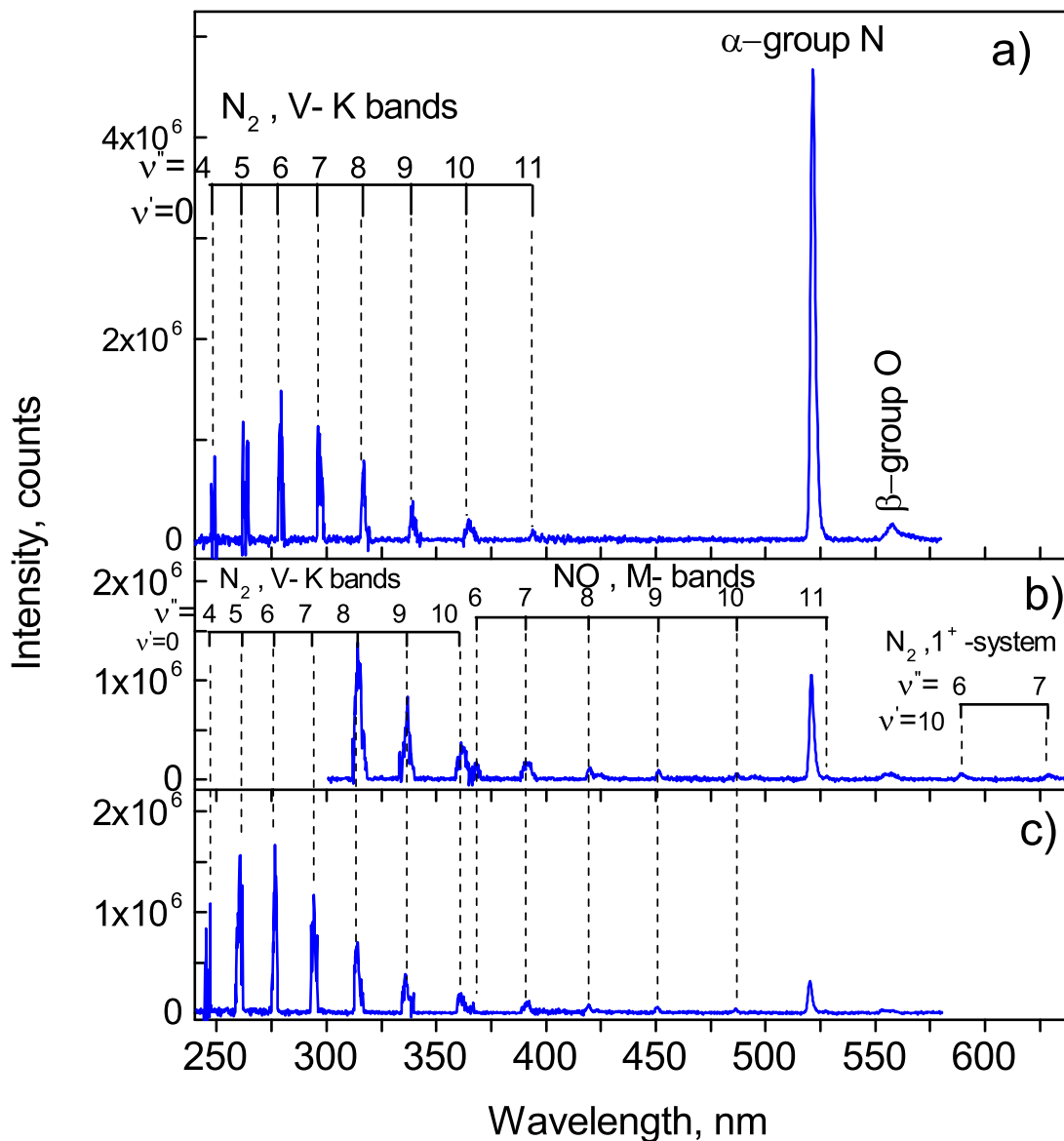
Figure 4.7: Integrated luminescence spectra obtained during warming of three nitrogen-neon-helium samples. Samples were prepared from $[^{14}N_2]$:[Ne]:[He] gas mixtures: a)1:1:100, b)1:20:400, c) 1:50:1000.
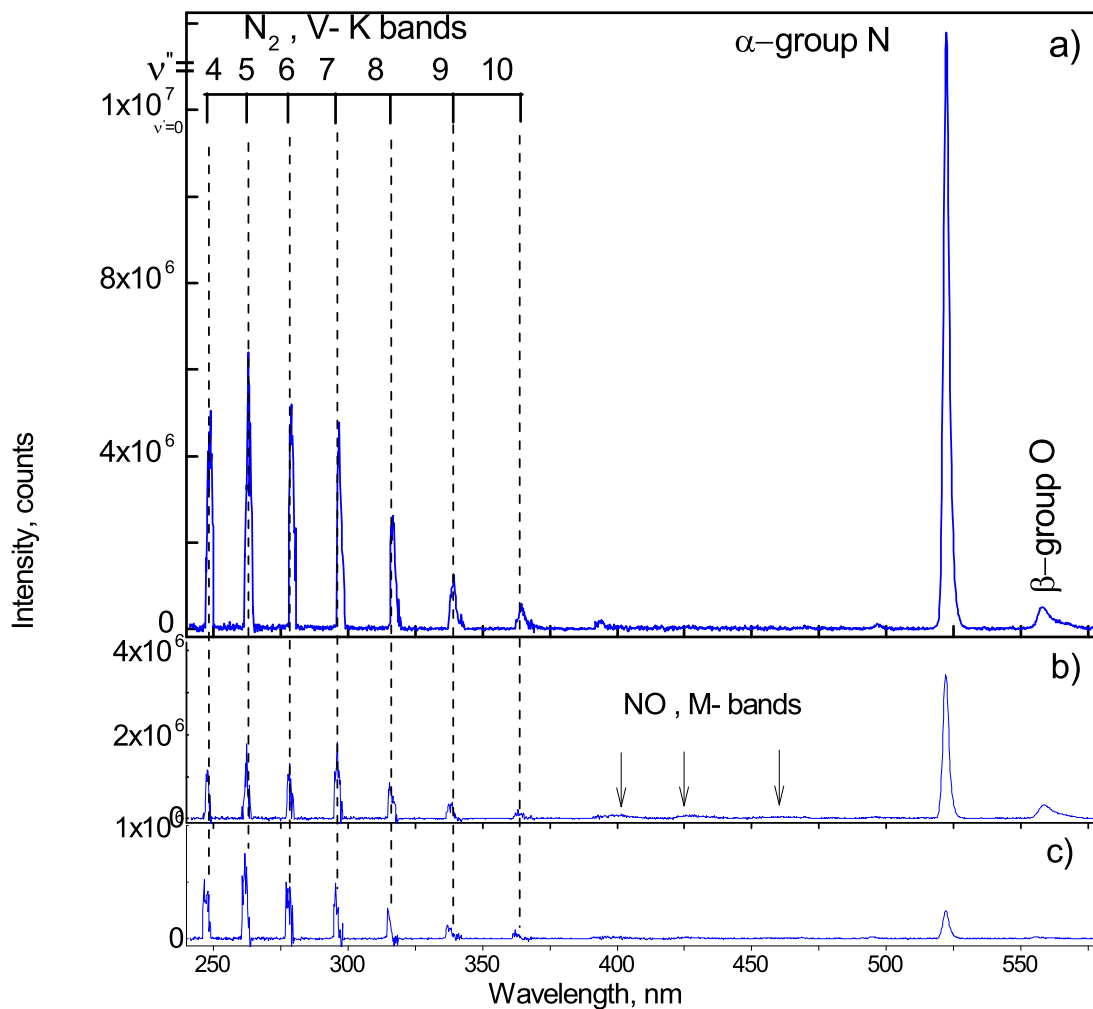
Figure 4.8: Integrated luminescence spectra obtained during warming of three nitrogen-argon-helium samples. Samples were prepared from $[^{14}N_2]$:[Ar]:[He] gas mixtures: a)1:1:200, b)1:5:600, c) 1:20:2000.

are half as intense, but in addition the bands of NO molecules are also present. In the case of samples prepared from the gas mixture $[^{14}N_2]/[Ne]/[He]=1/1/100$ and $[^{14}N_2]/[Ne]/[He]=1/50/1000$ the optical spectra were obtained in the spectral range 240-580 nm. The spectral range is 300-640 nm for the sample that was formed from $[^{14}N_2]/[Ne]/[He]=1/20/400$ gas mixture. As can be seen from Fig. 4.7(b), the bands at $\sim$ 589 nm and $\sim$ 629 nm are present in the spectrum. These bands were assigned to the $B^3\Pi-A^3\Sigma^1$ transition of N_2 molecules. Figure 4.8 also shows the integrated spectra of thermoluminescence of three different samples which were formed from $^{14}N_2$:Ar:He gas mixtures during warming up.

The temperature dependence of thermoluminescence for samples formed by injecting different gas mixtures of $[^{14}N_2]$:[Ne]:[He] are shown in Fig. 4.9. For the temperature dependence of thermoluminescence from $[^{14}N_2]$:[Ne]:[He]=1/5/100, 1/20/400, and 1/50/1000 were increased by a factor of 4, and 2, respectively. Again the maxima of the intensity of thermoluminescence is at T$\sim$1.9 K for all studied samples. This provides convincing evidence that the peak behavior has a common cause for all the different samples.

4.2   Discussion

The results obtained by ESR spectroscopy for N_2-Ne-He, N_2-Ar-He and N_2-Kr-He solids and optical spectroscopy for N_2-Ne-He, N_2-Ar-He solids allow us to study free radicals, molecules and nanoclusters stabilized in solidified helium. Impurity-helium condensates (IHCs) are a new class of non-crystalline nanomaterials formed by injecting a beam composed of helium and impurity gases into superfluid helium ^{4}He. When the gas jet meets the surface of the superfluid helium, the formation of nanoclusters each surrounded by one or two layers of solid helium due to Van der
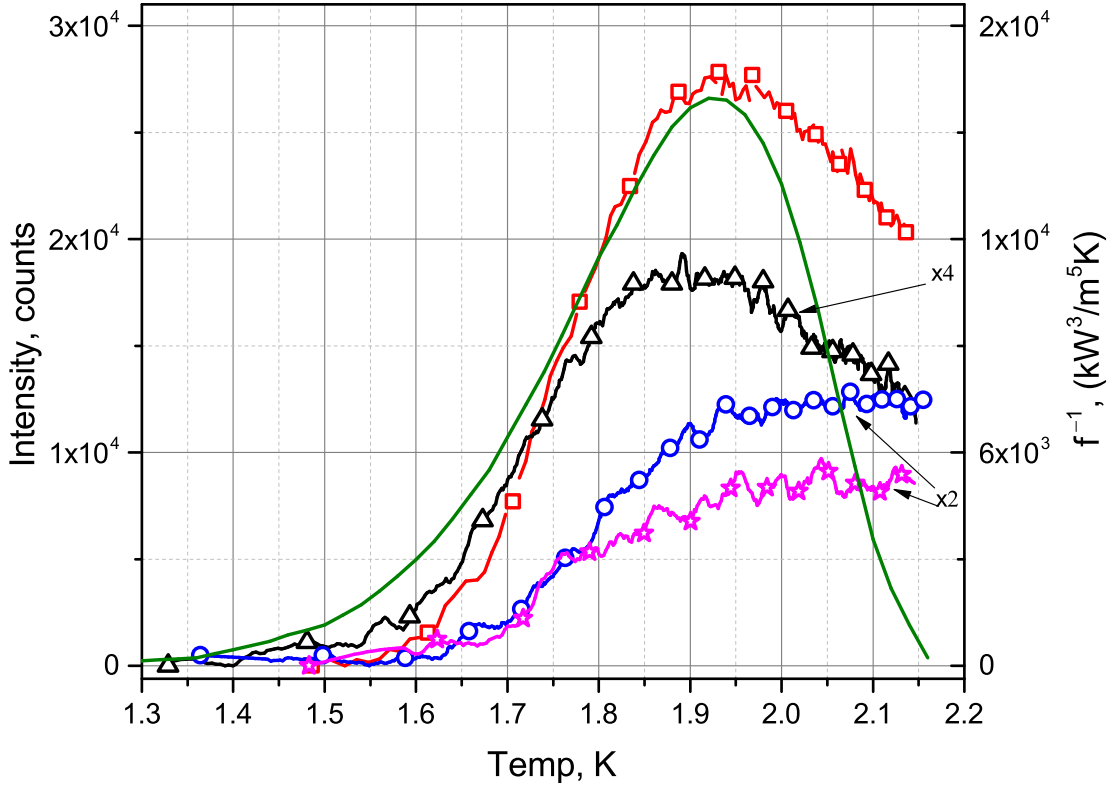
Figure 4.9: Temperature dependence of thermoluminescence intensity of nitrogen atoms for samples formed from different nitrogen-neon-helium gas mixtures: 1:1:100 (red-line with squares), 1:5:100 (black-line with triangles) and 1:20:400 (blue-line with circles), 1:50:1000 (magenta-line with stars). Heat conductivity function for turbulent HeII (green-line).[83] Warm up to T ∼ 2.15 K lasted 157 s, 212 s, 255 s, and 227 s, respectively.

95

Waal forces aggregate inside superfluid helium. Matrix isolation of highly reactive atoms in IHCs leads to high concentrations of these atoms. Upon the injection of impurity particles in bulk superfluid helium, a shell structures of nanoclusters are formed in such a way that heavier impurities form cores which are surrounded by shells lighter impurities.

In the present work, we studied the effect of addition of rare gas (RG) atoms (Ne, Ar, and Kr) to the condensed N_2-He gas mixture on the efficiency of stabilization of N atoms in IHCs. In experiments involving krypton-nitrogen-helium jets, high local and average concentrations of N atoms were achieved.[31] The average concentration of nitrogen atoms without addition of RG atoms to N_2-He gas mixture is $\sim 10^{18}$ cm^{-3}, and the efficiency of N atom capture for the N_2:He=1:100 is 1% while for the N_2:He=1:400 and N_2:He=1:800 gas mixtures the efficiencies of N atom capture are $\sim 2\%$ (see Table 4.1). Decreasing the size of clusters by reducing the content of N_2 relative to that of helium in the gas jet led to increase of the efficiency of N atom capture. As one can see in Table 4.1, a small increase of the capturing efficiency by the adding different quantities of neon atoms to the N_2-He gas mixtures might be also explained due to the differences in size of nanoclusters. However, the results of the measurements of the average concentrations of N atoms in N_2-Ar-He and N_2-Kr-He condensates shows that argon and especially krypton atoms play very important role, for increasing in the overall efficiency of stabilization of N atoms. Previous studies of H-H_2-Kr-He and D-D_2-Kr-He condensates demonstrated [11, 89] that the addition of Kr atoms to the condensed H_2-He or D_2-He gas mixture leads to a substantial increase in the average concentration of impurity atoms in the sample.

As one can see from table 4.3, as the size of the noble gas atoms increases, the melting temperature of the noble gases also increases. In addition, the melting

Table 4.3: The noble gases and other gases

Element	Melting temperature/^{o}C	Atomic Number	Relative molar/ Molecular mass
He	-272$_{at\ 26\ atm}$	2	4
Ne	-249	10	20
Ar	-189	18	40
Kr	-157	36	84
Xe	-112	54	131
O$_2$	-218	-	32
N$_2$	-210	-	28
NO	-164	-	30

temperature of N_2 and O_2 molecules are lower than melting temperature of Ar, Kr and Xe atoms, but higher than for Ne atoms. For noble gases the magnitude of the van der Waals forces increases by increasing the size of the atoms (see table 4.3). Van der Waals interaction between Ar-Ar and Kr-Kr are much stronger than for Ne-Ne atoms, so for the case of injection N_2-Ar-He and N_2-Kr-He jets into superfluid helium the Ar and Kr atoms initially form the cores of nanoclusters. After that, N atoms and N_2 molecules are attached to the surface of the Ar or Kr nanoclusters. In a previous study [31, 34], it was shown that the nanoclusters in the sample prepared from the mixture N_2-Kr-He and N_2-Xe-He exhibit a shell structure. Ar has an atomic number smaller than Kr and Xe but it might still be expected that the nanoclusters in the sample prepared from the mixture N_2-Ar-He should also exhibit a shell structure due to the stronger a Van der Waals interaction between Ar-Ar atoms compared to that of the other atoms. From the results of analysis of the shapes of the ESR spectra given in Table 4.2. we can conclude that the most N atoms (70%-90%) reside on the surface of N_2 layers, a smaller fraction of N atoms reside in the N_2 layer (1%-10%), and 13%-20% of N atoms reside inside the Ar clusters. On the other hand, the shell structure nanoclusters formed by condensing the jet containing (N_2-N-O-Ne-He) is quite different. After the jet cools down, first the nanoclsuters of N_2 are formed, later N and O atoms bind to the surface of the N_2 nanoclusters. At the next stage the layers of Ne atoms surround the nanoclusters, and finally a few layer of solidified helium atoms cover whole nanoclusters.

So far, investigations have been confined to the result of analyzing ESR spectra to give an understanding of the matrix environments of stabilized nitrogen atoms. Now we will turn our attention to investigation of the luminescence spectra detected during the warming up of the samples in superfluid helium from 1.32 K to 2.16 K.

The dynamics of the thermoluminescence spectra collected during the warming up of sample differ from the spectra that accompanied the destruction of the sample was discussed previously in section 2. Increasing the temperature of the sample immersed in liquid helium led to intense luminescence. At the beginning of warming up we observed emissions from the α-group of N atoms, the Vegard-Kaplan bands of N_2 molecules, and also the β-group of O atoms. Recombination of nitrogen atoms in the ground ^4S state is the main source of the excitation of atoms and molecules during the sample warming since the excitations from metastable $N_2(A^3\Sigma_u^+)$ were efficiently transferred to the $N(^4)$ and $O(^3P)$ atoms, resulting in formation of ^2D- state of N atoms and ^1S- state of O atoms. Some of the metastable $N_2(A^3\Sigma_u^+)$ molecules emitted light, producing Vegard-Kaplan bands. All processes leading to light emission can be represented by following equations:

$$N(^4S) + N(^4S) \rightarrow N_2(A^3\Sigma_u^+), \tag{4.2}$$

$$N_2(A^3\Sigma_u^+) + N(^4S) \rightarrow N(^2D) + N_2(X^1\Sigma_g^+), \tag{4.3}$$

$$N_2(A^3\Sigma_u^+) + O(^3P) \rightarrow O(^1S) + N_2(X^1\Sigma_g^+), \tag{4.4}$$

$$N(^2D) \rightarrow N(^4S) + \alpha\text{-}group, \tag{4.5}$$

$$O(^1S) \rightarrow O(^3P) + \beta\text{-}group. \tag{4.6}$$

$$N_2(A^3\Sigma_u^+) \rightarrow N_2(X^1\Sigma_g^+) + V\text{-}K\ bands, \tag{4.7}$$
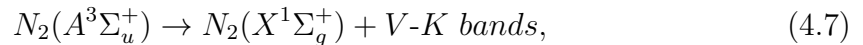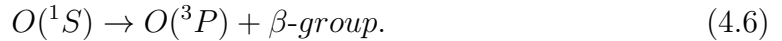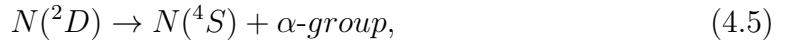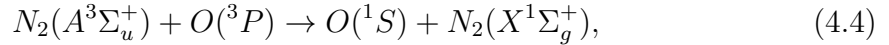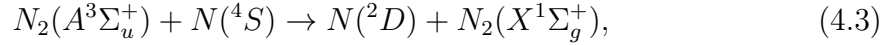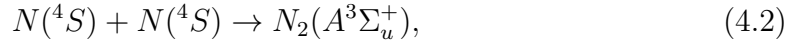
The glowing of the samples increased in intensity with increasing temperature, and reached the maxima at ~ 1.9 K. It should be pointed out that the position of the peak does not depend on concentration of N atoms stabilized in the sample prepared

99

from different gas mixtures. The temperature dependence of the turbulence buildup expression is similar to the temperature dependence of thermoluminescence for an as-prepared sample. This similarity provides evidence that the quantum vortices which formed as result of mutual friction between the normal and superfluid helium may initiate chemical reactions. Strands of the stabilized nitrogen atoms can contact each other, resulting in forming metastable $N_2(A^3\Sigma_u^+)$ due to the processes of the reconnection of the vortices. As a result of these processes the emission of the V-K bands of molecular nitrogen, α-group of nitrogen and β-group of oxygen atoms could have been produced.

The thermoluminescence of IHCs inside the superfluid helium was observed in previous studies [13, 28] and α-group is explained with the emission of $N(^2D)$ from two-body $N(^2D) - N_2$ complexes. According to this model, a single impurity atom or molecule is surrounded by a shell of localized helium atoms. Later structural studies of IHCs, however show clusters of impurities surrounded by thin layers of solid helium.[3, 4, 15, 16] Recently, another study suggested that thermoluminescence of IHCs submerged in helium is a result of neutralization reactions of thermally activated electrons with nitrogen cations.[34] This model could perhaps explain emission of the α-group by recombination of nitrogen cations and electrons, but it does not explain all other observed emission such as the β-group of $O(^1S)$ atoms, M-bands of NO molecules etc. The presence of β-group and M-bands of NO emission in the spectra shows that energy transfer occurs from excited nitrogen molecules to either N or O atoms isolated in a neon or argon matrix. The ESR measurements show that the number of stabilzed $N(^4S)$ atoms did not change during the warming of the samples in bulk HeII, but the total number of emitted photons from the sample during the entire process of warming up was found to be $\leq 1 \times 10^{13}$ for HeII. Thus

ESR measurements can not determine such small magnitudes of changes N atom concentrations. Therefore, the ESR studies do not confirm neutralization reactions for luminescence of IHCs inside superfluid helium. Furthermore, the observed effect of temperature dependence of thermoluminescence cannot be explained by dynamics of thermal relaxation because the characteristic of thermoluminescence dynamic do not change at different rates of warming (see figure 4.5 and 4.9).

One can see from Fig. 4.10 that there is a correlation between dependence of the average concentration of N atoms stabilized in the prepared sample and dependence of α-group of N atom emission intensity during the sample warm up. During the sample warming the overall integrated emission of intensity of the α-group increases with increasing the stabilized number of nitrogen atoms in the samples. On the other hand, the characteristics of the dynamics of the thermoluminescence spectra are same for different stabilized numbers of N atoms in the samples. Thus, it can be concluded that the relaxation of the stored energy in the nanoclusters is not responsible for observed the temperature dependence of the thermoluminescence. Now we shall discuss the observed features of the spectra from the samples prepared from nitrogen-neon-helium gas mixtures. In section 2 the effect of oxygen impurities on the luminescence spectra of nitrogen-helium condensates during the sample destruction was investigated. In the present work, we study the influence of oxygen impurities on the luminescence spectra of nitrogen-neon-helium condensates during the warming up inside the superfluid helium. The M-bands of NO molecules were absent in the integrated spectra for the sample prepared from gas mixture N_2:Ne:He=1:1:100 ($O_2/N_2 = 10^{-4}$ due to contamination of oxygen in the helium gas) as presented in Fig. 4.7a. However, increasing the ratio of O_2/N_2 from 10^{-4} to 4×10^{-4} in the sample prepared from gas mixture N_2:Ne:He=1:20:400 led to the appearance of the M-bands

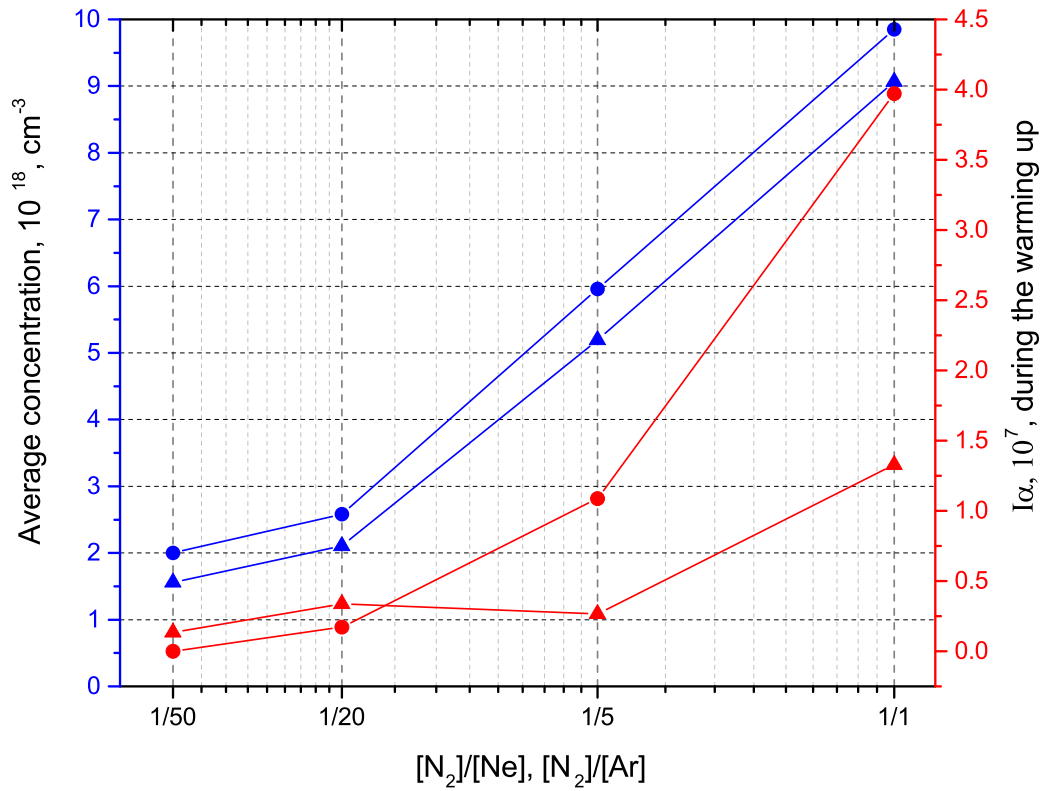Figure 4.10: Dependence of the average concentration of N atoms stabilized in N_2-Ne-He and N_2-Ar-He samples on the N_2/Ne (blue-line with triangles) and N_2/Ar (blue-line with circles) ratios in gas mixtures. Dependence of α-group intensity of nitrogen atoms in N_2-Ne-He and N_2-Ar-He samples on the N_2/Ne (red-line with triangles) and N_2/Ar (red-line with circles) ratios in gas mixtures.

of NO molecules. Similar results are also seen for the case of samples prepared from gas mixture N_2:Ar:He=1:5:600, N_2:Ar:He=1:20:2000, and N_2:Ar:He=1:20:2000 (see figure 4.8). The NO molecules were formed as a result of recombination of $N(^4S)$ and $O(^3P)$ atoms, leading to the appearance of NO molecular emission. According to the following processes:

$$N(^4S) + O(^3P) \rightarrow NO(a^4\Pi); \tag{4.8}$$

$$NO(a^4\Pi) \rightarrow NO(X^2\Pi) + h\nu \ (M\text{-}bands); \tag{4.9}$$
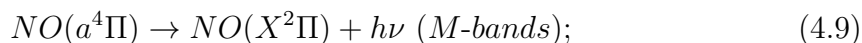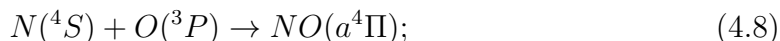
In addition to the appearance of the M-bands of NO, the emission of the 1^+ system of molecules were also detected for this sample. The presence of the excited $N_2(B^3\Pi_g)$ state might be explained by the fact that the B state has vibrationally resonant levels with the $N_2(A^3\Sigma_u^+)$ state.

For the case of the sample prepared from the gas mixture N_2:Ne:He=1:1:100 the positions of the V-K bands of N_2 molecules shows that emissions occur from the N_2 matrix. On the other hand, for the case of sample prepared from the gas mixture N_2:Ne:He=1:20:400 and N_2:Ne:He=1:50:1000 the V-K bands of N_2 and the M-band of NO positions correspond to that obtained for Ne matrices. The position of the α-group also reveals the environment of the emitting N atoms during sample warming-up. The α-group spectra in the integrated spectra during the warming-up for the sample prepared from the gas mixture N_2:Ne:He=1:1:100 had a maximum at 522 nm, whereas for the case of the sample prepared from the gas mixture N_2:Ne:He=1:20:400, and N_2:Ne:He=1:50:1000, the peaks were detected at 521 nm and 520 nm, respectively. These spectral features lead to the conclusion that during the warming-up for the sample prepared from the N_2:Ne:He=1:1:100 gas mixture the emitting $N(^2D)$ atoms was surrounded mostly by N_2 molecules,

while during the warming-up for the case of sample prepared from the gas mixtures N_2:Ne:He=1:20:400 and N_2:Ne:He=1:50:1000 the N atoms and NO molecules were surrounded mostly by Ne atoms. This interpretation, is in reasonable agreement with the differences of the dynamics of the α-group emission observed in Fig. 4.8. The differences of the temperature dependence of the α-group emission in Fig. 4.8 apparently result from differences in the environment of the $N(^2D)$ metastable atom in the IHCs. Typical decay times of the α-group for Ne-containing IHCs samples are noticeably longer than for a N_2 matrix. For the IHCs samples obtained by the condensation of N_2:Ne:He mixtures decay times of the α-group is $\sim$300 s, whereas for the N_2 matrix they are only $\sim$30 s.

It is possible that the helium adsorbed on the surfaces is weakly bound as to allow the clusters to approach one another until their surfaces touch. The interaction of nitrogen and oxygen atoms due to the quantum vortices in superfluid helium can initiate local recombination of the atoms residing on surfaces of clusters. The detection of NO molecules during warming up confirms the assumption of a chemical reaction proceeding in the IHCs at low temperature.

5. CONCLUSION

In section 2, dynamics of thermoluminescence from nitrogen-helium condensates formed by the collection of nanoclusters containing stabilized N and O atoms was studied during their destruction. At the beginning of the destruction, the fusion of nanoclusters was accompanied by the emission from N atoms and N_2 molecules as a result of recombination of N atoms. At the final stage the emission by O atoms as well as NO and O_2 molecules became dominant. The influence of oxygen impurities on the luminescence spectra of nitrogen-helium condensates was studied. Increasing the relative content of oxygen in molecular nitrogen nanoclusters from 10^{-4} to 10^{-3} led to domination of the bands from oxygen atoms as well as NO and O_2 molecules in the integrated thermoluminescence spectra. The mechanism of excitation of emitting species during destruction of nitrogen-helium condensates was revealed. Recombination of nitrogen atoms within molecular nitrogen nanoclusters produce metastable $N_2(A^3\Sigma_u^+)$ molecules which are responsible for energy transfer to stabilized N and O atoms and NO molecules. The mechanism of oxygen accumulation during destruction of nitrogen-helium condensates was revealed. Oxygen atoms recombine with nitrogen atoms resulting in formation NO molecules. These NO molecules are stored in the samples due to their high van der Walls interaction. The accumulation of NO molecules in the samples was accompanied by a growth of the luminescence of oxygen-containing species with time. For the first time the O_2 $(c^1\Sigma_u^- \rightarrow a^1\Delta_g)$, and $(c^1\Sigma_u^- \rightarrow X^3\Sigma_g^-)$ molecular bands were observed at the end of the destruction of nitrogen-helium condensates. This effect was explained by the formation of $(NO)_2$ dimers in solid nitrogen crystallites during fusion of nanoclusters. The dissociation of $(NO)_2$ dimers and their recombination with nitrogen atoms released pairs of O

atoms in close vicinity. These pairs of O atoms can recombine and create excited states of O_2 molecules.

In section 3, we developed a new experimental approach for studying quantum vortices in HeII in porous materials. We observed quantum vortix induced chemical reactions in porous ensembles of nanoclusters immersed in superfluid helium. These observations open new possibilities for studying chemical reactions of heavy species induced by vortices at very low temperatures in HeII where diffusion and tunneling in solid nanocrystallites are completely suppressed. We also observed the thermoluminescence of ensembles of nitrogen nanoclusters in normal liquid helium which was initiated by association of the nanoclusters resulting in thermal explosion of a small fraction of nanoclusters. Thermal explosions occur due to chain reactions of nitrogen atoms stabilized in nanoclusters for the conditions of poor thermal heat removal by the surrounding liquid helium.

In section 4, the impurity-helium solids created by injection of nitrogen atoms and molecules together with rare gas atoms (Ne, Ar or Kr) into superfluid helium have been studied by the ESR method and optical spectroscopy. ESR results show that most of stabilized N atoms reside on surfaces of nanoclusters. Argon and krypton atoms significantly increase the overall efficiency of stabilization of N atoms in IHCs. Also, we showed that behavior of the dynamics of the thermoluminescence spectra are same for different stabilized numbers of N atoms in the samples.

REFERENCES

[1] E.B. Gordon, L.P Mezhov-Deglin, and O.F. Pugachev. *JETP Lett.*, 19:63, 1974.

[2] V. Kiryukhin, B. Keimer, R.E. Boltnev, V.V. Khmelenko, and E.B. Gordon. *Phys. Rev. Lett.*, 79:1774, 1997.

[3] S.I. Kiselev, V.V. Khmelenko, D.M. Lee, V. Kiryukhin, R.E. Boltnev, E.B. Gordon, and B. Keimer. *Phys. Rev. B*, 65:024517, 2002.

[4] N.V. Krainyukova, R.E. Boltnev, E.P. Bernard, V.V. Khmelenko, V. Kiryukhin, and D.M. Lee. *Phys. Rev. Lett.*, 109:245505, 2012.

[5] E.B. Gordon, V.V. Khmelenko, E.A. Popov, A.A. Pelmenev, and O.F. Pugachev. *Chem. Phys. Lett.*, 155:301, 1989.

[6] E.P. Bernard, R.E. Boltnev, V.V. Khmelenko, V. Kiryukhin, S.I. Kiselev, and D.M. Lee. *Phys. Rev. B.*, 69:104201, 2004.

[7] V.V. Khmelenko, H. Kuntuu, and D.M. Lee. *J. Low Temp. Phys.*, 148:1, 2007.

[8] V.V. Khmelenko, R.E. Boltnev, E.B. Gordon, I.N. Krushinkaya, M.V. Martynenko, A.A. Pelmenev, E.A. Popov, and D.Y. Stolyakov. *Proceedings of Second International Conference on Low Temperature Chemisty, University of Missouri-Kansas City, Kansas City*, page 163, 1996.

[9] L.P. Mezhov-Deglin and A.M. Kokotin. *J. Low Temp. Phys.*, 119:385, 2000.

[10] R.E. Boltnev, A.A. Krushinskaya, I.N.and Pelmenev, E.A. Popov, D. Yu Stolyarov, and V.V. Khmelenko. *Low Temp. Phys.*, 31:547, 2005.

[11] R.E. Boltnev, E.P. Bernard, J. Jarvinen, V.V. Khmelenko, and D.M. Lee. *Phys. Rev. B*, 79:180506, 2009.

[12] E.B Gordon, A.A. Pelmenev, O.F. Pugachev, and V.V. Khmelenko. *Chem. Phys.*, 61:35, 1981.

[13] R.E. Boltnev, E.B. Gordon, V.V. Khmelenko, I.N. Krushinskaya, M.V. Marynenko, A.A. Pelmenev, E.A. Popov, and A.F. Shestakov. *Chem. Phys.*, 189:367, 1994.

[14] V.V. Khmelenko, D.M. Lee, I.N. Krushinskaya, R.E. Boltnev, I.B. Bykhalo, and A.A. Pelmenev. *Low Temp. Phys.*, 38:688, 2012.

[15] E.P. Bernard, R.E. Boltnev, V.V. Khmelenko, V. Kiryukhin, S.I. Kieselev, and D.M. Lee. *Phys. Rev. B*, 69:104201, 2004.

[16] V. Kiryukhin, E.B. Bernard, V.V. Khmelenko, R.E. Boltnev, N.V. Krainyukova, and D.M. Lee. *Phys. Rev. Lett.*, 98:195506, 2007.

[17] S.I. Kiselev, V.V. Khmelenko, and D.M. Lee. *J. Low Temp. Phys.*, 121:671, 2000.

[18] S.I. Kiselev, V.V. Khmelenko, and D.M. Lee. *Low Temp. Phys.*, 26:641, 2000.

[19] Vegard. *Nature*, 113:716, 1924.

[20] Vegard. *Nature*, 114:357, 1924.

[21] A.M. Bass. *Formation and Trapping of Free Radicals, Academic Press New York, London (1960).*

[22] E. Savchenko, I. Khyzhniy, S. Uyutnov, A. Barabashov, G. Gumenchuk, A. Ponomaryov, and V. Bondybey. *J. Phys. Chem. C.*, 12:49, 2014.

[23] E. Savchenko, I. Khyzhniy, S. Uyutnov, A. Barabashov, G. Gumenchuk, M.K. Beyer, A. Ponomaryov, and V. Bondybey. *J. Phys. Chem. A*, 119:2475, 2015.

[24] A.M. Bass. *Phys. Rev.*, 101:1740, 1956.

[25] B.J. Fontana. *J. Appl. Phys.*, 29:1668, 1958.

[26] M. Peyron and H.P. Brioda. *J. Chem. Phys.*, 30:139, 1959.

[27] H.P. Brioda and M. Peyron. *J. Chem. Phys.*, 32:1068, 1960.

[28] E.B. Gordon, L.P Mezhov-Deglin, O.F. Pugachev, and V.V. Khmelenko. *Cryogenics*, 16:555, 1976.

[29] V.V. Khmelenko, E.P. Bernard, S. Vasiliev, and D.M. Lee. *Russ. Chem. Rev.*, 76:1107, 2007.

[30] E.P. Bernard, V.V. Khmelenko, and D.M. Lee. *J. Low Temp. Phys.*, 150:516, 2008.

[31] S. Mao, V.V. Boltnev, V.V. Khmelenko, and D.M. Lee. *Low Temp. Phys.*, 38:1037, 2012.

[32] R.E. Boltnev, I.N. Krushinskaya, A.A. Pelmenev, D. Yu Stolyarov, and V.V. Khmelenko. *Chem. Phys. Lett.*, 305:217, 1999.

[33] V.V. Khmelenko, A.A. Pelmenev, I.N. Krushinskaya, I.B. Bykhalo, R.E. Boltnev, and D.M. Lee. *J. Low Temp. Phys.*, 171:302, 2013.

[34] R.E. Boltnev, I.B. Bykhalo, I.N. Krushinskaya, A.A. Pelmenev, , V.V. Khmelenko, S. Mao, A. Meraki, S.C. Wilde, P.T. McColgan, and D.M. Lee. *J. Phys. Chem. A*, 119:2438, 2015.

[35] H. Kajihara, T. Okamura, F. Okada, and S. Koda. *Laser Chem.*, 15:83, 1995.

[36] J. Goodman and L.E. Brus. *J. Chem. Phys.*, 67:1482, 1977.

[37] W.F. Vinen. *Proc. R. Soc. A*, 240:114, 1957.

[38] W.F. Vinen. *Proc. R. Soc. A*, 242:493, 1957.

[39] K.L. Chopra and J.B. Brown. *Phys. Rev.*, 108:157, 1957.

[40] G.A. Williams and R.E. Packard. *Phys. Rev. Lett.*, 33:280, 1974.

[41] E.J. Yarmchuk, M.J.V. Gordon, and R.E. Packard. *Phys. Rev. Lett.*, 43:214, 1979.

[42] E. Fonda, D.P. Meichle, N.T. Ouellette, S. Hormoz, and D.P. Lathrop. *PNAS*, 111(10):4707–4710, 2014.

[43] G.P. Bewley, D.P. Lathrop, and K.R. Sreenivasan. *Nature*, 441(4):588, 2006.

[44] W. Guo, J.D. Wright, S.B. Cahn, J.A. Nikkel, and D.N. McKinsey. *Phys. Rev. Lett.*, 102(6):235301, 2009.

[45] S. Babuin, M.Stammeier, E. Varga, M. Rotter, and L. Skrbek. *Phys. Rev. B*, 86(7):134515, 2012.

[46] D.E. Zmeev, F. Pakpour, P.M. Walmsley, A.I. Golov, W. Guo, D.N. McKinsey, G.G. Ihas, P.V.E. McClintock, S.N. Fisher, and W.F. Vinen. *Phys. Rev. Lett.*, 110(5):175303, 2013.

[47] W. Guo, M. LaMantia, D.P. Lathrop, and S.W. Van Sciver. *PNAS*, 111(8):4653–4658, 2014.

[48] G.P. Bewley, M.S. Paoletti, K.R. Sreenivasan, and D.P. Lathrop. 105(9):13707–13710, 2008.

[49] P.M. Walmsley, A.I. Golov, H.E. Hall, A.A. Levchenko, and W.F. Vinen. *Phys. Rev. Lett.*, 99(11):265302, 2007.

[50] P. Walmsley, D. Zmeev, F. Pakpour, and A. Golov. *PNAS*, 111(12):4691–4698, 2014.

[51] E.B Gordon, A.V. Karabulin, V.I .Matyushenko, V.D. Sizov, and I.I. Khodos. *J. Exp. Theor. Phys.*, 112(13):1061–1070, 2011.

[52] E.B. Gordon, A.V. Karabulin, V.I.Matyushenko, V.D. Sizov, and I.I. Khodos. *Chem. Phys. Lett.*, 519-520(14):64–68, 2014.

[53] L.F. Gomez, E. Loginov, and A.F. Vilesov. *Phys. Rev. Lett.*, 108(15):155302, 2012.

[54] L.F. Gomez et al. *Science*, 345(16):906–909, 2014.

[55] M.H.W. Chan, K.I. Blum, S.Q. Murphy, G.K.S. Wong, and J.D. Reppy. *Phys. Rev. Lett.*, 61(18):1950, 1988.

[56] J.D. Reppy. *J. Low Temp. Phys*, 87(17):205, 1992.

[57] J. Yoon, D. Sergatskov, J. Ma, N. Mulders, and M.H.W. Chan. *Phys. Rev. Lett.*, 80(19):1461, 1998.

[58] R. Toda, M. Hieda, T. Matsushita, N. Wada, J. Taniguchi, H. Ikegami, S. Inagaki, and Y. Fukushima. *Phys. Rev. Lett.*, 99(20):255301, 2007.

[59] A.A. Pelmenev, I.N. Krushinskaya, I.B. Bykhalo, and R.E. Boltnev. *Low Temp. Phys.*, 42(33):224–229, 2016.

[60] R.J. William. *Modern Physics from a to ZO, Wiley,(1994)*.

[61] E.A. Popov, J. Eloranta, J. Ahokas, and H. Kunttu. *Low Temp. Phys.*, 29:510, 2003.

[62] O. Oehler, D.A Smith, and K. Dressler. *J. Chem. Phys.*, 66:2097, 1977.

[63] R.J. Sayer, R.H. Prince, and W.W. Duley. *Proc. R. Soc. Lond. A.*, 373:477, 1981.

[64] S. Koda and H. Kajihara. *Bull. Chem. Soc. Jpn.*, 70:1225, 1997.

[65] H. Kajihara, T. Okamura, and S. Koda. *Laser Chem.*, 15:83, 1994.

[66] P.H. Krupenie. *J. Phys. Chem. Ref. Data*, 1:423, 1972.

[67] J. Eloranta, K. Vaskonen, H. Hakkanen, T. Kiljunen, and H. Kunttu. *J. Chem. Phys.*, 109:7784, 1998.

[68] R. Vivie and S.D. Peyerimhoff. *J. Chem. Phys.*, 89:3028, 1988.

[69] S. Nourry and L. Krim. *MNRAS*, 450:2903, 2015.

[70] R.E. Boltnev, I.N. Bykhalo, A.A. Krushinskaya, A.A. Pelmenev, S. Mao, A. Meraki, P.T. McColgan, D.M. Lee, and V.V. Khmelenko. *Phys. Chem. Chem. Phys.*, 18:16013, 2016.

[71] M. Chergui, N. Schwentner, and A. Tramer. *Chem. Phys. Lett.*, 201:187, 1993.

[72] I.Y. Fugol and Y.B. Poltotatski. *Solid State Commun.*, 30:497, 1979.

[73] T.G. Slanger. *J. chem. Phys.*, 69:4779, 1978.

[74] E.M. Horl. *J. Mol. Spectrosc.*, 3:425, 1959.

[75] J. Fournier, J. Deson, and C. Vermeil. *J. chem. Phys.*, 68:5062, 1978.

[76] L.G. Piper, L.M. Cowles, and T. Pawlins. *J. Chem. Phys.*, 85:3369, 1986.

[77] F. Legay and N. Legay-Sommaire. *Chem. Phys. Lett.*, 211:516, 1993.

[78] R.A. Ruehrwein, J.S. Hashma, and J.W. Edwards. *J. Phys. Chem.*, 64:1317, 1960.

[79] W.F. Vinen. *Proc. Royal Soc. London*, A249:114–127, 1957.

[80] J.T. Tough and D.F. Brewer. *Progress in Low Temp. Phys. ed.*

[81] S. Babuin, M. Stammeier, E. Varga, M. Rotter, and L. Skrbek. *Phys. Rev. B*, 86:134515, 2012.

[82] C. Kittel and E. Abrahams. *Physical Review*, 90(1):238, 1953.

[83] S.W. Van Sciver. *Helium Cryogenics.* Plenum Press, New York and London, 1st edition, 1986.

[84] S.I. Kiselev, V.V. Khmelenko, D.M. Lee, V. Kiryukhin, R.E. Boltnev, E.B. Gordon, and B. Keimer. *J. Low Temp. Phys.*, 126(31):235, 2002.

[85] A.A. Ovchinnikov. *Sov. Phys. JETP*, 30(36):147–150, 1970.

[86] K. Dressler, O. Oehler, and D.A. Smith. *Phys. Rev. Lett.*, 34(37):1364–1367, 1975.

[87] W.F. Vinen. *J. Low Temp Phys.*, 145(1):7–24, 2006.

[88] D.D. Awschalom and K.W. Schwarz. *Phys. Rev. Lett.*, 52(38):49–52, 1984.

[89] R.E. Boltnev, E.P. Bernard, J. Jarvinen, I.N. Krushinskaya, V.V. Khmelenko, and D.M. Lee. *J. Low Temp. Phys.*, 158:468, 2010.